Multiresolution Image Analysis
Innovative applications for Positron Emission Tomography in clinical practice

Grecchi, Elisabetta

Awarding institution:
King's College London

Multiresolution Image Analysis

Innovative applications for Positron Emission Tomography in clinical practice

Elisabetta Grecchi

Department of Imaging Sciences & Biomedical Engineering

King's College London

A thesis submitted for the degree of

Doctor of Philosophy

London 2016

This thesis is dedicated to the memory of my father and to my mother, who offered unconditional love and support and has always been there for me.

Abstract

Positron Emission Tomography is an excellent tool to image physiological processes *in vivo* and it is of great potential when it comes to disease staging for targeted therapies. However, the potential of PET imaging is somewhat limited by its low spatial resolution with resulting significant partial volume effect (PVE) that deteriorates the accuracy of the quantification of the physiological process under scrutiny. In this context, the use of multimodality imaging is very convenient to resolve this limitation. Using novel techniques based on a multiresolution approach, it is possible to recover PET resolution by a synergistic coupling of the PET images with the anatomical counterpart, either CT or MRI. The multiresolution analysis is performed through a wavelet decomposition of both functional and anatomical images which has been used already in the past with similar purposes.

The aim of this thesis is to present novel multiresolution partial volume correction (PVC) techniques that target two different clinical applications. The first part of the project aims to correct for PVE in order to improve the clinical assessment of [18F]Fluoride PET/CT imaging in presence of bone metastasis from prostate and breast cancer. In the second part of the project we develop a different PVC multiresolution approach aiming to improve the quantification of [11C]PIB PET/MR brain myelin imaging in Multiple Sclerosis (MS) patients. The algorithms validation was performed using either phantom data or clinical images of human controls.

The main result of this work is that application of the PVC methodology resulted in a very significant gain in image resolution without any detectable increase of image noise. Lesions sharpness and detectability improved as well with a resulting increase in quantification accuracy. The algorithms developed and presented in this thesis proved to be straightforward tools to improve PET quantification in routine clinical practice.

Acknowledgements

This project has taken place at both St Thomas' Hospital, London, and the Centre for Neuroscience, Institute of Psychiatry, Denmark Hill, London, since July 2012. During this period I have interacted with several people and I am very thankful to all of those that have helped and guided me. From those, there are some individuals to whom I am grateful and I wish to acknowledge them.

Foremost, I am extremely grateful to my supervisor Prof Federico Turkheimer for his support and encouragement throughout this years. It has been an honour to work with him and take advantage of his excellent scientific guidance and inspiration - I am grateful for the time he granted me to answer my questions and discussing my ideas. He was able to create an ideal environment for fruitful research and collaboration resulting in a memorable PhD journey.

I have been also privileged to be co-supervised by Prof Gary Cook and Dr Charalampos Tsoumpas. I would like to thank Prof Cook for sharing his data and medical expertises with me and for being always available to answer any doubts or questions, no matter how busy his schedule was. A very special thank goes to Harry, who accompanied me during my first year and introduced me to exciting world of PET imaging. I am grateful for all the passion he put in supervising me and all the opportunities he gave me.

I also wish to acknowledge all the people that have provided assistance and support throughout my PhD project. Special thanks to Dr Jim O'Doherty for

the time and effort he dedicated for the phantom acquisitions and taught me many useful things about St Thomas' PET centre. I also wish to acknowledge Dr Musib Siddique, Dr Benjamin Taylor and Dr Benedetta Bodini for helping me with the clinical evaluation. I would also like to thank Dr Kris Thielemans for the invaluable support and guidance he gave me during my first months at St Thomas' Hospital. Last but definitely not least a special thanks to Dr Mattia Veronese. He has been an unique collaborator and friend, always enthusiastic and keen on discussing endless project ideas.

I dedicate this thesis to my family who have always been a tremendous source of encouragement throughout my life. A special thanks goes to my mother, without her endless love and support during these past three years I would not have been able to achieve this life milestone.

Contents

List of Figures

List of Tables

Chapter 1

Introduction

Positron Emission Tomography PET offers the opportunity to quantify physiological processes *in vivo* through image visualisation of a targeted body region. The recent development of whole body PET-MRI scanners provide a great amount of additional information to PET imaging. However anatomical images, either computed tomography CT or magnetic resonance imaging MRI, have been mostly used for visualization purposes only and there is a shortage of ad-hoc tools to fully exploit the potential of multimodality imaging. It is in this context that this thesis comes into play. The aim is to develop straightforward applicable tools to improve the resolution of PET imaging by synergistically exploiting the anatomical information provided by CT or MRI. The resolution recovery techniques take advantage of the mutliresolution property of the wavelet transform applied to both functional and structural images to create a high resolution PET image. Two algorithms have been implemented and tested for two different clinical applications, i.e. whole body PET/CT in oncology and brain PET/MR in neurology.

1.1 Thesis Outline

The specific objectives of this thesis are the following:

i to implement and validate a partial volume correction algorithm with a straightforward application in oncology to bone metastases PET/CT imaging

ii to develop a new and more robust partial volume correction algorithm for PET/MR imaging, and specifically, to evaluate the influence of the achieved PVC on multiple sclerosis brain PET/MR images of myelin.

In the first part of **Chapter 2** the reader is presented with a brief description of the basic principles of PET imaging acquisition followed by an introduction to different types of reconstruction algorithms available in the literature. Furthermore, in Chapter 2 is presented the concept of Partial Volume Effect (PVE) and Partial Volume Correction (PVC). Three different groups of partial volume techniques are described with reference to related publications.

In **Chapter 3** is presented the design and acquisition of the three phantom experiments performed to have matched anatomical-functional dataset to test the algorithm implemented for the bone metastases study. The chapter is presented as submitted and published in the 2013 IEEE NSS/MIC Conference Record. A detailed description of phantom preparation and acquisition is described considering that this experiment had not been previously described in the literature.

Chapter 4 and 5 describe the two major projects developed during the past two years. **Chapter 4** describes the implementation of a PET/CT PVC algorithm developed from previous works on PET/MR PVC. The algorithm is validated thanks to the phantom experiments presented in Chapter 3. The results also show the impact on clinical assessment of bone metastases when the PVC algorithm is applied. The Chapter is presented as the article peer-reviewed and published in the *Journal of Nuclear Medicine*. In **Chapter 5** the reader is presented with a second PVC algorithm developed and validated by the candidate. This part of the project aimed to a more robust algorithm that does not require either an anatomical atlas or prior segmentation of anatomical images. Furthermore this new algorithm is able to perform effective PVC also in case of cold lesions such as the ones characterising PET/MR brain scans in Multiple Sclerosis. The algorithm is validated with a dataset of PET/MR scan of both health volunteer and MS patients. The Chapter is presented as submitted to *Neuroimage* for peer-review.

Chapter 6 summarises the findings and outcomes of this thesis and outlines potential areas for future research. In the **Appendix A** is reported a detailed mathematical formulation and description of the wavelet transform considering that it is the core tool used in both the PVC algorithms presented in this thesis.

1.2 Achievements and Contributions

This thesis is the work of the candidate - specific areas where others have contributed specialist input are listed below. The design and acquisition of the phantom experiments have been carried out together with Dr Jim O'Doherty, St Thomas Hospital PET centre. The clinical evaluation of the bone metastases dataset have been performed using the FAST software implemented by Dr Muhammad Siddique, Division of Imaging Sciences, King's College London. The clinical evaluation of the multiple sclerosis dataset have been partially performed with pre-implemented algorithms by Dr Mattia Veronese (Centre for Neuroimaging, King's College London) and Dr Daniel Garcia-Lorenzo (Sorbonne University)

The work presented in this thesis has been funded by a 4 years MPhil/PhD EPSRC scholarship (EP/K502868/1). The initial aim of the project was to investigate a novel way to incorporate anatomical information within the reconstruction algorithm of PET acquisitions. However, after the first year, the aim had to be adjusted due to a change in the project supervision. Dr Tsoumpas who was supervising the project moved to a different University and Prof Turkheimer kindly accepted to take over as the project supervisor and I moved to the Neuroimaging department. Despite the aforementioned changes, the work I have carried out during my first year has been incredibly helpful to get familiar with and understand the complexity behind PET image reconstruction and the factors influencing PET images analysis. These considerations together with a better understanding of the clinical environment helped in outlining the new direction of this PhD project.

During my first year I investigated the influence on the quantification accuracy in PET imaging when different reconstruction algorithms with different settings are used. The findings have been presented at the 2013 IEEE NSS/MIC Conference (Seoul, Korea)

and published as conference records. The investigation dealt with reconstructing phantom and patient data with three different reconstruction algorithms using the Software for Tomographic Image Reconstruction STIR (http://stir.sourceforge.net) and compared the outcome in terms of image quality and clinical impact. Part of the analysis I carried out for this investigation have been integrated as teaching material in the first PET/MRI summer school held in Athens in May 2012 and for the current update of STIR software. In April 2016 I have been awarded with Alavi-Mandell Award by the Society of Nuclear Medicine for my publication on PVC applied to bone metastases. During these three and a half years my work has been published in peer-reviewed journals and conference records as listed below.

Peer-reviewed journal publications

1. **E Grecchi**, J O'Doherty, M Veronese and F E Turkheimer, Multimodal Partial-Volume Correction: Application to 18F-Fluoride PET/CT Bone Metastases Studies, *Journal of Nuclear Medicine*, 56(9):1408-14, 2015

2. **E Grecchi**, M Veronese, B Bodini, D Garcia-Lorenzo, B Stankoff and F E Turkheimer, Multimodal Partial Volume Correction - Application to [11C]PIB PET/MRI myelin imaging in multiple sclerosis, submitted to *Neuroimage*, 2015

Conference records and abstracts

1. **E Grecchi**, J O'Doherty and F E Turkheimer, Exploiting anatomical information for PET image enhancement: A phantom experiment for algorithm validation, in *2014 IEEE Nuclear Science Symposium*, Seattle, USA

2. **E Grecchi**, J O'Doherty, G J Cook and F E Turkheimer, Anatomical-Based Resolution Recovery for 18F-Fluoride PET/CT, in *2014 IEEE Nuclear Science Symposium*, Seattle, USA

3. **E Grecchi**, K Thielemans, G J Cook and C Tsoumpas, Influence of Three Reconstruction Algorithms on the Estimation of the Standardize Uptake Value in 18F-

Fluoride PET, in *2013 IEEE Nuclear Science Symposium*, Seoul, Korea

Publications from collaborations within the PhD time frame

4. **E Grecchi**, O M Doyle, A Bertoldo, N Pavese and F E Turkheimer, Brain shaving: Adaptive detection for brain PET data, in *2014 IEEE Nuclear Science Symposium*, Seattle, USA

5. **E Grecchi**, M Veronese, R M Moresco, G Bellani, A Pesenti, C Messa and A Bertoldo, Assessment of voxelwise quantification of [18F]FDG dynamic PET data in human lung: insight for clinical use, in *2012 World Molecular Imaging Congress*, Dublin, Ireland

Chapter 2

Background and basic principles

In this chapter a brief overview of Positron Emission Tomography (PET) is presented followed by a more focused description of Partial Volume Effect (PVE). Following this, the various existing approaches to reduce partial volume effect are also reviewed.

2.1 Positron Emission Tomography

Positron Emission Tomography is an established non-invasive nuclear imaging modality that produces functional images of the human body by depicting physiological or molecular processes (i,e, blood flow, receptor density and glucose metabolism). Compared with alternative functional imaging modalities such as Single-Photon Emission Computed Tomography (SPECT) it offers greater sensitivity and quantitative accuracy. Moreover, given the relatively shorter half life of most PET radiotracers, high count rate image acquisitions can be performed while maintaining a relatively low patient radiation dose. During a PET exam a patient is injected with a radiotracer solution which travels into the body until it reaches the tissue of interest. A radiotracer consist of a biologically active molecule that has been labelled with an unstable radioisotope. The most commonly used radioisotope in clinical and research PET imaging are 18F, 15O, 11C and 13N. The radioisotope is bounded to a biomolecule targeting specific function in the human body (e.g. glucose analogue to quantify tissue metabolism).

As depicted in Figure 2.1A, when an unstable isotope undergoes positron decay, a positron

and a neutrino are released. The emitted positron travels through the tissue until it interacts and annihilates with an electron (Figure 2.1B). The distance travelled by the positron before its interaction with the electron is typically referred to as *mean positron range* of the nuclide and represent the minimum spatial resolution achievable in PET imaging. The positron range varies from isotope to isotope and it is source of blurring in PET imaging. The interaction between positron and electron produces a pair of high energy 511keV photons ($\gamma - rays$) which travel in opposite directions hitting a pair of detectors (coincidence event) determining a line of response LOR. In order to be recorded as a coincidence event, the two photons have to reach the pair of detectors within specific time and energy windows. These two $\gamma - rays$ are typically emitted with an angle of $180° \pm 0.5°$. This uncertainty in the LOR definition is an additional cause of image blurring in PET. This type of blurring due to the *non-colinearity* of $\gamma - rays$ gets more sever as the distance from the annihilation points to the pair of detectors increase.

Providing that both photons reach the detectors rings without interacting with the surrounding materials, the LOR will intersect the position of the annihilation event (Figure 2.1C). Several annihilation events occur in the targeted region producing a proportional number of LORs which are stored in the form of a sinogram (Figure 2.1D) as a function of the angle of orientation against the displacement from the centre of the scanner. Each point in the singoram accounts for the number of annihilations described by the specific LOR associated with a pair of detectors. Several sinogram are collected, one for each plane and then back-projected into image space by means of a reconstruction algorithm returning the final quantitative 3D PET image.

2.1.1 Image degradation factors

The mean positron range and $\gamma - rays$ non-colinearity are only some of the factors affecting PET image quality that can be further deteriorated by photons that might interact in the patient body resulting in events contributing to background signal. As described in the previous paragraph, a detected LOR corresponds to a coincidence event of two photons originated from the same annihilation (Figure 2.2A). However, not all the de-

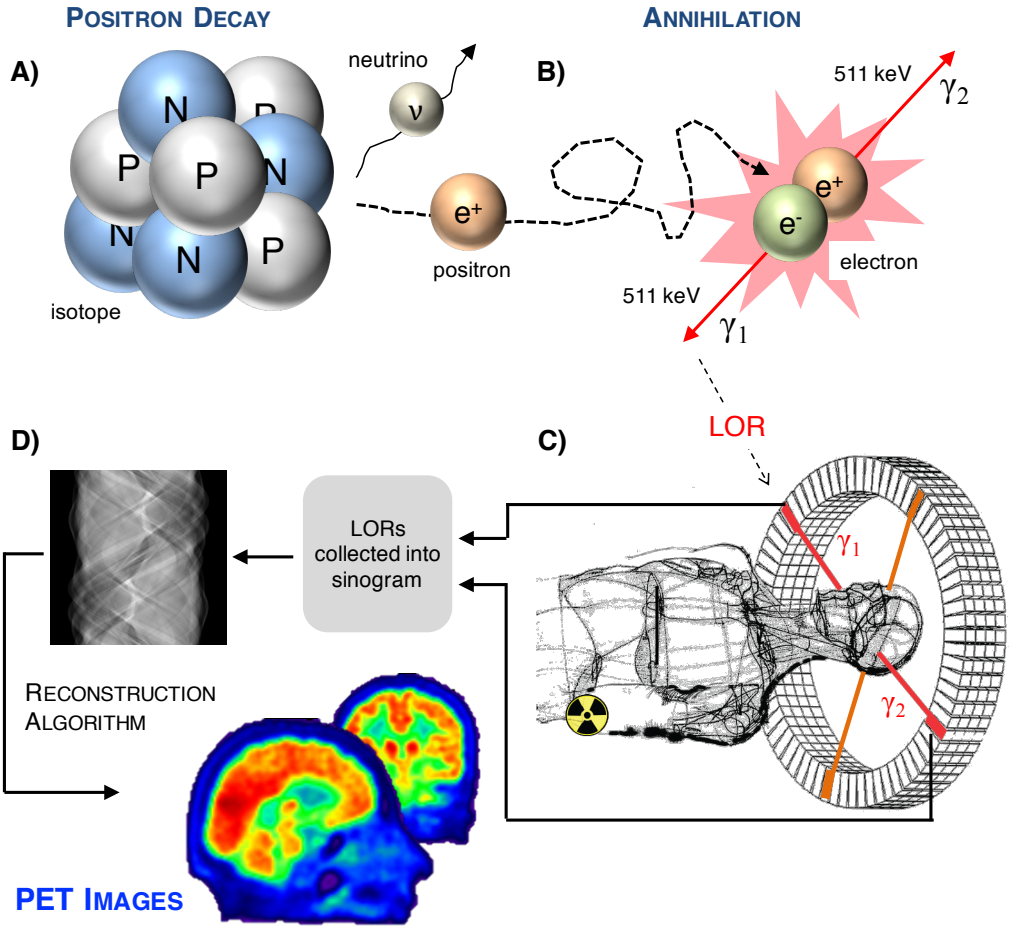

Figure 2.1: **PET Principles** An atom that undergoes positron decay ejects a positron (e^+) and a neutrino (ν). When the positron annihilates with an electron (e^-) two 511 keV photons travelling in opposite direction are produced. A line of response LOR is registered if both photons are detected within a set timing window and different LORs are collected in the form of a sinogram. A reconstruction algorithm is then used to project the PET image back into image space from sinogram space.

tected coincidence events come from ”true” annihilation and some events, as random and scatter coincidence, might be wrongly recorded contributing to image noise. Scatter coincidences occur when one or both photons undergo Compton scattering resulting in erroneous information about the location of the annihilation event, therefore a wrong LOR is recorded (Figure 2.2B). Random coincidences occur when the two detected photons come from different annihilation events and are therefore wrongly recorded as a single annihilation event. This might happen when two positrons annihilate approximately at the same time and one photon from each annihilation is not detected while the other two are (Figure 2.2C). Scatter and random events increase the number of detected events degrading image resolution by adding a background to the true event distribution and decreasing the maximum possible signal to noise ratio (SNR).

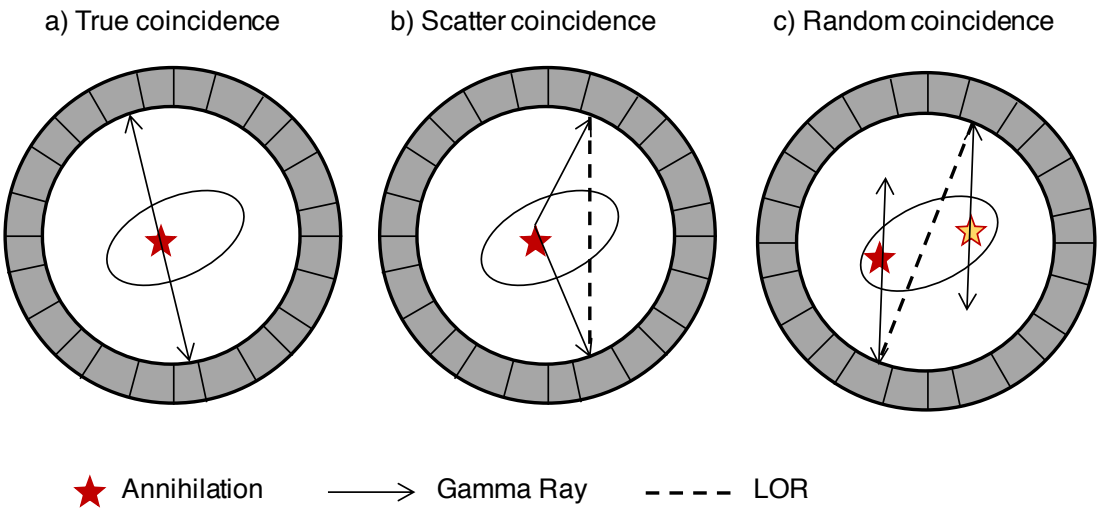

Figure 2.2: True, scatter and random coincidence events

A quantitative measure of PET noise, therefore of the effect of scatter and random, can be described by the noise equivalent count rate (NECR) [110] measuring the performance of an imaging system in term of SNR. The NECR is calculated as

$$NECR = \frac{TrueEvents^2}{TrueE. + RandomE. + ScatterE.} \tag{2.1}$$

Scatter and random events can be estimated and the measured data can be corrected either before the reconstruction in projection space or within reconstruction.

2.1.2 Reconstruction algorithms

In order to produce a 3D image of the radioactivity distribution in the patient, an operation known as image reconstruction is performed. A 3D PET image spatially maps the radioactivity concentration collected into a sinogram in x,y,z space; several algorithms are available to perform this operation and they can be classified into analytic or iterative methods.

One of the first and most commonly used analytic reconstruction method is filtered back projection (FBP) [51] and it provides a direct mathematical solution for the recovery of the radioactivity distribution based on a line-integral model and Fourier theory. Analytic methods are computationally efficient due to the direct solution which simplify the reconstruction. However, they do not take into account the underlying physics of the coincidence detection and statistical noise that may give rise to streak artefacts in the reconstructed images. Filters can be applied before or during the reconstruction [123] to mitigate noise effects but at the expenses of quantification accuracy and image resolution.

Due to these limitations iterative methods gained more popularity demonstrating improved image quality [75, 55]. One advantage of iterative methods is the possibility to incorporate within the reconstruction process models of physical degradation factors, underlying detection physics and the statistical variability of photon detection. Iterative algorithms may improve the image quality in terms of noise and spatial resolution. That is the case for high counts measured data where an accurate system model has high impact on image resolution. However, improvements can be achieved also for low counts measured data where the model of the statistical noise (due to the limited detection of photons) can impact the image resolution as well.

The emission of photons can be modelled as a Poisson process [51] and Rockmore and Macovski [95] formulated the first attempt to include this Poisson model in tomographic reconstruction with a maximum-likelihood ML estimation. However, it was the work of

Shepp and Vardi [103], and independently Lange and Carson [67], who proposed using expectation maximisation EM [32] to maximise the Poisson likelihood that made the ML-EM approach very popular in PET reconstruction.

The measured data are a consequence of nuclear decays, a random process that is statistically variable. For this reason they are usually modelled as random variables characterized by a Poisson distribution [103]

$$y_i \sim Poisson\{\overline{y}_i(\lambda)\} \tag{2.2}$$

The relation between measured data *yi* and expected data x_i, where *i* are projection elements and *j* voxel indexes, can be formulated as

$$\overline{y} = E[y_i] = \sum_{j=1}^{N} p_{ij}x_j + r_j + s_j \tag{2.3}$$

where r_i, s_i represent scatter and random coincidences and $p_{i,j}$ denote the probability of detecting an emission from voxel *j* at detector pair *i*. The matrix $P = p_{ij}$ is known as forward operator or system matrix and includes system geometry, detector response, attenuation and other factors for more realistic modelling of the relationship between image space and projection space [89, 85].

From the above expressions the discrete Poisson probability of expected data can be described as follows

$$p(y|\lambda) = \prod_i e^{-y_i} \frac{\overline{y}i^{y_i}}{yi!} \tag{2.4}$$

with its logarithmic form as

$$\log p(y|\lambda) = L(\lambda) = \sum_{i=1}^{M} y_i \log(\overline{y}_i) - \overline{y}_i - \log(y_i!) \tag{2.5}$$

In order to estimate the expected data *xi*, the log-likelihood $L(\lambda) = \phi(\lambda)$ is the objective

function that has to be maximize with respect to λ_j by the reconstruction algorithm

$$\frac{\partial L(\lambda)}{\lambda_j} = ... = \sum_i \frac{p_{ij} y_i}{\sum_l p_{il}\lambda_l + r_l + s_l} - \sum_i p_{ij} \xrightarrow{maximum} 0 \tag{2.6}$$

A first attempt to include the Poisson model into tomographic reconstruction was made by Rokmore and Macovski [95] with the maximum-likelihood ML estimation formulation. The underlying idea is to iteratively update the radioactivity distribution until it converges to a solution where a defined objective function is maximised. The objective function is a function of the forward modelled sinogram based on the current activity estimate and the measured sinogram. It was the work of Shepp and Vardi [103] as well as Lange and Carson [67] who proposed using the expectation-maximisation EM [32] to maximise the Poisson likelihood that made the ML-EM approach very popular in PET reconstruction. The EM algorithm is a general framework for computing ML estimates through specification of a complete but unobserved dataset.

E-step computes the conditional expectation of the log-likelihood

M-step performs the maximization of the conditional expectation

$$\lambda^{k+1} = \arg\max_{\lambda \geq 0} \sum_j \lambda_j^k \sum_i \frac{p_{ij} y_i \log(p_{ij}\lambda_j)}{\sum_l p_{il}\lambda_l^k + r_i + s_i} - \lambda_j \sum_i p_{ij} \tag{2.7}$$

$$\lambda_j^{k+1} = \frac{\lambda_j^k}{\sum_i p_{ij}} \sum_i \frac{p_{ij} y_i}{\sum_l p_{il}\lambda_l^k} \tag{2.8}$$

The EM algorithm converges monotonically to the solution maximizing the objective function thus at each iteration the updated images will increase the value of the objective function. The main drawback of the EM approach is its extremely slow rate of convergence, thus many attempts have been made in order to speed the convergence up. One of the most widely adopted algorithms is the ordered-subsets expectation maximization OSEM proposed by Hudson and Larkin [53].

The OSEM algorithm divides the complete dataset into a number of disjoint sets known as subsets. The objective function can be rewritten as a sum of sub-objective functions

that is sequentially maximised.

$$\phi(\lambda) = \sum_{q=1}^{N_s} \phi_q(\lambda) \tag{2.9}$$

where N_s is the number of subsets and $S_q \subseteq \{1, 2, ..., M\}$ denotes the collection of the indices in the q_{th} subset. Thus the update equation of OSEM becomes

$$\lambda_j^{(k,q)} = \frac{\lambda_j^{(k,q-1)}}{\sum_{i \in S_q} p_{ij}} \sum_{i \in S_q} \frac{p_{ij} y_i}{\sum_l p_{il} \lambda_l^{(k,q-1)} + r_i + s_i} \tag{2.10}$$

A single iteration is completed once all the subsets have been updated. The convergence speed is directly proportional to the number of subsets; the higher the subset number the faster will be the algorithm convergence since more iterations can be performed for the same time.

Despite its remarkable improvement in the convergence rate at early iterations, OSEM does not fully converge and it is characterized by an increase in noise level at later iterations (as in MLEM). This happens because the low frequency components of the image are resolved at early iterations while the high frequency, including noise, are carried on at higher iterations. Since OSEM requires a high number of iterations to come close to convergence, a noise-resolution trade-off has to be taken into account. An additional common problem to all ML methods in PET is the ill-conditioning of the reconstruction, i.e. small changes in the data cause high variance in the estimates which also contributes to increase the noise level as iterations proceed.

One solution to mitigate the noise deterioration in OSEM reconstruction is to stop the iterations at an early stage; however this might not be the ideal approach since convergence rate depends on noise and object characteristic (low and high frequency). Thus the convergence of different objects in the image is not achieved at the same iterations number.

An alternative approach is to regularise the estimates including a penalisation factor, or *prior*, favouring certain image characteristic (e.g. local smoothing, edge sharpening etc) [38]. The prior term can be included in the ML formulation via a Bayesian formulation scheme or *maximum a posteriori* (MAP) algorithm [50]. Taking advantage of Bayes rule

that defines the posterior density function

$$p(\lambda|y) = \frac{p(y|\lambda)p(\lambda)}{p(y)} \tag{2.11}$$

the objective function that has to be maximised becomes

$$\phi(\lambda) = L(y|\lambda) + \log\, p(\lambda) \tag{2.12}$$

where $p(\lambda)$ represents the prior.

A prior function usually penalizes the intensity variation in adjacent voxel values constraining the final solution. Popular priors are Gibbs distribution functions that use Markov field models and usually rely on additional anatomical information that can be derived from different imaging modality like CT or MR imaging. For example, when anatomical prior information is available, the noise can be reduced within anatomical regions while preserving contours sharpness by allowing larger variation between voxels across boundaries. The formulation of Gibbs distribution priors can be written as follows

$$p(\lambda) = \frac{1}{Z}e^{-\beta U(\lambda)} \tag{2.13}$$

and consequently the MAP formulation becomes

$$\max_{\lambda}\phi(\lambda) = \max_{\lambda}L(y|\lambda) - \beta U(\lambda) \tag{2.14}$$

where $U(\lambda)$ is the energy function and β the penalty factor. The difficulty with solving the equation is highly dependent on the form of the prior energy function $U(\lambda)$ and the iterative approach used for maximization. An efficient way to include the MAP approach in the EM algorithm called one-step-late (OSL) has been proposed by Green [45] where the direct solution of the maximisation step is achieved through the first order Taylor expansion of $U(\lambda)$.

$$\lambda_j^{(k+1)} = \frac{\lambda_j^{(k)}}{\sum_i p_{ij} + \beta\frac{\partial}{\partial\lambda_j}U(\lambda)|_{\lambda=\lambda^{(k)}}} \sum_i \frac{p_{ij}y_i}{\sum_l p_{il}\lambda_l^{(k)} + r_i + s_i} \tag{2.15}$$

where the penalty term is defined using the estimates at previous iterations.

2.2 Partial Volume Effect

The accuracy of the quantification of radiotracer distribution obtained with emission tomography is limited by the poor spatial resolution of the PET imaging system [5]. As described in the previous section there are several factors concurring in degrading image resolution, from positron range and non-colinearity to the choice of the reconstruction algorithm and its ability to reach convergence and cope with the ill-posedness of the reconstruction problem. Not only has the choice of the reconstruction algorithm but also the reconstruction parameters play an important role in defining the final resolution [13]. These can be voxel size, number of iterations and choice of filters that can be applied within or after the reconstruction to control noise level but ending up also degrading the resolution of the reconstructed image.

The poor spatial resolution of PET images is one of the main causes of partial volume effects together with the discrete image sampling. Additional PVE can be introduced by motion (patient, cardiac, respiratory) or, for dynamic studies, by chances in activity distribution due to tracer uptake and washout. It is important to address the causes and mitigate the consequences of PVE because it can be responsible for overestimation of the size of small structure, low sensitivity in the detection of small low-contrast lesions and difficulty in identifying anatomical structures . The limited spatial resolution introduces a 3D blurring in the image responsible for activity spill-out between neighbour regions [107]. While the total activity is preserved (no counts are lost) it is misplaced and spread out in adjacent area and therefore an object can appear bigger in size but lower in activity. The amount of PVE is determined by the size of the object. Larger objects will show blurred edges but the activity in the central area will be likely preserved. Smaller objects will be likely to suffer from PVE when they have a spatial dimension less than 2.5 to 3 times the FWHM of the system point spread function (PSF) [90] (Figure 2.3) that usually tends to be approximated with an isotropic Gaussian function. The effect of the PSF (Figure 2.4) varies within the PET field of view (FOV) due to the non-uniform response of the

detectors. It is smaller in the centre of the scanner and increases towards the detectors as well as being more prominent in the transaxial direction rather than the axial one [73]. As mentioned earlier, the second factor concurring to PVE is related to the discrete image sampling. The tracer distribution inside the body can be seen as a continuous function however, images are sampled using a discrete grid of voxels therefore the tracer distribution may not correspond to the boundaries determined by this grid. For this reason different tissue types might be enclosed in a single voxel and the resulting voxel tracer uptake will be determined by the average of the different tissues activity. This effect is known as *tissue-fraction effect*.

The goal of partial volume correction (PVC) is to improve image resolution reversing the PVE and restoring the true activity distribution of targeted regions. An overview of different PVC approaches is presented in the next section.

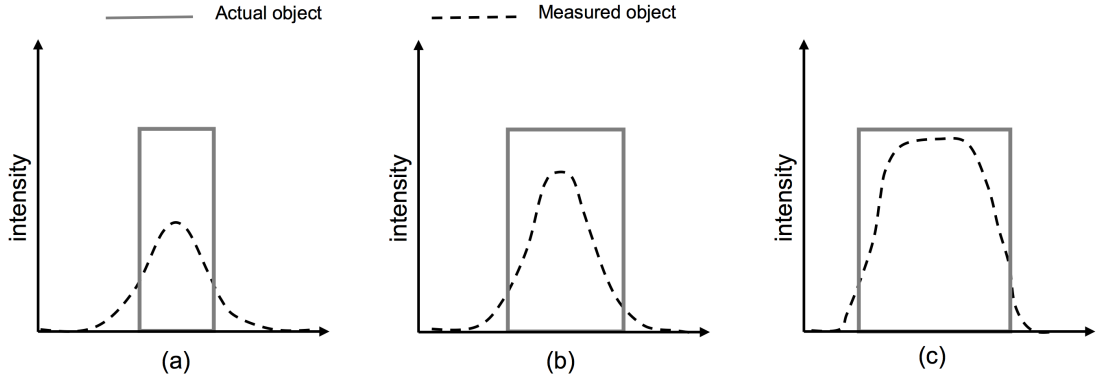

Figure 2.3: Example of the PSF effect on objects of different sizes where the object appears to be larger and have lower activity than it actually does. This effect is particulary relevant for smaller objects (a).

2.3 Partial Volume Correction

Two general categories of PVC techniques are voxel-based and region-based approaches [107], depending on whether the PVC targets a single ROI as a whole or all image voxels. A further classification can be made between PVC techniques that are applied to post-reconstructed images or included during the reconstruction process which can be

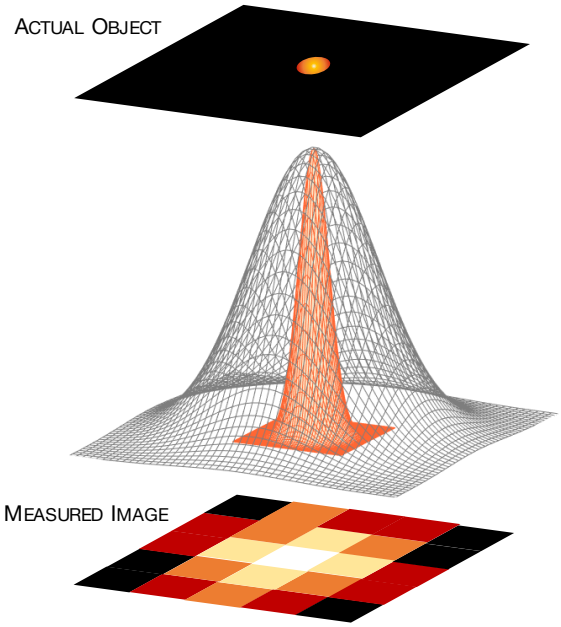

Figure 2.4: **Point-spread function** Schematic depiction of the PSF effect on image acquisition. The Gaussian profile of a point-spread function is sandwiched between the actual object and the measured image.

either region- or voxel- based. Given the popularity of multimodality imaging and the almost ubiquitous availability of anatomical images (CT or MRI) along with PET, some PVC techniques included in the aforementioned categories can be further classified in data-driven (when they rely only on PET data) or anatomical-based (when they take advantage of additional information provided by the anatomical counterpart). As one can see, the possibilities when it comes to PVC are countless. The following sections will give a brief overview of popular techniques belonging to each category for a better understanding of possible approaches to the PVC problem.

2.3.1 Region-based method

Recovery coefficient

Simple and intuitive approaches to PVC are based on multiplicative numerical factors like the resolution Recovery Coefficient (RC) introduced in 1979 by Hoffman et al. [**?**] as the ratio between an object apparent activity and its true concentration. The correction

is performed by multiplying the pixel intensity in a specific region of interest (ROI) with a specific RC. The RC is object dependent (size and shape) thus has to be empirically measured for different PET systems on objects with known activity and known shape. The RC approach found one of its first applications in oncological PVC, as tumour lesions easily approximated to spherical objects. However, the assumption of spherical ROIs is not realistic so RC precalculations are necessary for objects of similar size and shape to the object of interest.

Geometric Transfer Matrix

A method based on spatially-defined regions on anatomical images (MRI) aiming to correct for PVE in multiple ROIs was proposed by Rousset et al [97] and its known as Geometric Transfer Method (GTM). The method requires the segmentation of the co-registered anatomical images into a set of *N* non-overlapping ROIs with the assumption of uniform activity within each ROI. The contribution of each ROI to its neighbours, defined as regional spread function (RSF) has to be computed by blurring each ROI with the system PSF. All the fractional contributions $(\omega_{i,j})$ of each RSF_j inside each ROIi are collected into a matrix to form the following system of linear equations

$$\begin{pmatrix} M_1 \\ \vdots \\ M_N \end{pmatrix} = \begin{pmatrix} \omega_{1,1} & \omega 1,2 & \cdots & \omega 1,N \\ \vdots & \vdots & \vdots & \vdots \\ \omega_{N,1} & \omega N,2 & \cdots & \omega N,N \end{pmatrix} \begin{pmatrix} T_1 \\ \vdots \\ T_N \end{pmatrix} \tag{2.16}$$

where *M* is the mean values in each ROI while *T* its true activity. The true activity can be then obtained as follows:

$$T = \omega^{-\mathbf{1}} M \tag{2.17}$$

As from the above equations, the result obtained is not an image but the true average activity concentrations of each ROI corrected for spill-over between adjacent ROIs. The GTM method is widely applied since it can account for spill-over effects between different regions, however it does not provide a partial volume corrected image and stems from

the assumption of uniform ROIs activity, quite unrealistic especially in oncology due to tumour heterogeneity.

From PET raw data

Region-based techniques can be also applied in sinogram space rather than image space. This idea was initially proposed by Huesman et al [54] and further developed to improve robustness towards statistical noise and ROIs definition [20, 80, 39]. The idea is to define a ROI on the structure of interest and forward project just the selected in sinogram space. The raw data are then convolved with a filter function accounting for the blurring effects and back projected into image space. This approach is quite fast because only a portion of the complete image is involved in the reconstruction process. Later on Carson [20] included this approach into a MLEM reconstruction to account for the Poisson statistic of noise while a similar approach based on a least square optimization was proposed by Formiconi [39]. In order to make the ROIs definition more robust Moore [80] extended this approach to exploit multimodality imaging (PET/CT, PET/MRI) by segmenting few tissue types of a neighbour area around the ROI.

2.3.2 Voxel-based method

Reconstruction based methods: *PSF and Anatomical Priors*

There are two possible ways to achieve PVC at voxel-level during the reconstruction process that can be either applied separately or together. One is to include information about the system PSF in the reconstruction algorithms [85, 112], the other is to use matched anatomical information, for example as a regularization term in MAP iterative reconstruction [6, 84, 14]. Partial Volume Correction can be performed incorporating a model of the PSF in the system matrix used for back- forward- projection during the reconstruction [29, 85, 3]. First of all a careful modelling of the system matrix is necessary [1, 89] but also a model describing the PSF is necessary. Defining an accurate PSF model might not be that straightforward. Monte Carlo simulations can be accurate but they require long computational times and need of detailed knowledge of the system design. Alternatively,

the PSF can be empirically measured but, despite being a conceptually easy approach, in practice is not that easy to acquire a point source covering all the field of view [92, 43, 65]. As already mentioned in the *Reconstruction Algorithms* section, to obtain a significant recovery of true PET signal, an iterative algorithm should run up to convergence or at least for a high number of iterations. Not only a high number of iterations affects the amount of image noise but also exacerbate the appearance of Gibbs (or edge) artefact intrinsic of PSF-based reconstruction [117, 114]. The use of an anatomical prior can help with noise control while preserving image boundaries thus improving structures resolution. PVC can be performed targeting the smoothing effect of a regularisation prior in MAP reconstruction to specific ROIs derived from segmentation of high resolution anatomical images such as CT and MRI. A first group of techniques uses anatomical information together with Gibbs smoothing prior weighting [28]. Within these are priors based on intensity distribution analysis. Bowsher et al. [18] proposed a prior where higher probabilities are assigned when voxels stayed within anatomical boundaries promoting greater smoothing among nearby voxels. Lipinski et al. [70] and Baete et al. 2004 [6] assumed a gaussian distribution for voxels within specific anatomical regions while Sastry and Carson 1997 [100] described images as a sum of activities for different tissue types. A third class of prior is based on similarity measures (e.g mutual information and entropy) between voxels such as the minimum cross-entropy [4] or joint-entropy and mutual-information [84, 86, 106]. Recent studies comparing anatomical based priors in brain data [56, 127] have suggested that reconstruction methods incorporating priors provide good preservation of lesion contrast whereas post-reconstruction methods reduce bias in regional quantification, although accurate image segmentation and registration is required. While in brain studies these can be a conquerable limitation, tissue segmentation and image co-registration are not as straightforward for whole body scans, especially in the presence of patient motion. An additional limitation to routine application of anatomical priors in clinical practice is the requirement to tune specific parameters for each acquired dataset.

Image deconvolution

A simpler way to include a model for the PSF is to account for its effect directly in image space through image deconvolution. The idea behind the deconvolution approach is to reverse the blurring effect directly in image space given the following convolution model for the "blurred" image $b(\bar{x})$

$$b(\bar{x}) = t(\bar{x}) * h(\bar{x}) \tag{2.18}$$

where $t(\bar{x})$ represent the "true" unblurred image, $h(\bar{x})$ a model describing the PSF in the $\bar{x} = (x, y, z)$ space and $*$ denotes a 3-D convolution. From the equation above it is clear that the noise component is not taken into account; this is a notable simplification since the PSF itself does not account for all the image resolution deterioration. The deconvolution process to estimate the true image t from the observed image b is then an ill-posed problem similarly to the reconstruction one therefore iterative solving techniques are commonly used. Many iterative approaches have been proposed which rely either the Van Cittert (CT) algorithm [**?**, **?**] or the Richardson-Lucy (LC) algorithm [**?**, **?**] to iteratively solve the equation under a positive constraint. The main drawback of this class of PVC techniques is the excess noise amplification as iteration proceed, thus the need of including a regularization term.

Partition methods

Partition methods belong to the post-reconstruction anatomical-based PVC category. They require segmentation of spatially co-registered anatomical images into two or more tissue types before applying the PVC at voxel level for each segmented region. A first attempt has been made by Videen et al [126] where brain is segmented into two regions, brain and non-brain, where the former is the corrected for the effect of the latter. The mask of the brain region is convolved with the system PSF to create a brain image of resolution coefficients (RCs). The voxel ratio between the original PET image and the RCs images is then computed to obtain a PVC brain PET image. The method has been extended to 3D images by Metlzer et al [76] and later on to include segmentation of three

tissue types on MRI images by Müller-Gärtner et al [82] (MG). The MG method requires segmentation into white matter (WM), grey matter (GM) and cerebrospinal fluid (CSF) and then calculate a GM PVC image by subtracting from the original PET the spill-in contribution of WM and CSF and finally corrects for GM spill-out as well. This method also requires a convolution of WM and CSF images with the scanner PSF and assumes tracer uniform uptake in the target region.

Segmentation into three tissue classes can be a limiting factors if one is interested in a more functional-based tissue segmentation. Yang et al [131] modified the MG method to be flexible in considering multiple ROIs, although requiring a priori knowledge of activity concentration ratio among ROIs. To overcome this limitation Thomas et al [116] suggested to exploit the GTM approach to estimate instead the a priori activity information. Of course all these approaches are susceptible to mis-determination of the system PSF as well as mis-registration between anatomical and functional images.

Anatomical information in image space

An alternative image-based approach that uses anatomical information to improve PET resolution is to transfer the high-frequency information from the high-resolution anatomical image to the low-resolution PET. Several examples, usually relying on a wavelet transformation of both functional and anatomical images, are reported in literature [15, 104, 69, 41]. These methodologies are straightforward to apply since they only require coregistration of the two imaging modalities without the need for tuning additional parameters or a priori assumptions about tracer distribution within ROIs. On the other hand these algorithms are necessarily dependent on the accuracy of image coregistration thus they have been mainly applied to brain studies even though good results have been reported for oncological [16] and cardiac [11] applications as well. Further discussion and description of these methodologies is reported in Section 2.5 considering their relevance for the work presented in this thesis. Prior to that, Section 2.4 will report a detailed description of the wavelet transform.

2.4 Wavelet Transform

The Fourier transform is a fundamental tool in signal processing. However, it suffers from major limitations when it comes to non-stationary signals, namely signals that have time varying frequency. In a broad sense, images are an example of transient signals that can be effectively represented by localized finite-energy bases, contrary to Fourier decomposition [24].

Biomedical images, PET images in the specific case, are a perfect example of signal requiring analysis methods able to discriminate events that occur at the opposite extremes of time-frequency domain. Wavelets represent indeed an optimal finite-energy base to localize the information in the time-frequency domain being capable of trading one type of resolution for the other [121].

2.4.1 Wavelet Domain

From Fourier theory it is known that a signal can be expressed with a Fourier expansion as an infinite sum of cosines and sines. A major drawback of this type of analysis is the ability of providing only frequency resolution but no time resolution. In other words, one might be able to determine all the frequencies present in a signal without knowing when they occur.

In order to achieve a joint time-frequency representation one can cut the signal in several parts which are then analysed separately. The frequency components remain while adjoining information about when they actually occur. Cutting the signal is equivalent to performing a convolution between the signal itself and a *cutting window* in the time domain (or alternatively a multiplication in frequency domain). Thus, the time-frequency resolution strictly depends on the cutting window that has to be chosen wisely.

For example the Fourier transform of a short time cutting window such as the Kronecker delta contains all possible frequencies, hence the signal transform will broaden through the entire spectrum (Figure 2.5).

This extreme example shows opposite behaviour than a standard Fourier transform, hav-

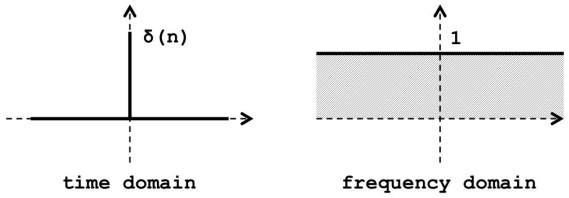

Figure 2.5: Graphical representation of Kronecker Delta in time domain (left panel) and its spectrum obtained with a Fourier Transform (right panel)

ing now information on time resolution while lacking frequency one. From the previous examples it follows, for the Heisenberg's uncertainty principle applied to signal processing, that it is impossible to simultaneously know the exact frequency and the exact time of occurrence of the same frequency. The wavelet analysis represents a solution for this cutting signal problem leading to a signal representation in time and frequency domains simultaneously. The basic idea is to use a cutting window that is shifted along the signal and calculate the spectrum for each of these shifted positions (translation). This process is then iterated changing the window size (dilation). The result is a collection of time-frequency representations with different resolutions (from different window size, Figure 2.6A), hence the definition of *multiresolution analysis*. The goal of multiresolution analysis is to apply the divide and conquer strategy: separate the signal in multiple components that can be independently analysed and processed by different algorithms.

2.4.2 Continuous Wavelet Transform

Let's define the function $\psi(t)$ called *mother wavelet* as follow

$$\psi_{\tau,\sigma}(t) = \frac{1}{\sqrt{\sigma}}\psi\left(\frac{t-\tau}{\sigma}\right) \tag{2.19}$$

where σ is the scale factor (dilation), τ the translation factor and ψ represents a basis function that can be designed to taste as long as it fulfils general wavelet properties (*admissibility, regularity and vanishing moments* [19][31][102]).

The *Continuous Wavelet Transform CWT* of a signal $f(t)$ is its decomposition into a set

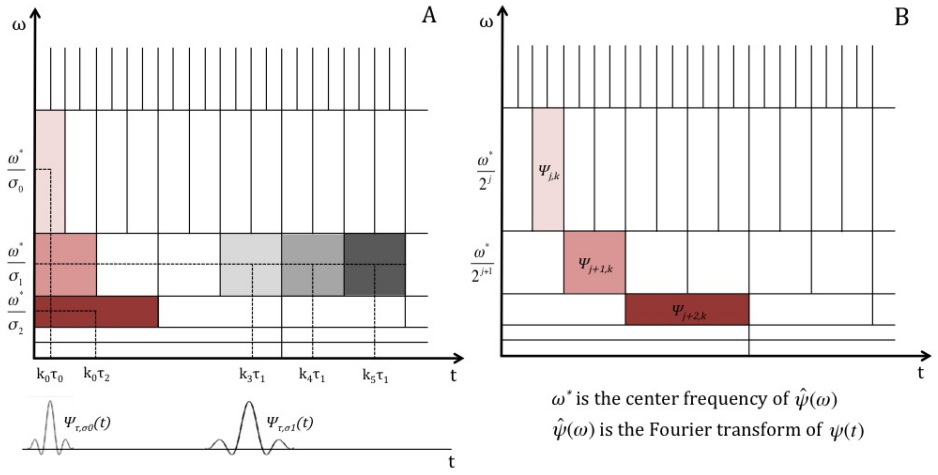

Figure 2.6: Frequency bands and time window tiling for generic discrete wavelet function (A) and dyadic wavelet transform (B). The grid in A refers to equation 2.19 and shows the influence of different dilation (red blocks) and translation (grey blocks) in time-frequency windows. The grid in B refers to equation 2.23 the shows the influence of different resolution levels in time-frequency windows for fixed dilation and translation

of wavelets functions $\psi_{\tau,\sigma}(t)$

$$W_\psi f(\tau,\sigma) = \int_{-\infty}^{\infty} f(t)\overline{\psi_{\tau\sigma}(t)}d(t) \tag{2.20}$$

where the continuous overbar indicates complex conjugation.

Let's analyse a bit further equation 2.20 and consider two arbitrary functions $x(\cdot)$ and $y(\cdot)$ defined in a finite-energy space L^2; one can represent their inner product as

$$\langle x, y\rangle = \int_{-\infty}^{\infty} x(\cdot)\overline{y(\cdot)}d\cdot \tag{2.21}$$

hence equation 2.20 becomes

$$W_\psi f(\tau,\sigma) = \int_{-\infty}^{\infty} f(t)\overline{\psi_{\tau\sigma}(t)}d(t) = \langle f(t), \psi_{\tau\sigma}(t)\rangle \tag{2.22}$$

meaning that the CWT computes, through the inner product, the wavelet coefficients of $f(t)$ associated with the wavelet function $\psi_{\tau\sigma}(t)$. These coefficients measure the correlation between the two functions: higher correlation produces higher coefficients.

By definition the *CWT* is calculated by continuously shifting a continuously scalable func-

tion over a continuous signal. The process clearly produces a high redundancy of these scaled functions with a consequent high computational load, which isn't ideal for most practical applications.

To alleviate this computation burden the *Discrete Wavelet Transform DWT*, where dilations and translations are performed in discrete steps, has been proposed as a variation of the *CWT*.

2.4.3 Dyadic Wavelet Transform

Starting from equation 2.19 a fixed dilation step σ_0 and a translation factor τ_0 depending on the dilation step are now introduced

$$\psi_{j,k}(t) = \frac{1}{\sqrt{\sigma_0^j}}\psi\left(\frac{t - k\tau_0}{\sigma_0^j}\right) \tag{2.23}$$

A common choice for computational efficiency is to fix $\sigma_0 = \frac{1}{2}$ and $\tau_0 = \sigma_0^j$ which correspond to a binary dilation (i.e. dilation by 2^j) and a dyadic translation ($k/2^j$), the so called *Dyadic Wavelet Transform DWT*

$$\psi_{j,k}(t) = 2^{j/2}\psi(2^j t - k) \tag{2.24}$$

A *wavelet series decomposition* is defined when discrete wavelets (equation 2.24) are used to transform continuous signals producing a series of wavelet coefficients (as for the continuous case of equation 2.22).

Together with redundancy reduction, a second advantage of performing wavelet series decomposition is the possibility of producing an orthonormal basis. Indeed, a function $\psi \in L^2$ is an orthogonal wavelet when its family $\{\psi_{j,k}\}$ is an orthonormal basis of L^2, meaning that

$$\langle \psi_{j,k}, \psi_{l,m} \rangle = \delta_{j,l} \cdot \delta_{k,m} \qquad j,k,l,m \in \mathbb{Z} \tag{2.25}$$

hence any function $f(t) \in L^2$ can be written as

$$f(t) = \sum_{j,k} d_{j,k}\psi_{j,k}(t) \tag{2.26}$$

The representation in equation 2.26 is called *wavelet series* and shows that a signal can be reconstructed (inverse wavelet transform) via a weighted sum of orthogonal wavelet basis functions. The weighting factors are the wavelet coefficients $d_{j,k}$ that, analogously to the continuous domain, result from the inner product

$$d_{j,k} = \langle f(t), \psi_{j,k}(t) \rangle \tag{2.27}$$

From equation 2.24 and Figure 2.6 it is clear that the wavelet bandwidth depends on the scaling factor 2^j. As the resolution level j increases the bandwidth is halved (1, 0.5, 0.25, 0.125, 0.0625 ...) and shifted by a factor of 2. This means that theoretically an infinite number of wavelets are needed to cover the entire spectrum (Figure 2.7A) because for increasing value of j only half of the remaining spectrum is covered.
A solution is to introduce, alongside with the wavelet function $\psi_{j,k}$, a scaling function $\varphi_{j,k}$ [72] aiming at filling that portion of the spectrum that remains otherwise uncovered when the analysis stops at a desired resolution level J (2.7B).
At this point the signal at a specific resolution level j can be expressed as

$$f^j(t) = \sum_k d_{j-1,k}\psi_{j-1,k}(t) + \sum_k c_{j-1,k}\varphi_{j-1,k}(t) \tag{2.28}$$

The whole signal $f(t)$ results from taking into consideration $\psi(t)$ for all the resolution levels and $\varphi(t)$ for the finer one only

$$f(t) = \sum_j^J \sum_k d_{j,k}\psi_{j,k}(t) + \sum_k c_{J,k}\varphi_{J,k}(t) \tag{2.29}$$

Over time different wavelet functions (and the related scaling function) have been proposed as suitable to provide good time and frequency localization [2]. In Figure 2.8 is

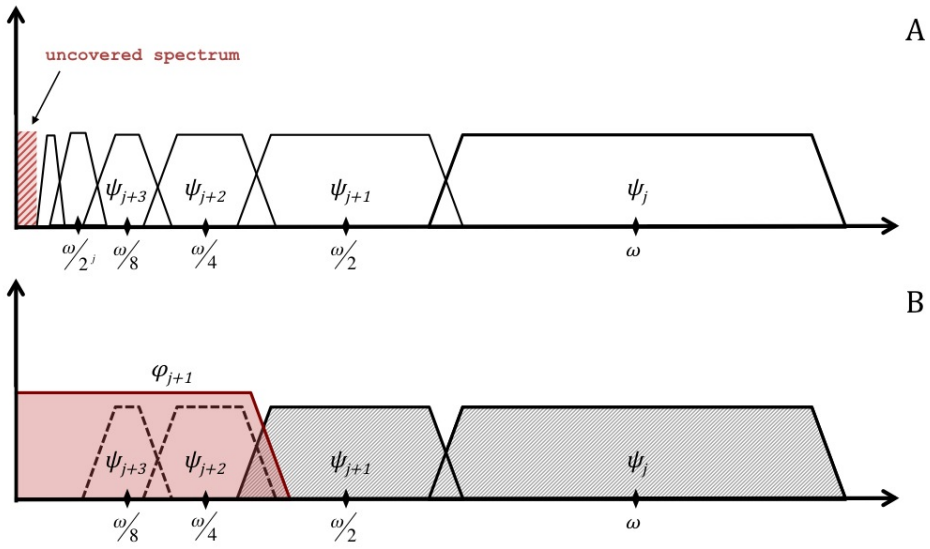

Figure 2.7: Graphical representation of wavelet spectra coverage. Trapezoid elements represent the spectra of dilated wavelet ψ for each resolution level j. The ratio between the centre frequency of a wavelet spectrum and the width of the spectrum itself is the same for all wavelets at different resolution levels j. **Panel A** shows that ideally an infinite number of wavelets is required to cover the entire spectrum since at each resolution level the wavelet stretches to cover only half of the remaining spectrum. **Panel B** shows the role of the scaling function φ (red element) that aims to cover the remaining portion of the spectrum when the analysis stops at a desired resolution level j. For the specific example reported in panel B the transform of signal $f(t)$ up to resolution level $j+1$ is described by two wavelet functions ψ (grey elements) and one scaling function φ (red element).

reported with sole illustrative purpose the Battle-Lemarie wavelet function [7].

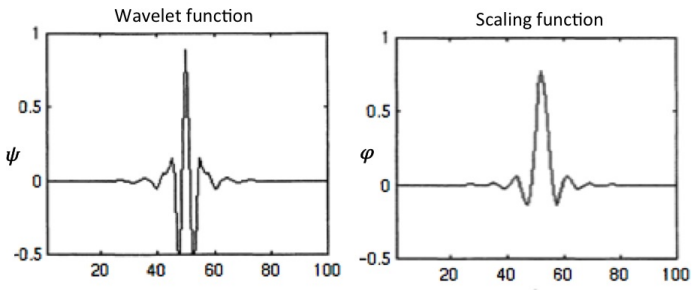

Figure 2.8: Representation of the Battle-Lemarie wavelet basis. Left panel wavelet function. Right panel scaling function.

2.4.4 Filter Implementation

Previous sections described the role of wavelet and scaling functions and relative coefficients for signals representation; this section will explain how these coefficients can be estimated.

Let's define two subspaces in the finite-energy space L^2

$\{V_j\}$ of L^2 generated by $\varphi_j(t)$

$\{W_j\}$ of L^2 generated by $\psi_j(t)$

where both functions satisfy the same dilation equation as 2.24

$$\varphi_j(t) = \sum_k l_{k,j}\varphi(at-k) \xrightarrow{dyadic} \sum_k l_{j,k}\varphi(2^j t-k) \tag{2.30}$$

As partially illustrated in Figure 2.7B and better depicted in Figure 2.9, every subspaces V_n (at the arbitrary resolution level n) can be seen as an orthogonal sum of mutually orthogonal subspaces W_j given $j < n$

$$V_n = \oplus_{j=-\infty}^{n-1} W_j \tag{2.31}$$

The equation 2.31 and Figure 2.9 describe a two-scale relation between basis functions

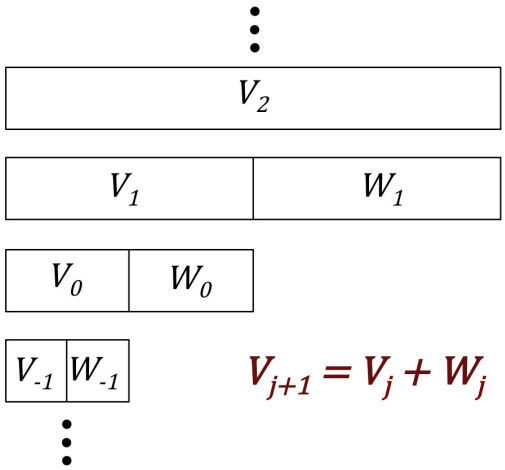

Figure 2.9: Approximation of wavelet subspace relationship. For each resolution level j the subspace (V_i) generated by the scaling function is described as the sum of the subspaces generated by wavelet (W_{j-1}) and scaling function (V_{j-1}) at a finer resolution level.

that can be formalized as

$$\varphi(t) \in V_0 \subset V_1 \tag{2.32a}$$

$$\psi(t) \in W_0 \subset W_1 \tag{2.32b}$$

When equation 2.31 is combined with the relations expressed by 2.32 the result is as follow

$$\varphi(2^0 t) = \sum_k \ell_{k,1} \varphi(2^1 t - k) \tag{2.33a}$$

$$\psi(2^0 t) = \sum_k h_{k,1} \psi(2^1 t - k) \tag{2.33b}$$

that can be generalized as

$$\varphi(2^j t) = \sum_k \ell_{k,j+1} \varphi(2^{j+1} t - k) \tag{2.34a}$$

$$\psi(2^j t) = \sum_k h_{k,j+1} \psi(2^{j+1} t - k) \tag{2.34b}$$

When comparing Figure 2.9 with Figure 2.10 (which shows symmetries with Figure 3) and relating equation 2.28 with equations 2.34, the wavelet transform can be regarded as a filter bank where the output at different stages are the wavelet- and scaling coefficients.

More specifically, the wavelet function coefficients $d_{j,k}$ will result from a high-pass filter $\mathscr{H}(k)$ while the scaling function coefficients $c_{j,k}$ from a low-pass filter $\mathscr{L}(k)$ both applied to the scaling function resulting from the previous resolution level (Figure 2.11).

$$c_{j-1,k} = \sum_m \ell(m-2k)c_{j,k} \tag{2.35a}$$

$$d_{j-1,k} = \sum_m h(m-2k)c_{j,k} \tag{2.35b}$$

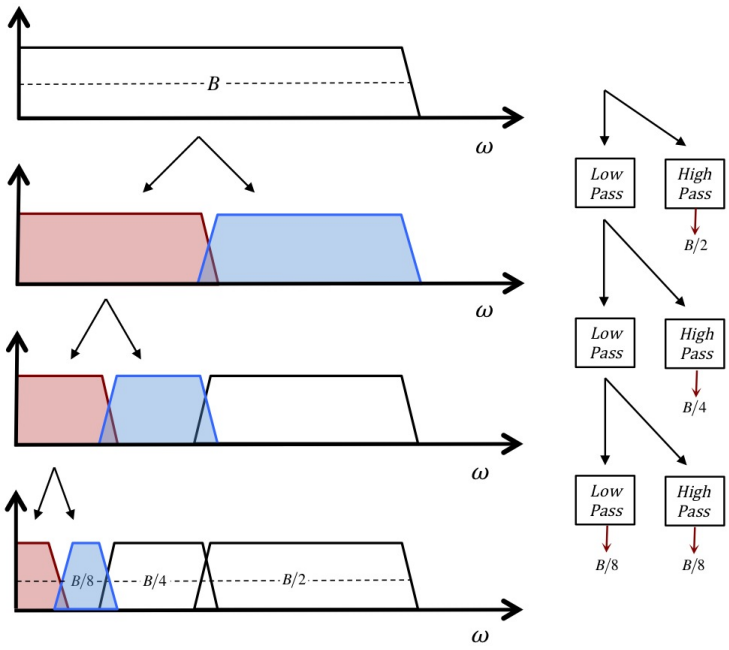

Figure 2.10: Graphical representation of the splitted signal spectrum through an iterated filter bank. The scaling function (red element) and wavelet function (blue element) result from the application of a low-pass (the former) and high-pass (the latter) filter to the scaling function of the previous level.

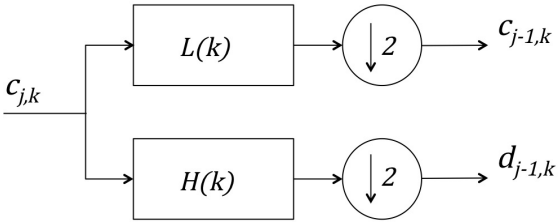

Figure 2.11: Implementation of equations 2.35 as one stage of an iterated filter bank

2.4.5 Multi-Dimensional Wavelets

In imaging application the input signal is no longer mono dimensional therefore its components have to be represented by n-dimensional wavelets and scaling functions (generally 2D or 3D). The 2D case formalized by equations 2.36 is described by three 2D wavelets and one 2D scaling function that generate 4 subimages starting from the original (for m dimensions the number of subimages at each level increases to 2^m). The algorithm generates four components from a 2D input signal while applying the one-dimensional decomposition (low- and high-pass filters) successively along the rows and columns and decimating the outcome in half (Figure 2.12A). The scaling function coefficients resulting from the application of the low-pass filter $\mathscr{L}(\cdot)$ to both rows and columns are the input for the second level wavelet decomposition.

$$\begin{cases} \psi_1^{(j)} = \psi_{a,b}^1 = \varphi(x-a)\psi(y-b) \rightarrow LH \\ \psi_2^{(j)} = \psi_{a,b}^2 = \psi(x-a)\varphi(x-a) \rightarrow HL \\ \psi_3^{(j)} = \psi_{a,b}^3 = \psi(x-a)\psi(y-b) \rightarrow HH \\ \varphi^{(j)} = \varphi_{a,b} = \varphi(x-a)\varphi(x-a) \rightarrow LL \end{cases} \tag{2.36}$$

The outcome of the 2D decomposition is visually described in Figure 2.12B where, for each resolution levels the algorithm generates four quadrants. Three quadrants contain the wavelet coefficients describing vertical (HL), horizontal (LH) and diagonal (HH) details while the remaining upper-left quadrant (LL) contains the residual coefficients of the scaling function. When the 2D wavelet is applied in the same fashion to the coarse resolution quadrant LL the result is the second resolution level analysis.

For what concern the 3D case ($m = 3$) the first resolution level decomposition results in 8 different sub-volumes (Figure 2.13). Analogously for the 2D analysis the one-dimensional decomposition is applied successively along all dimensions; this time together with rows and columns there is the image depth in the z direction that has to be considered as well. The coarser resolution quadrant (that is the input for the following resolution levels analysis) results again from the application of the low-pass filter along all directions x,y

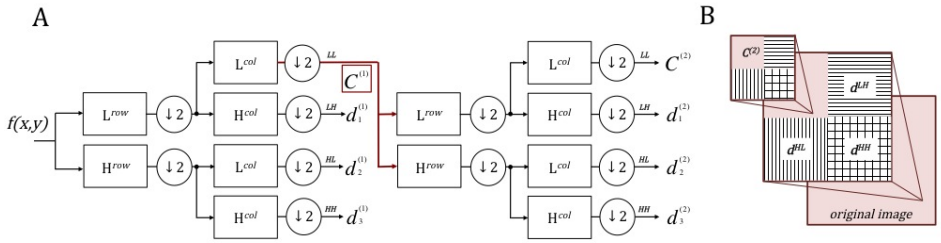

Figure 2.12: A) Two levels of a quaternary separable wavelet tree used for two-dimensional signal. Row filtering is denoted by the superscript *row* while column filtering by the superscript *col*. d^j and C^j are respectively the wavelet and scaling coefficients for resolution level j. B) Graphical representation of the application of 2D DWT. After each resolution level the output is made of three quadrants containing horizontal (LH), vertical (HL) and diagonal (HH) details plus a coarse residual quadrant that is the input for the second level analysis

and z.

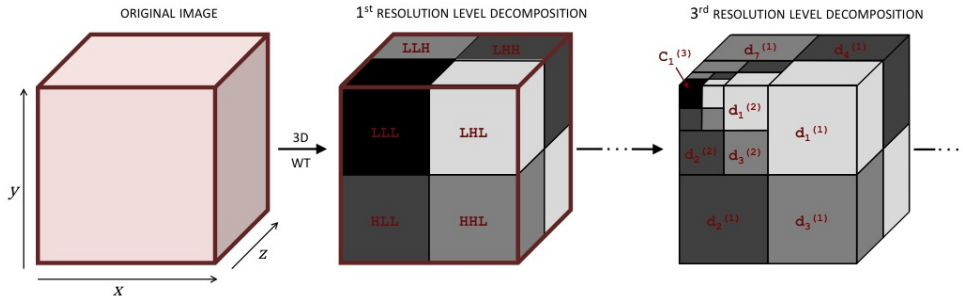

Figure 2.13: Graphical representation of the output of the DWT applied to a 3D image. The concept is similar to the 2D representation of Figure 2.12B. After the first resolution level analysis the output consists of 7 blocks containing wavelet coefficients describing horizontal, vertical and diagonal details plus one block (LLL) containing the coarse residual that is plugged in to the second level of analysis and so on.

2.4.6 Dual-Tree Wavelet Analysis

The majority of wavelet based algorithms developed for medical imaging analysis stem from the Dyadic Wavelet transform [72][71] described in the previous section. Although DWT works well for signal compression, when it comes to multimodality image analysis its applicability is hampered by three main disadvantages.

In the first instance the lack of shift invariance is responsible for major variations in energy

distribution of wavelet coefficients at different scales when there are small variations in the input signal. Because of the shift dependence, the DWT might not be the optimal choice for detecting key features in images.

In addition, due to the separable and real nature of the low- and high-pass filter the DWT is characterized by poor dimensionality selectivity, which can be a major drawback when one is interested in the detailed structural content of anatomical images. Finally the reconstruction from wavelet domain to image domain is sub-optimal due to the post filtering output decimation that is however necessary to reduce redundancy and computational burden.

In his work Kingsbury [61] [60] proposed a *dual-tree complex wavelet transform* (DT CWT) to overcome DWT limitations in order to achieve better directionality selectivity, shift invariance and perfect reconstruction while keeping limited redundancy.

The shift invariance and directional selectivity issues can be both effectively addressed by means of a *complex wavelet transform* CWT. However, perfect reconstruction is difficult to achieve with CWT after resolution level 1 analysis hence a different approach to generate a complex filter tree is needed.

The same achievements of the CWT in term of shift invariance and directionality selectivity can be obtained with a real DWT by doubling the sampling rate at each filtering level. From Figure 2.12A one can notice that this is equivalent to eliminate the down-sampling $(\downarrow 2)$ that results in having two parallel trees, a and b, as outlined in Figure 2.14A. The two parallel trees result from the delays of the high- and low-pass filters $\mathscr{H}(\cdot)$ and $\mathscr{L}(\cdot)$. The shift invariance is preserved when the delays of two trees are half a sample different, meaning that *odd-length* filters are used in one tree and *even-length* filters in the other. Figure 2.14B shows the position of wavelet and scaling basis functions when the filters are arranged to be odd and even (the reader is referred to compare Figure 2.14A with Figure 2.8 to appreciate the difference between basis functions in DWT and DT-CWT).

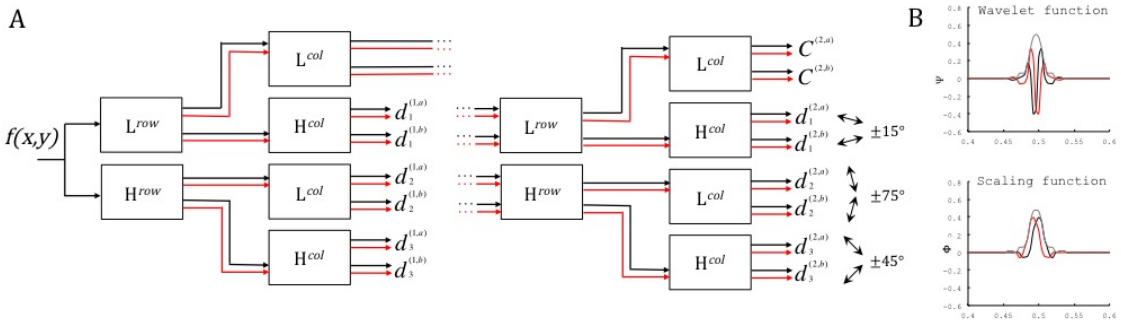

Figure 2.14: A) Two levels of the complex wavelet tree for a real 2D input signal $f(x, y)$ resulting in wavelet coefficients describing six directional bands at each level (black double ends arrow). The real and complex components of the tree are represented with different colors (black and red respectively). B) Impulse response at level 1 of the DT-CWT of the wavelet and scaling functions. They are equivalent to the basis functions of the odd and even filters used to double the sampling rate.

2.5 Wavelet approaches to PVC

One way to generate PVC images using spatially co-registered high-resolution anatomical images is by exploiting the characteristics of wavelet transform and multi-resolution analysis to transfer high-frequencies (boundary information) from anatomical to functional images. The wavelet transform is an interesting mathematical tool that allow a simultaneous representation of spatial and frequency domain resulting in an image presenting different contrast and structure depening on the for of the wavelet basis used. Furthermore it enables work at different levels of spatial resolution, operating as a tool of multiresolution analysis. For a more detailed description of the wavelet transform the reader is referred to Paragraph 2.4.

Wavelet transform is a powerful tool for PET image processing given its inherent ability to provide both space and frequency localization [99, 122]. However, when the analysis involves image noise characteristics or wavelet coefficients variance, some technical developments are necessary since the white noise conditions considered in standard wavelet procedures are not valid for Poisson distributed PET images [120].

á trous algorithm A first attempt to achieve PVC of PET images exploiting wavelet characteristics has been made by Boussion et al [15]. To start with, images are trans-

formed from image to wavelet space via the *á trous* algorithm and decomposed up to a common resolution level. Assuming a correlation between the wavelet coefficients in the two images, a linear model is established between the anatomic and functional details at lower resolution level. If the level of resolution of the structural image H is *q*, referred as H_q, and that of the PET image L is $r = q + p$ one can write

$$L_{q+p}(x, y) = L_{q+p+1}(x, y) + w^L_{q+p+1}(x, y) \tag{2.37}$$

$$H_{q+p+1}(x, y) = H_{q+p+1}(x, y) + \sum_{k=1}^{k=p+1} w^H_{q+k}(x, y) \tag{2.38}$$

where w_k denotes the layers of details at the specific resolution level. The linear model describing the relationship between L and H is applied to the high resolution details of the anatomical image in order to obtain the lacking ones in the functional image. Thus the resolution level L_q can now be reconstructed from the previous known resolution level as

$$L_q(x, y) = L_{q+p+1}(x, y) + \alpha \sum_{k=1}^{k=p+1} w^s H_{q+k}(x, y) \tag{2.39}$$

where the parameter α is defined as the mean of the voxel by voxel division between the functional wavelet coefficients and the anatomical ones. This method requires the assumption of perfect correlation between the two imaging modalities given the linear model used to correct the details that are then added to the original image. This may lead to artefact appearance, especially if structures belonging to the anatomical image are not in the functional one.

Denoising A similar approach to the one introduced by Boussion et al has been introduced by Turkheimer et al [119] to enhance the signal-to-noise ratio via image denoising. Contrary to the original approach, here the author postulates a stochastic model to relate structural and functional information to relax the assumption of a simple linear scalar model. Furthermore, since the final goal is to achieve denoising instead of adding additional high frequency information to the PET, the anatomical images are degraded to the same resolution as the PET one and not vice-versa.

The anatomical images are initially blurred with a Gaussian filter to match the PET resolution and then both images are transformed into wavalet space using a dyadic wavelet transform DWT (see Section 2.4.3). As before, PET wavelet coefficients are replaced by those of the structural one after appropriate scaling obtained through an appropriate stochastic model. To start with a linear relation is defined between the correspondent wavelets in the functional image L and those in the structural image

$$L_i(w) = \alpha_i(w)H_i(w) + b_i(w) + \varepsilon(w) \tag{2.40}$$

where i is the resolution level and $w = [s/2^i]$ for each pixel s. The linear model is applied locally instead of globally. The model can be resolved using a least square approach. The term $\varepsilon(w)$ is assumed to be a gaussian process but this assumption is not supported any more in case of iteratively reconstructed images. If this is the case variance transformation needs to be applied prior solving the model. The relationship between function and structure presents homogeneities that can be exploited to improve the SNR however, it might vary throughout the image therefore the set of coefficients (α_i and b_i) is modelled with a mixture of multivariate normal distributions and estimated through a clustering K-means algorithm. The denoised PET is finally obtained by applying the new set of coefficients to equation 2.40.

Deconvolution and Denoising One way to exploit the capability of wavelet transform to act as denoising tool is to couple them with PVC techniques that suffer from noise amplification to obtain a noise-controlled PVC image. Boussion et al [17] suggested to combine the wavelet-based *BayesShrink* denoising technique [23] with an image deconvolution PVC technique based on the Richardson-Lucy algorithm (see Section 2.3.2). Of course the deconvolution step of the PET image with the scanner PSF is performed prior the denoising one. Despite the improvement in term of noise-controlled the performance of the method still depends on the accurate model of the scanner PSF and the nature of the image noise. Namely, different reconstruction algorithms produce images with different noise characteristics thus appropriate wavelet-based denoising approach has to be

selected.

Synergistic-Functional-Structural RR A similar technique to the Boussion *á trous* algorithm algorithm has been proposed by Shidahara et al [104] specifically for brain data. The technique uses MRI images coupled with anatomical probabilistic brain atlas allowing local analysis and relaxing for structural/functional correlation [10].

To create the structural image to inform the resolution recovery process the authors used a 3D maximum probability atlas defining 83 anatomical structures [46]. Once appropriate registration is performed between atlas and subject spaces, to each segmented region is assigned an intensity value obtained by averaging each region on the original PET.

Initially, both functional and structural images (the regions defined atlas described above) are decomposed trough the Dual Tree Complex Wavelet Transform DT-CWT [60] into several resolution elements. The estimated wavelet coefficients are then collected into two separate matrixes $W_{PET,j}$ (as derived from the original PET image) and $W_{SR,j}$ (as derived from the structural reference image) for each resolution level j. In this implementation we set $j = 1, 2$ meaning that two consecutive wavelet decompositions are attributed to the same original image. The high-resolution coefficients of the functional decomposition are then "replaced" with the coefficients of the structural one by means of combining the two matrices with appropriate local scaling as follows

$$W^{new}_{PET,j} = scaling_1 \cdot W_{SR,j} + scaling_2 \cdot W_{PET,j} \tag{2.41a}$$

$$W^{new}_{PET,j}(q,k) = R_j \cdot \{G_j \cdot \gamma_j(q) \cdot W_{SR,j}(q,k) + [1 - \gamma_j(qright)] \cdot W_{PET,j}(q,k)\} \tag{2.41b}$$

where $q \in Q$ indexes the number of quadrants in the wavelet decomposition and k the position in the wavelet domain within each quadrant. The $W^{new}_{PET,j}$ coefficients are then back-projected into image space using the inverse DT-CWT to obtain the new high-resolution functional image.

In Eq. 2.41b R_j is the recovery coefficient accounting for the difference in resolution between the functional and anatomical images and is defined as

$$R_j = \frac{\sum_k \sum_q W_{SR,j}\{q,k)}{\sum_k \sum_q W_{SR^S,j}\{q,k)} \tag{2.42}$$

where W_{SR^S} is the wavelet transform of the structural reference image smoothed with a 3D Gaussian filter to match the PET scanner resolution (a FWHM of 4mm was selected following a simulation study).

G_j is the anatomical-to-functional global calibration factor and is defined as

$$G_j = \frac{\sum_k \sum_q W_{PET,j}\{q,k)}{\sum_k \sum_q W_{SR,j}\{q,k)} \tag{2.43}$$

The branching ratio γ_j weights the anatomical information by taking into account anatomical variability and statistical variability through measures of wavelet quadrants variance

$$\gamma_j(q) = \frac{SSW_j(q)}{SSW_j(q) + SSB_j} \tag{2.44}$$

Note that in Eq. 2.5 the between quadrant variance SSB depends on anatomical variability while the within quadrant variance SSW is mainly due to stochastic fluctuations and are defined as

$$SSB_j = Q \cdot \sum_k \left(\frac{\sum_q W_{PET,j}}{Q} - \frac{\sum_k \sum_q W_{PET,j}}{Q \cdot K} \right)^2 \tag{2.45}$$

$$SSW_j = \sum_k \left[\sum_{q \in D} \left(W_{PET,j} - \frac{\sum_q W_{PET,j}}{Q} \right)^2 \right] \tag{2.46}$$

When the functional image contains enough structural information the SSB will overtake the SSW reducing the amount of structural input in Eq. 2.41b due to a smaller branching ratio γ_j.

2.6 Conclusion

There is no optimal solution when it comes to the choice of a PVC technique. First of all it is data-dependent; in order to be able to apply methodologies that rely on structural information, anatomical images must be available and perfectly co-registered with the functional ones. Furthermore, some acquisition sites might have available direct measurement of the scanner PSF making a PSF-based PVC approach appealing. Another important consideration concerns the task of the image analysis as well as the target region. When the aim is to perform SUV estimate of selected ROIs, a region-base approach can be suitable, while voxel-based methodologies are preferred when it comes to tissue heterogeneity imaging or performing quantitative measurements at voxel level. Another factor that might influence the PVC choice is the nature of the target area. For example in reconstruction based approaches, the computation burden might become too high when dealing with whole body acquisition, typical of oncological studies, rather than an only-brain one. However, reconstruction based algorithms preserve good image contrast while post-reconstruction techniques lead to better lesion quantification [56], so there is a trade-off between computational load and expected outcome that has to be taken into account.

The aim of this thesis is to select, implement and test PVC approaches that can be easily applied to specific clinical routine images preserving the heterogeneity characteristic of the structures under analysis. For these reasons reconstruction-based approaches have been excluded considering the limitation in extending them to clinical routine where the reconstruction is performed by the scanner software and exporting raw data to implement a different reconstruction approach might be not feasible. Furthermore, patients might be scanned with different scanners during the same study so different models of the system matrix of the scanner PSF might need to be computed.

Region-based approaches have been excluded as well since the assumption of regional homogeneous uptake is not realistic. The author believes that the choice of a PVC technique in this case should come down to wavelet-based techniques. These approaches

are easily and flexibly applicable in image space without the need of prior knowledge about system characteristic and tracer distribution. More specifically, the author finds quite appealing the approach of Shidahara et al since it does allows a local analysis and performs noise-controlled PVC in a single step.

In the following Chapters a slightly modified version of Shidahara method has been applied to whole-body PET/CT data in oncological acquisition. From considerations derived by this first projects, a new wavelet-based approach has been formulated for target brain applications.

However, before approaching directly real clinical data, the author believes that a preliminary step might be useful and interesting for future assessment of algorithm validation. When it comes to validate methodologies based on multimodality imaging a popular choice is to use simulated data. Despite the availability of simulated database of specific clinical images and software for data simulation, obtained suitable simulated data might still be not possible. For these reasons the first investigation presented in this thesis is about performing PET/CT phantom acquisitions showing functional as well as structural image contrast. At the time of the investigation no similar experiments were available in literature as well as no information about tweaking parameters and possible precautions necessary to obtain a phantom acquisition as close as possible to a real patient PET/CT scan.

In the next chapter is described such experimental procedures together with a brief overview of quantitative information that can be obtained from these kind of experiments. The set of images obtained in this phase will be used to validate the wavelet-based PVC approach presented in Chapter 4.

Chapter 3

Exploiting anatomical information for PET image enhancement: A phantom experiment for algorithm validation

Adapted from *Conference Proceedings, IEEE Nuclear Science Symposium and Medical Imaging Conference (NSS/MIC)*, 2014 Seattle

3.1 Introduction

Multimodality imaging acquisition systems (e.g. PET/CT and PET/MR) offer the possibility to integrate both functional and anatomical information to achieve better diagnostic accuracy. The routine in clinical practice is to simply overlap PET images with their anatomical counterpart, either CT or MR. However, novel methodologies are now available for further exploitation of the potential of multimodality imaging by taking advantages of the higher resolution of anatomical images. Recently, attention has been mostly focused on regularizing PET reconstruction by means of integrating MR anatomical information [127, 58, 14] as *prior* information in a *Maximum a Posteriori* (MAP) iterative reconstruction aiming for better noise control and edge sharpening. The high level of anatomical detail in MR images can also be exploited for post-reconstruction PET image de-noising [22] or partial volume correction through image resolution recovery [104, 69]. Despite the majority of

these methodologies being MR-based rather than CT-based, PET/MR systems are still less common than PET/CT.

Furthermore, the majority of algorithms have been validated with simulated data or with clinical brain PET data regardless of the lack of a ground truth. Clinical practice would benefit from the increased image resolution due to the extensions of anatomy-based algorithms from PET/MR to PET/CT systems. However, for a more robust approach, the validation should be performed on realistic phantom acquisitions that would fill the existing gap between data simulation (often simplistic) and real patient data (lacking of a ground truth).

Therefore in this work we describe a reproducible experimental set up aimed to obtain PET/CT images showing a realistic range of correlations (from null to moderate and strong) between anatomical details and corresponding functional uptake. In this specific case, our aim was to mimick the contrast levels of an [^{18}F]Fluoride bone PET/CT scan with the intent of using this acquisition to validate a resolution-recovery algorithm for visualization of bone metastases. However, the procedure can be generalized to a wide range of PET/CT contrast experiments

3.2 Materials and Methods

3.2.1 Phantom preparation

We used the NEMA IEC body phantom without the lung insert with six spheres having volume of 26.52 ml (sphere 1), 11.49 ml (sphere 2), 5.57 ml (sphere 3), 2.57 ml (sphere 4), 1.15 ml (sphere 5) and 0.52 ml (sphere 6) respectively. All the phantom compartments (the main chamber and the six spheres) were filled with iodinated CT contrast media (CM) Omnipaque300^{TM} (300mg/ml organic Iodine) and radioactive tracer [^{18}F]Fluoride at varying concentrations. We aimed to reproduce PET and CT contrast levels between spheres and background as observed in clinical [^{18}F]Fluoride bone scans. Specifically, we aimed to reproduce the contrast levels that are reported in Table 3.1 as they were observed in a patient scan for soft tissue, bone tissue and sclerotic bone metastases.

The phantom background was associated with the soft tissue while the spheres were considered as bone tissue or bone lesion. The values reported were obtained as the ratio of mean values computed in different ROIs that were manually outlined in a representative patient PET/CT scan.

	PET contrast	CT contrast
Bone/Tissue	12	5
Lesion/Tissue	35	25

Table 3.1: PET/CT contrast levels in a standard bone [^{18}F]Fluoride bone scan

The desired radiotracer concentration is made knowing the volume of each sphere and considering that the injected radioactivity is kept confined.

To the best of our knowledge, we found only one study reporting the trend of CT contrast variation in terms of Hounsfield Units against the CM concentration variation, showing a linear relationship between HU and iodine concentration up to 20 M solution for a range of tube potentials (40kVp-90kVp)[93]. Therefore, in order to characterize the CM concentration necessary for our scope (a standard CT scan uses 140 kVp), we performed a calibration CT acquisition. This calibration step consisted in filling with 0.2 ml of CM each sphere that was then topped up with water; the resulting Iodine concentrations in each sphere were therefore 2.3, 5.2, 10.7, 23, 54 and 120 mg/ml. Through the analysis of the CT images we derived the relationship between Iodine concentration and resulting CT image contrast and therefore selected the appropriate Iodine concentration for our purpose.

The CT acquisition has a dual purpose, not only providing anatomical information but also returning the attenuation correction factors used during PET reconstruction. In order to avoid activity estimation bias [83] as a result of using the incorrect attenuation map (μ-*map*) due to the iodinated contrast media, it is necessary to perform an additional scan where all phantom compartments are filled with only water. The resulting μ-*map* from this scan was used to attenuation correct all further PET scans from the contrast experiments. The CT scan of the water phantom was registered with the contrast media CT acquisition of each PET/CT experiment via a semi-automated rigid registration on a GE

AW Workstation (v4.6). We scanned the calibration phantom two times after applying a slight rotation and translation and then using the different detectable structures to validate the registration procedure.

Images were acquired on a GE Discovery 710 PET/CT scanner. CT scans were performed using our clinical protocol for routine patient imaging with 115 mA, 140 kVp and gantry rotation speed of 0.5 second followed by fully 3D PET-TOF acquisitions of 5 minutes.

Sections	Experiment 1		Experiment 2	Experiment 3
	Iodie	[^{18}F]FDG	Iodine [^{18}F]FDG	Iodine [^{18}F]FDG
Background	Tissue		Tissue	Tissue
Sphere 1	Bone		Bone	Tissue
Sphere 2	Bone		Lesion	Lesion
Sphere 3	Bone		Bone	Tissue
Sphere 4	Tissue	Lesion	Lesion	Lesion
Sphere 5	Tissue	Lesion	Bone	Tissue
Sphere 6	Tissue	Lesion	Lesion	Lesion

Table 3.2: Classification of the phantom compartments

We performed three different acquisitions in order to simulate different scenarios, including (Experiment 1) a possible mismatch between anatomical and functional image (i.e. a structure classified as a lesion on the PET but not on the CT). The rationale behind this is testing robustness of the anatomical based technique towards lack of available information. Table 3.2 reports the scenarios we aimed to simulate in each experiment.

3.2.2 Image Processing

In order to explore the range of possibilities of using anatomical information to enhance the functional information, we integrated the former both within- and post- reconstruction. PET data were reconstructed with the same settings used in clinical routine but also using a *Maximum a Posteriori* (MAP)-OSL reconstruction regularized with a Bowsher-type [14] anatomical prior. For inclusion of the anatomical information in the post-reconstruction approach, the images reconstructed with standard settings were processed with a modified version of the Synergistic-Functional-Structural Resolution Recovery (SFS-RR) tech-

nique [104].

The standard PET reconstruction was an iterative TOF-OSEM algorithm, with 24 subsets and 2 iterations performed with the scanner manufacturer software (GE Q.Core Vue-Point). The MAP reconstruction was implemented with the Software for Tomographic Image Reconstruction (STIR) [115]. Subsets and iteration numbers were the same as the standard reconstruction to have a more meaningful comparison; higher number of iterations can produce a more accurate signal recovery but also increase the noise level. For a more exhaustive final picture we performed the standard reconstruction using the attenuation correction factors derived from CT images with CM to quantify the impact of using the wrong μ-*map*.

Signal-to-noise ratio was also calculated for a quantitative comparison of trade-off between noise and image signal obtained with different modalities. Where $Activity_{xxx}$ is the average measure activity of the specified area and σ_{BG} the standard deviation of the phantom background.

$$SNR = \frac{Activity_{ROI} - Activity_{BG}}{\sigma_{BG}} \tag{3.1}$$

3.3 Results

Figure 3.1 shows a CT transaxial view of the phantom used in the calibration step to determine the relationship between Iodine concentration and image contrast in terms of Hounsfield Units. Each sphere contains 0.2 ml CM but being of different volumes the resulting CT contrast is inversely proportional to the sphere volume. We performed two scans of the phantom in two different positions (Figure 3.1a - 3.1b) to validate the registration procedure used to register the water-only phantom CT into the space of the CM phantom CT.

Figure 3.2 displays the mean values in Hounsfield Units of different ROIs drawn on the CT images plotted against the corresponding Iodine concentration from the CM. A suggested sigmoidal curve represented the optimal fit for our measurements. As the final aim of the experiment was mimicking a bone PET/CT, we were interested in the Iodine concentrations providing CT contrast similar to bone structures. Therefore the choices of

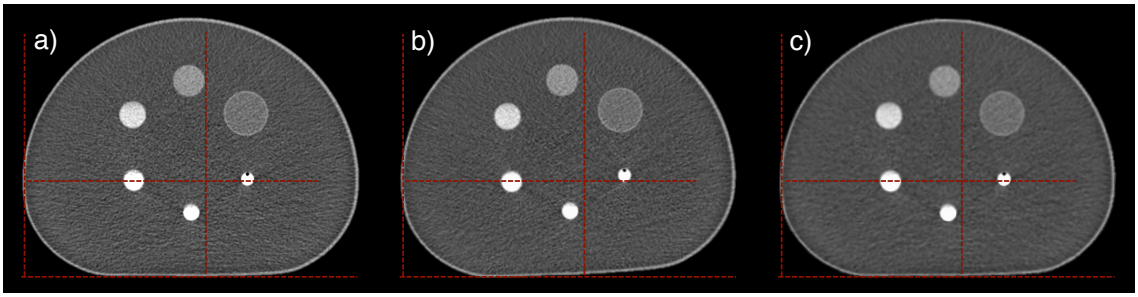

Figure 3.1: CT transaxial view of the calibration phantom. Each sphere is filled with 0.2 ml CM. a) reference acquisition; b) same phantom as in a) slightly rotated and shifted with the purpose of testing the registration procedure; c) registered version of b) into the native space of a). Dashed red lines help with misalignment visualization

CM concentration were based on the data derived from the grey shaded area in Figure 3.2. Note that the intensity range we are interested in refers to the linear part of the graph.

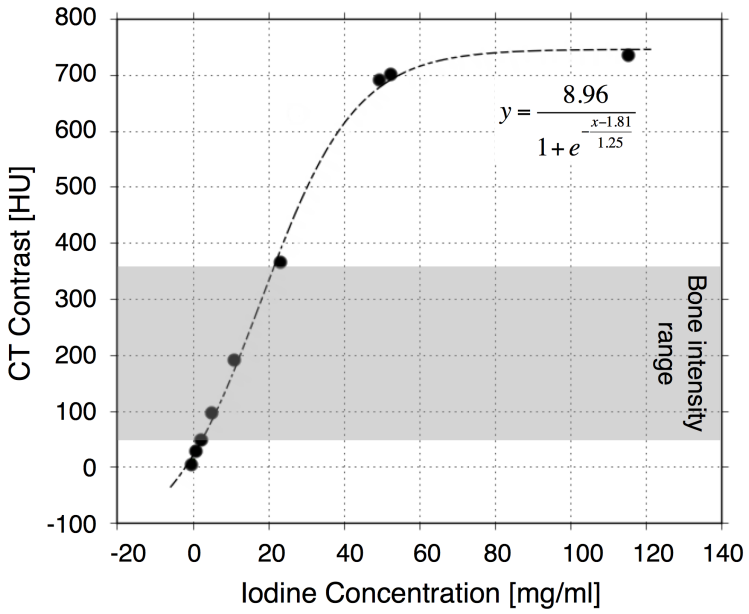

Figure 3.2: Plot showing the correlation between organic Iodine concentration (CM 300mg I/ml) and the average CT values in HU measured on the images. Black dots are the measurements while dashed line is the sigmoid interpolation. Grey area is indicative of the range of CT Hounsfield Unit in bone tissue

We performed three different acquisitions in order to simulate different scenarios as already described in Table 3.2. Hence Table 3.3 reports the concentrations of CM and radiotracer employed to reproduce those scenarios, where Sphere 1 represent the sphere

Sections	Experiment 1		Experiment 2		Experiment 3	
	Iodie	[^{18}F]FDG	Iodine	[^{18}F]FDG	Iodine	[^{18}F]FDG
Background	1.09	4.56	1.20	5.29	1.20	5.70
Sphere 1	6.00	53.20	6.00	66.50	1.20	5.90
Sphere 2	6.00	53.20	42.00	187.00	41.20	227.00
Sphere 3	6.00	53.20	6.00	66.50	1.20	5.90
Sphere 4	1.00	148.50	42.00	187.00	41.20	227.00
Sphere 5	1.00	148.50	6.00	66.50	1.20	5.90
Sphere 6	1.00	148.50	42.00	187.00	41.20	227.00

Table 3.3: Contrast media and radiotracer concentrations in phantom compartments. Sphere volume decrease from bigger to smaller from Sphere 1 to Sphere 6.

with bigger volume and sphere 6 the sphere of smaller volume.

Figure 3.3 shows transaxial views of PET/CT acquisition (standard PET reconstruction, attenuation map derived from the water-only phantom) for the three phantom experiments described in Tables 3.2-3.3. All images are smoothed with a 3D Gaussian filter with FWHM of 6.4mm.

Figure 3.4 shows different image combinations that can be explored with a PET/CT contrast acquisition. We show the transaxial views for the sole Experiment 2. Figure 3.4a shows an image reconstructed with the standard OSEM approach as reference. Figure 3.4b is still reconstructed with standard OSEM but using the incorrect attenuation map derived from the CT scans with iodinated CM. Figure 3.4c-3.4d shows what can be achieved when the anatomical information can be incorporated to enhance image quality. Specifically, in 3.4c we applied an anatomy-based resolution recovery algorithm after standard reconstruction generating an improved recovery of smaller structures. The image in 3.4d was reconstructed using a MAP approach with anatomical prior that resulted in a better noise control ($SNR_{standardOSEM}$ = 5.5, SNR_{MAP} = 13).

In Figure 3.5 we reported some quantitative analysis that can be derived from Figure 3.4. The three smaller spheres were automatically segmented on the PET images using a threshold of 30% *SUVmax* as routinely performed with [^{18}F]Fluoride bone scans. The performance of each methodology can be evaluated in terms of volume segmentation and activity quantification being the ground truth known. Figure 3.5a shows that a more accurate volume definition can be achieved when the anatomical information is

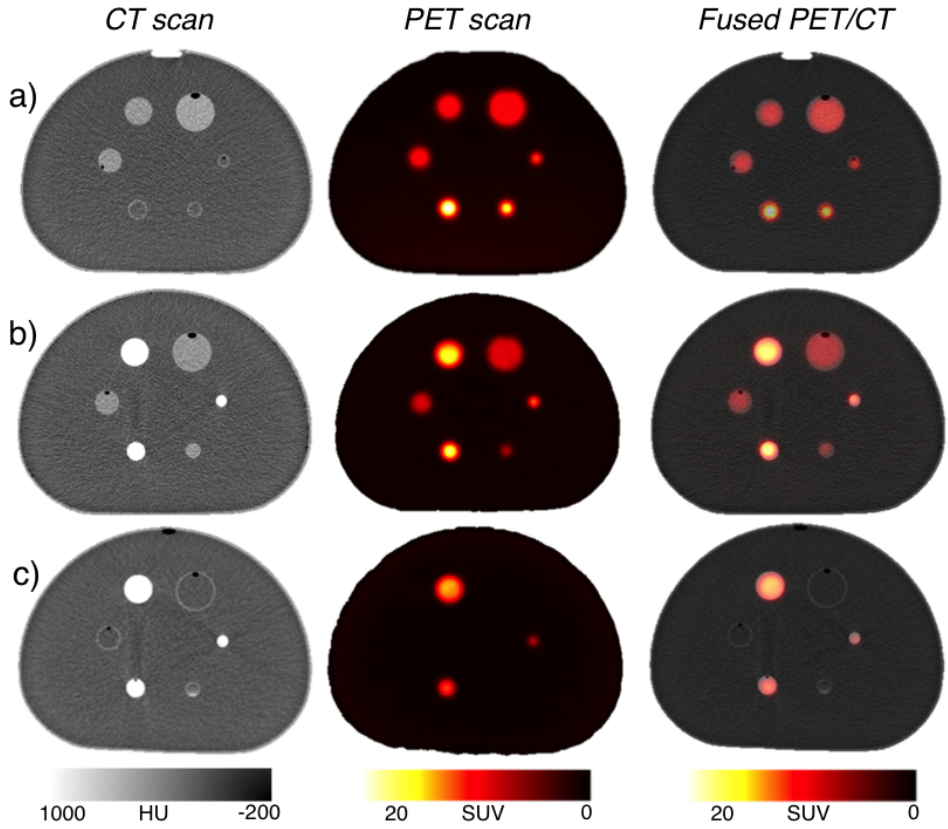

Figure 3.3: Phantom transaxial views of CT (left), PET (center) and fused PET/CT (right). PET images are reconstructed with standard OSEM. Each line refers to a different experiment: a) Experiment 1; b) Experiment 2; c) Experiment 3. Experiments settings are reported in Tables 3.2-3.3.

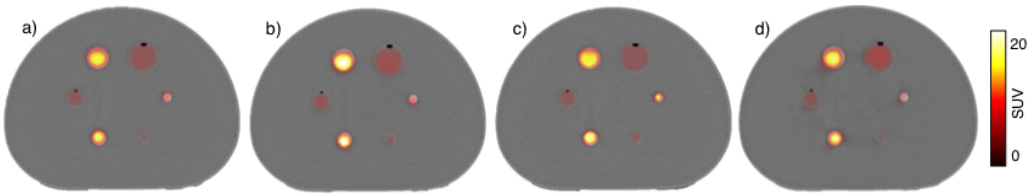

Figure 3.4: PET/CT fused transaxial view of Experiment 2. a) Standard OSEM reconstruction; b) OSEM reconstruction using the incorrect attenuation map derived from CT image with CM; c) Standard OSEM reconstruction with application of an Anatomy-Based Resolution-Recovery technique; d) MAP reconstruction with anatomical prior

taken into account, both within- and post- reconstruction (average volume overestimation $PET_{STANDARD}$ = 80%, $PET_{RES-RECOVERY}$ = 36%, $PET_{ANATOMICAL-PRIOR}$ = 67%). The same applies for activity quantification, which resulted in a smaller bias especially when a post reconstruction resolution recovery algorithm was employed ($PET_{STANDARD}$ = 66%, $PET_{RES-RECOVERY}$ = 54%, $PET_{ANATOMICAL-PRIOR}$ = 57%). When anatomical information are taken into account the post-reconstruction approach shows better performance; in the specific case is due to the better image contrast that the one of images reconstructed with the Bowsher prior that are here characterized by increase image smoothing. Other type of prior could be tested together with different penalty factor to investigate the best combination for the specific acquisition, but this goes beyond the goal of this experiment. In the plot reported in Figure 3.5c it is shown that the difference in the recovered PET activity concentration due to an incorrect attenuation correction falls in a range between 10-20% and increases linearly with CT contrast differences.

3.4 Conclusions

This report provides a detailed description of PET/CT phantom acquisitions aimed to obtain functional and anatomical images with a range of correlated structures. This represents a useful methodology to produce test sets for the validation of algorithms that enhance PET image quality through the integration of anatomical information into the standard PET. Quantitative measurements and observations on the influence of contrast media on both CT and PET have been reported. To the best of our knowledge these are the first experiments investigating the effect of bone attenuation in quantifiable PET/CT scanning The results reported in this work provide sufficient information to reproduce the experiments for desired contrast level and represents a good starting point to perform a wider range of acquisitions and analyses.

In the context of this thesis, the phantom images produced in this empirical part, have been used to validated a PVC technique adapted for whole-body oncological PET/CT scans. The following Chapter will describe the clinical motivation and background for PVC while these phantom experiments will be used in the Material and Method Section

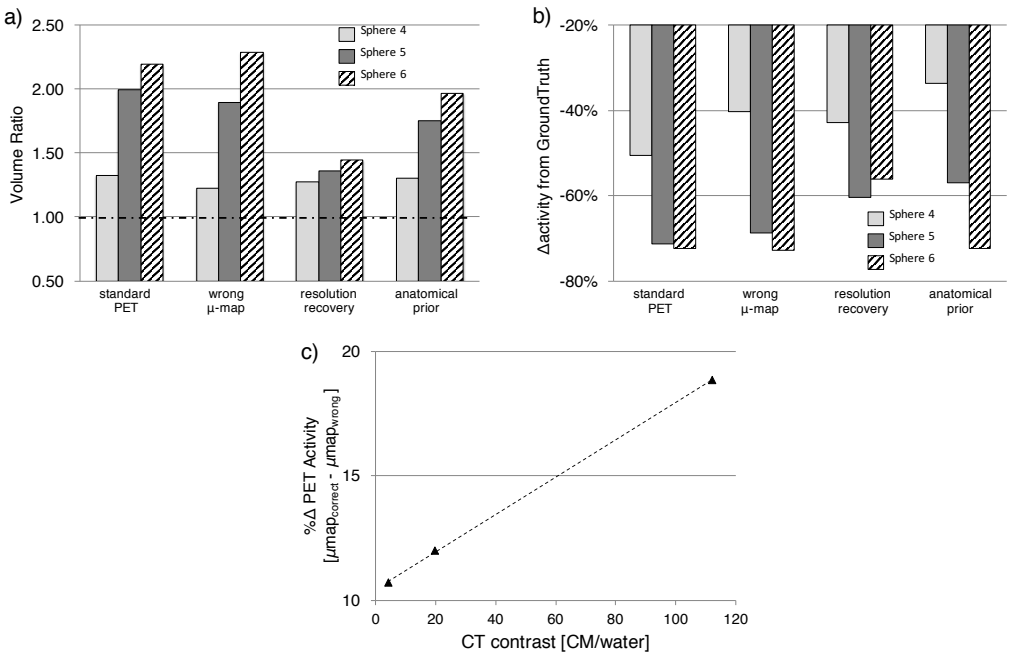

Figure 3.5: Representative quantitative analyses showing what it is possible to investigate with the described PET/CT contrast acquisition. a) Ratio between the real volume and the volume computed after automated threshold segmentation. b) Percentage difference of the recovered PET radioactivity against the ground truth. c) Percentage difference of the recovered PET radioactivity when reconstruction is performed using the incorrect attenuation map. Results are reported for the three smallest spheres in a) and b) and for the average of spheres representing background, bone and lesion contrast in c).

as a tool to validate the PVC approach before its application on clinical data.

Chapter 4

Multimodal PET/CT PVC - Application to [^{18}F]Fluoride bone metastases studies

Adapted from *Journal of Nuclear Medicine* 2015; 56:1408-1414
DOI: 10.2967/jnumed.115.160598

4.1 Introduction

Up to 70% of patients with prostate and breast cancer will develop bone metastases [98, 27]. [^{18}F]Fluoride has shown efficacy in both diagnosis and treatment response assessment [25, 113, 101, 26] and recent studies on skeletal metastases report improved diagnostic sensitivity and specificity when morphologic evaluation from computed tomography (CT) scans are combined with functional evaluation of [^{18}F]Fluoride positron emission tomography (PET) [35, 36]. This radiotracer accumulates at skeletal metastatic sites as a result of increased blood flow, osteoblastic activity and bone mineralization [42, 88, 129]. In prostate cancer, [^{18}F]Fluoride accumulation corresponds to sites of osteosclerosis and increased bone density that are usually visible on CT [8].

Evaluation criteria for tumor staging and response assessment include visual and/or quantitative evaluation of the extent, intensity and changes in [^{18}F]Fluoride uptake in bone lesions [132]. In this perspective the influence of the partial volume effect (PVE) is of impact [109] when comparing activity and morphological changes pre- and post-

therapy [47, 107] considering the poor image resolution and quantification bias resulting from activity spill-over. PVE in PET has been addressed with several imaged-based partial volume correction (PVC) methods [96] that can be classified as either voxel-based methods, such as partition-based [77], multiresolution [16, 104], or region of interest (ROI)-based techniques [5, 97], which are limited by assumptions of radiotracer distribution homogeneity in the area of interest. A distinct approach consists of the incorporation of a model for the system point-spread-function (PSF) within the image reconstruction algorithm to account for resolution degradation [89, 92].

In this study our aim was to correct for the PVE in whole-body [^{18}F]Fluoride PET-CT to allow a more robust lesion classification in terms of activity quantification and volume definition. The methodology was developed from previous work by Shidahara et al [104] and exploits the local functional/structural relationship of PET/CT in a synergistic fashion for a realistic noise controlled resolution recovery of PET images, hence the name Synergistic-Functional-Structural Resolution-Recovery (SFS-RR). Here the SFS-RR algorithm is optimized for [^{18}F]Fluoride PET given the correlation between functional (fluoride uptake) and morphological (sclerosis) signals on PET and CT images. For benchmarking the resulting images were compared to standard reconstructed PET images and images reconstructed with the inclusion of the PSF model [3].

4.2 Materials and Methods

4.2.1 Image Resolution Recovery

The Synergistic-Functional-Structural Resolution-Recovery (SFS-RR) algorithm was first introduced by Shidahara et al. [104] for partial volume correction of brain PET-MR data. The idea stems from previous concepts on wavelet-based resolution recovery [16] and de-noising [119]. The structural information was exploited by segmenting a T1-MRI image through a probability atlas [46] defining 83 anatomical regions. Hence, the resolution recovery is ROI-based and relies on good co-registration between PET and MRI images as well as between MRI and the probability atlas.

In this work we developed SFS-RR further to fit a novel clinical requirement, specifically [^{18}F]Fluoride PET/CT for detecting and monitoring bone metastases. The choice of the application is not fortuitous; in the first instance, PET/CT images provide synergistic information (i.e. both modalities show high image intensity in correspondence of lesions) and, secondly, they do not require additional coregistration as for two separate PET and MR acquisitions. Furthermore all the structural information of interest is contained in the CT and can be automatically segmented for each subject with no need for a universal atlas. The algorithm decomposes both functional (PET) and anatomical (CT) images into several resolution elements by means of a wavelet transform. The high-resolution components of both modalities are then combined together via a statistical model with appropriate scaling, resolution correction and weighting, to create a high-resolution PET image that exploits the structural information, when present, but preserves PET data when matching structural data are not present. The whole procedure is schematically described in Figure 4.1 while the original algorithm has been previously described in section 2.5.

In contrast to the original work of Shidahara et al [104] when referring to the final relation between structural and functional wavelet coefficients (equations 2.41) the branching ratio γ_j is calculated in a slightly different way. From equation 2.46 one can see that within quadrant variance is computed as the sum of deviations over diagonal quadrants (D). Here however, the within quadrant variance is computed taking into consideration each quadrant in wavelet domain separately instead of averaging over the diagonal ones only as in equation 4.1.

The rationale behind this choice depends on the nature of PET image noise that, being non-white and correlated, projects differently into each wavelet quadrant [120]. Therefore accurate estimation of the variance of the wavelet coefficients requires independent computation in each quadrant.

$$SSW_j\left(q\right) = \sum_k \left(W_{PET,j} - \frac{\sum_q W_{PET,j}}{Q} \right)^2 \tag{4.1}$$

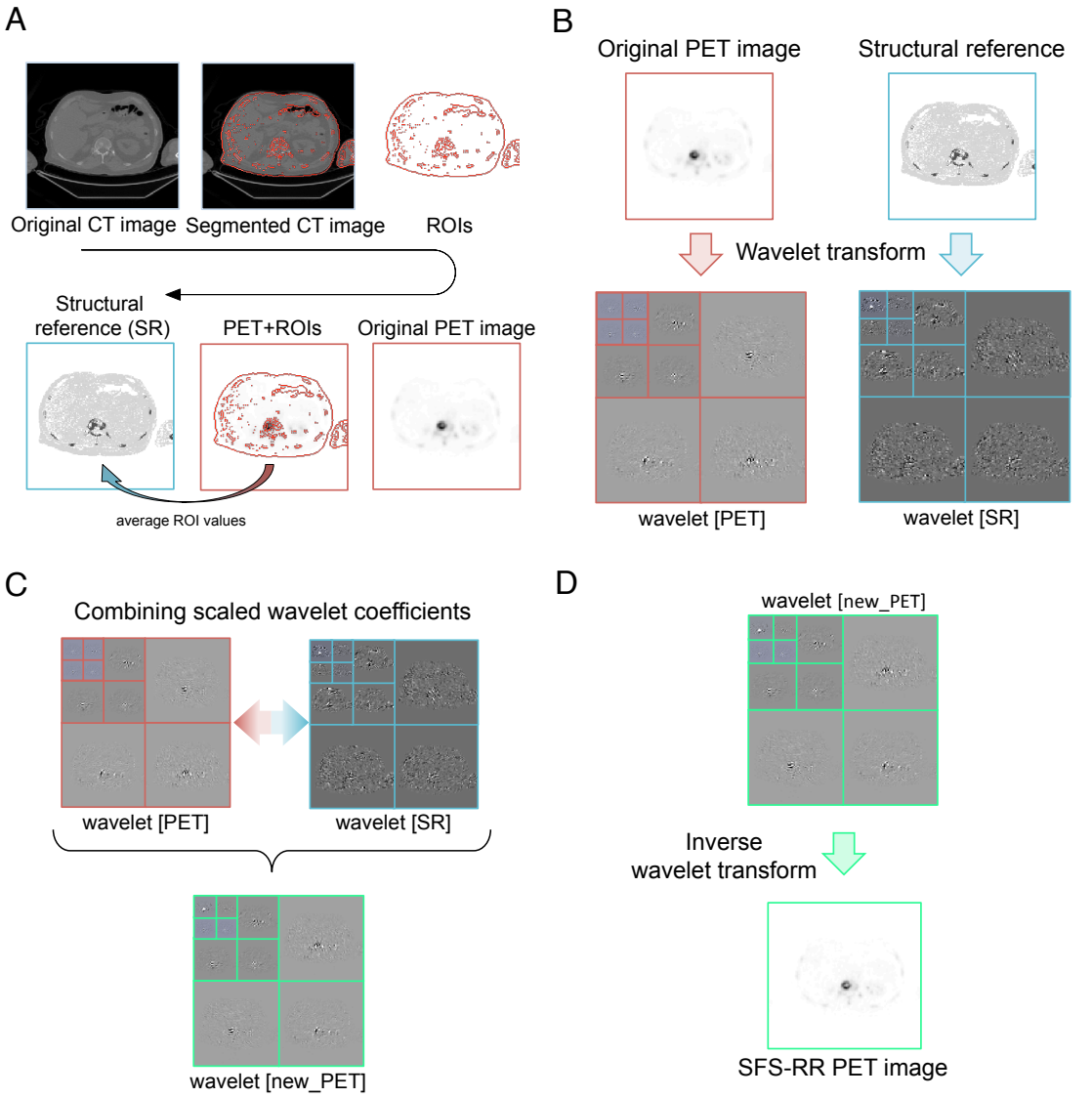

Figure 4.1: Graphical representation of the SFS-RR algorithm. A) The structural reference image required by the SFS-RR algorithm is computed from the CT and PET images; B) wavelet decomposition of functional and structural images; C) the functional and structural wavelet coefficients are combined to get the new high-resolution PET coefficients; D) inverse wavelet transform of the coefficients obtained from step C resulting in the new high-resolution SFS-RR PET image. For a detailed mathematical formulation please refer to the Supplementary Materials B.

4.2.2 Anatomical Image Segmentation

In their original work, Shidahara et al. [104] proposed the use of an anatomical brain atlas to obtain suitable anatomical images. In brain studies this is a reasonable procedure given the possibility of normalizing to a common space (e.g. probabilistic atlas).
In whole-body PET-CT, the atlas-based approach is not feasible. In [^{18}F]Fluoride PET-CT acquisitions the good spatial correlation between morphological and functional information is such that the CT images of each subject can be processed individually to highlight the structures of interest supplying the required structural base.
The first step consists of an initial coarse segmentation of the CT images based on thresholding the Hounsfield Units (HU) values as follow: bone (100$\leq$HU$\leq$1400), soft tissue (0$\leq$HU$\leq$100) and fat (-150$\leq$HU$\leq$0) [78]. Bone is further segmented into 100 bins after image histogram equalization. New intensity values are assigned to all the segmented regions. These intensity values are calculated from the average of each corresponding region in the original PET image to obtain the subject-specific structural reference image used as anatomical information for the SFS-RR algorithm [104, 66]. For an example of segmentation achieved in the spinal chord see Figure 4.2.
Image segmentation and the SFS-RR algorithm implementation were both performed in Matlab R2011b (The Mathworks Inc., Natick MA, USA).

4.2.3 Phantom Data

For the evaluation of the SFS-RR method we used the NEMA IEC body phantom and an insert with six spheres of different volumes, 26.52 cm^3 (S1), 11.49 cm^3 (S2), 5.57 cm^3 (S3), 2.57 cm^3 (S4), 1.15 cm^3 (S5) and 0.52 cm^3 (S6), respectively. Compartments were filled with both iodinated contrast media (CM) Omnipaque300^{TM} (300 mg/ml organic Iodine) and radioactive tracer 18F-Fluoride. We aimed to reproduce contrast levels between different structures in both the PET and CT images as observed in clinical [^{18}F]Fluoride bone scans. Specifically, we reproduced PET and CT contrasts as observed in normal soft tissue, normal bone and metastatic bone. We performed three different experiments changing the layout of CT and PET contrasts. This aimed to account for possible mis-

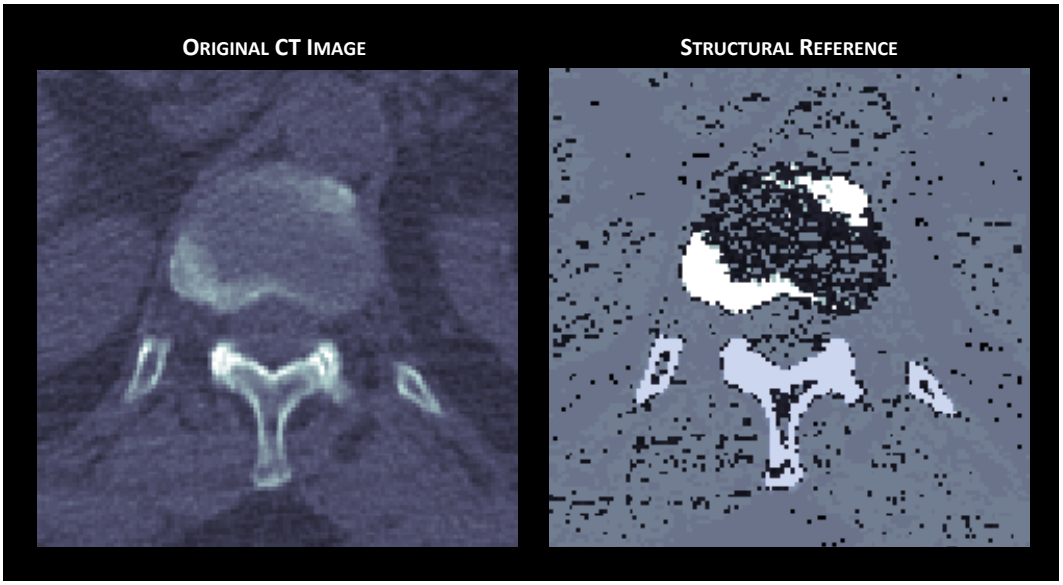

Figure 4.2: Comparison between the original CT image (left) and the structural reference image (right) for a zoomed transaxial spinal view. The ROIs of the structural reference are defined by automatic thresholding the original CT intensities in Hounsfield Units; the new value for each ROI is defined as the average activity of each corresponding region in the original PET image.

matches between functional and anatomical images (i.e. whereas a lesion would be detectable in only one imaging modality) resulting in a more robust method validation for what concern the phantom experiments. A summary of CM and radiotracer concentrations used in each experiment is reported in Table 4.2.3. For a detailed description of the experimental procedure we refer to Chapter **??**.

Phantom Compartments	Experiment 1		Experiment 2		Experiment 3		Sphere Volume ml
	Iodie CM [mg/ml]	[^{18}F]FDG [kBq/ml]	Iodie CM [mg/ml]	[^{18}F]FDG [kBq/ml]	Iodie CM [mg/ml]	[^{18}F]FDG [kBq/ml]	
Background	1.09	4.56	1.20	5.29	1.20	5.70	9700
Sphere 1	6.00	53.20	6.00	66.50	1.20	5.90	26.52
Sphere 2	6.00	53.20	42.00	187.00	41.20	227.00	11.49
Sphere 3	6.00	53.20	6.00	66.50	1.20	5.90	5.57
Sphere 4	1.00	148.50	42.00	187.00	41.20	227.00	2.57
Sphere 5	1.00	148.50	6.00	66.50	1.20	5.90	1.15
Sphere 6	1.00	148.50	42.00	187.00	41.20	227.00	0.52

Table 4.1: Contrast media and radiotracer concentrations in phantom compartments

Images were acquired on a GE Discovery 710 PET-CT scanner (General Electric Medical System, Milwaukee, WI, USA). CT scans were performed with a routine clinical protocol

(115 mA, 140 kVp and 0.5 second gantry rotation speed) followed by a fully 3D PET Time Of Flight (TOF) acquisition. PET data were reconstructed using our routine clinical protocol, a standard TOF Ordered Subsets Expectation Maximization (OSEM) algorithm (24 subsets, 2 iterations) (GE Q.Core VuePoint FX, henceforth called *Standard PET*). The resulting images were then processed with the SFS-RR algorithm. In addition we reconstructed the same data with the inclusion of a Point Spread Function (PSF) model into the standard TOF-OSEM algorithm (GE Q.Core VuePoint FX-S, henceforth called *PET-PSF*).

All the images were finally smoothed with a Gaussian 3D filter FWHM 6.4mm; this is required by PSF reconstructed images as well when used in clinical routine given that increased noise level hamper visual assessment

4.2.4 Clinical Dataset

The impact of the proposed resolution recovery technique was tested with two different sets of oncological patient data, both characterized by the presence of bone metastases. The institutional review board approved this study and all subjects signed a written informed consent

The first dataset was a prospective observational study of patients with bone-predominant metastatic prostate cancer, at first diagnosis or at progression of disease, who were embarking on docetaxel chemotherapy. The second data set was a prospective observational study of patients with bone-predominant metastatic breast cancer, at first diagnosis or at progression of disease, who were embarking on a new line of endocrine treatment in combination with bone-targeted therapy. In total 7 patients with active skeletal metastases were included in the analysis, 4 with prostate cancer and 3 with breast cancer.

In each patient a whole body [^{18}F]Fluoride PET-CT scan was acquired with a total of 8 bed positions, from the base of the skull to upper thighs, 60 minutes after injection of approximately 250MBq.

The image reconstruction protocol for both datasets was the same as for the phantom experiment, with the exclusion of the PSF reconstruction, which was not performed as it

was not included in the clinical protocol.

4.2.5 Data Analysis

In-house software was used to perform quantitative analysis on both phantom and patient data. An ROI was manually drawn on the outer border of each lesion in order to completely contain the whole lesion volume (or sphere for the phantom data) and then automatically segmented with a threshold of 40$\%$ of the maximum value of the ROI. The SUV$_{mean}$, SUV$_{max}$, SUV$_{peak}$ and lesion metabolic active tumor volume (MATV) were then computed for the automatically segmented ROI. SUV$_{peak}$ is computed here as the mean SUV measured over a fixed small circular volume of about 1cm^3, in the hottest area of the tumor (more active region). It is considered more reproducible since it involves the mean value of a few voxels involving and surrounding the hottest tumor area.
Solely for the phantom experiments, knowing the ground truth, we used the Root Mean Square Error (RMSE) and Contrast to Noise Ratio (CNR) as additional metrics for image quality assessment. Specifically, we evaluated the quantification accuracy and the trade-off between contrast improvement and image noise. The two metrics are defined as follows

$$RMSE = 100 \times \sqrt{\frac{(A_S - A_{S,true})^2}{{A_{s,true}}^2}} \tag{4.2}$$

$$CNR = \frac{A_S - A_{S,back}}{\sigma_{back}} \tag{4.3}$$

A$_S$ represents the mean activity estimated inside a sphere and A$_{S,true}$ the corresponding ground truth while A$_{back}$ is the mean activity estimated in the phantom background and σ_{back} its standard deviation.

4.3 Results

4.3.1 Phantom Data

Figure 4.3 shows representative transaxial views of structural (CT) and functional (PET) images for the three phantom experiments, one for each line. PET images from PSF reconstruction (PET-PSF) and from the application of the Resolution Recovery algorithm (PET-SFS) are also displayed. In Figure 4.4 are reported as well representative line profiles for the three experiments for spheres 4-5. Improved qualitative resolution for the smaller structures (red marker in Figure 4.3) is noted when the SFS-RR algorithm is applied. Even though larger spheres (green and blue markers in Figure 2) are easily detectable in the images from all modalities, it is possible to appreciate a reduction in the blurring surrounding the structure when the resolution recovery algorithm is implemented. Furthermore it is possible to appreciate the robustness of the anatomy-based resolution recovery algorithm to unexpected mismatches between anatomy and functional acquisition by studying images from Experiment 1. Even though spheres 4-6 cannot be detected on the CT they are not lost in the new functional image returned by the SFS-RR algorithm. The quantitative evaluation of functional images obtained with the three different methods is reported in Tables 4.2. The tables report for each phantom compartment in all the experiments the estimates of SUV$_{mean}$, SUV$_{max}$, SUV$_{peak}$ and MATV together with the corresponding ground-truth values

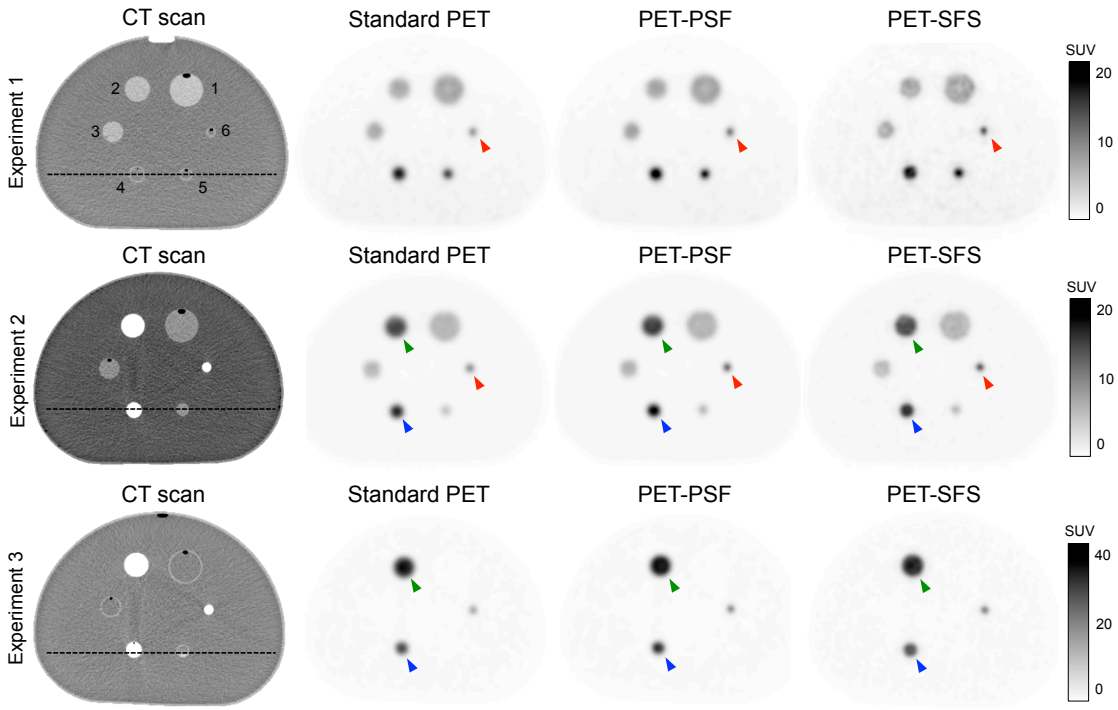

Figure 4.3: [^{18}F]Fluoride PET-CT transaxial images of three different phantom experiment acquisitions (one for each line). Alongside the CT image (1st column) are three different types of functional images: standard PET images (2nd column), images resulting from the inclusion of a PSF model into the reconstruction (3rd column) and images resulting after the application of the SFS resolution recovery algorithm (4th column). For detailed information on lesions volume, CM and 18F-FDG concentrations we refer to Table 4.2.3. Green markers highlight sphere 2, blue markers highlight sphere 4 and red markers highlight sphere 6.

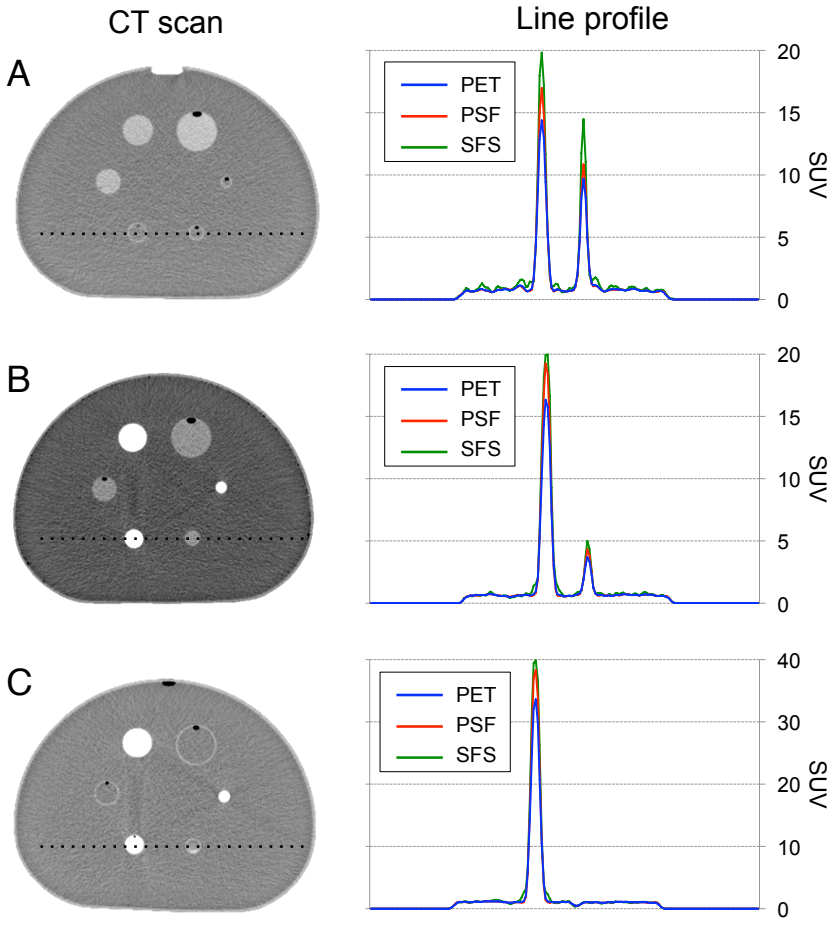

Figure 4.4: CT images and line profiles of three different phantom experiment acquisitions (one for each line). The line profiles in the 2nd column refer to the position highlighted by the dashed line on the CT. The line profiles are reported for all the three imaging modalities under examination: standard PET (blue line), PET-PSF (red line) and PET-SFS (green line).

Table 4.2: SUV_{mean}, SUV_{max}, SUV_{peak} and MATV estimates computed for the phantom spheres after automated segmentation for all the Experiments 1-3. Values are reported for estimates obtained with three different modalities (standard PET, PET reconstructed with a PSF model, PET corrected with the SFSRR algorithm) alongside the corresponding ground truth values

Experiment 1														
	$SUV_{mean}[g \setminus ml]]$			$SUV_{max}[g \setminus ml]]$			$SUV_{peak}[g \setminus ml]]$			Ground	$MATV cm^3$			Ground
	PET	PET_{PSF}	PET_{SFS}	PET	PET_{PSF}	PET_{SFS}	PET	PET_{PSF}	PET_{SFS}	Truth	PET	PET_{PSF}	PET_{SFS}	Truth
S1	5.66	5.95	6.44	8.45	8.84	10.03	8.03	8.17	8.19	9.60	32.22	30.81	30.44	26.52
S2	5.29	5.64	6.28	8.50	9.00	10.69	8.50	8.8	7.88	9.60	13.84	13.20	12.47	11.49
S3	4.54	5.01	5.73	7.73	8.58	9.37	7.73	7.87	7.97	9.60	7.46	6.72	6.75	5.57
S4	10.22	12.25	13.17	18.64	22.12	22.11	18.64	16.25	18.24	24.87	3.52	2.86	3.33	2.57
S5	7.72	9.51	12.60	14.82	18.55	23.56	14.81	10.91	13.75	24.87	1.98	1.56	1.37	1.15
S6	4.21	5.27	8.50	8.19	10.52	16.92	4.77	10.51	11.96	24.87	1.34	1.10 0.83	0.52	

Experiment 2														
	$SUV_{mean}[g \setminus ml]]$			$SUV_{max}[g \setminus ml]]$			$SUV_{peak}[g \setminus ml]]$			Ground	$MATV cm^3$			Ground
	PET	PET_{PSF}	PET_{SFS}	PET	PET_{PSF}	PET_{SFS}	PET	PET_{PSF}	PET_{SFS}	Truth	PET	PET_{PSF}	PET_{SFS}	Truth
S1	4.65	4.87	5.16	6.85	7.08	7.78	6.62	6.69	6.54	8.67	34.28	32.96	31.03	26.52
S2	10.40	11.11	11.55	16.28	16.83	17.16	15.63	15.87	14.92	24.38	14.06	13.54	13.52	11.49
S3	3.87	4.25	4.60	6.74	7.25	7.57	6.09	6.61	6.39	8.67	7.53	6.89	6.53	5.57
S4	9.93	11.42	12.40	17.57	20.21	19.76	13.95	15.90	17.20	24.38	3.35	3.03	3.20	2.57
S5	2.49	3.08	4.02	4.97	6.05	7.71	3.14	3.57	4.76	8.67	2.32	1.71	1.37	1.15
S6	4.56	6.16	8.57	8.79	11.76	16.14	5.02	7.60	10.03	24.38	1.39	0.98	0.86	0.52

Experiment 3														
	$SUV_{mean}[g \setminus ml]]$			$SUV_{max}[g \setminus ml]]$			$SUV_{peak}[g \setminus ml]]$			Ground	$MATV cm^3$			Ground
	PET	PET_{PSF}	PET_{SFS}	PET	PET_{PSF}	PET_{SFS}	PET	PET_{PSF}	PET_{SFS}	Truth	PET	PET_{PSF}	PET_{SFS}	Truth
S2	24.59	25.95	26.63	38.11	38.01	37.90	37.20	36.82	34.87	40.61	13.52	13.42	13.59	11.49
S4	16.68	19.08	20.74	29.92	34.12	33.97	23.78	26.89	29.19	40.61	3.35	3.08	3.25	2.57
S6	7.36	9.78	13.61	13.77	18.33	25.52	8.02	14.08	19.15	40.61	1.25	0.90	0.79	0.52

A summary of the performance of the methods is summarized in Figure 4.5 as the average among the three experiments. The general trend shows that the smaller the sphere, the bigger the bias in the activity estimation, regardless of the method used. However, with the SFS-RR application the bias decreases with an average range of 1-5% in the PET-PSF images and 5-19% in PET-SFS images. The same trend applies to lesion size estimation where the bias decreases in a range of 0.46-0.95 cm for PET-PSF data and 0.56-1.09 cm for PET-SFS data.

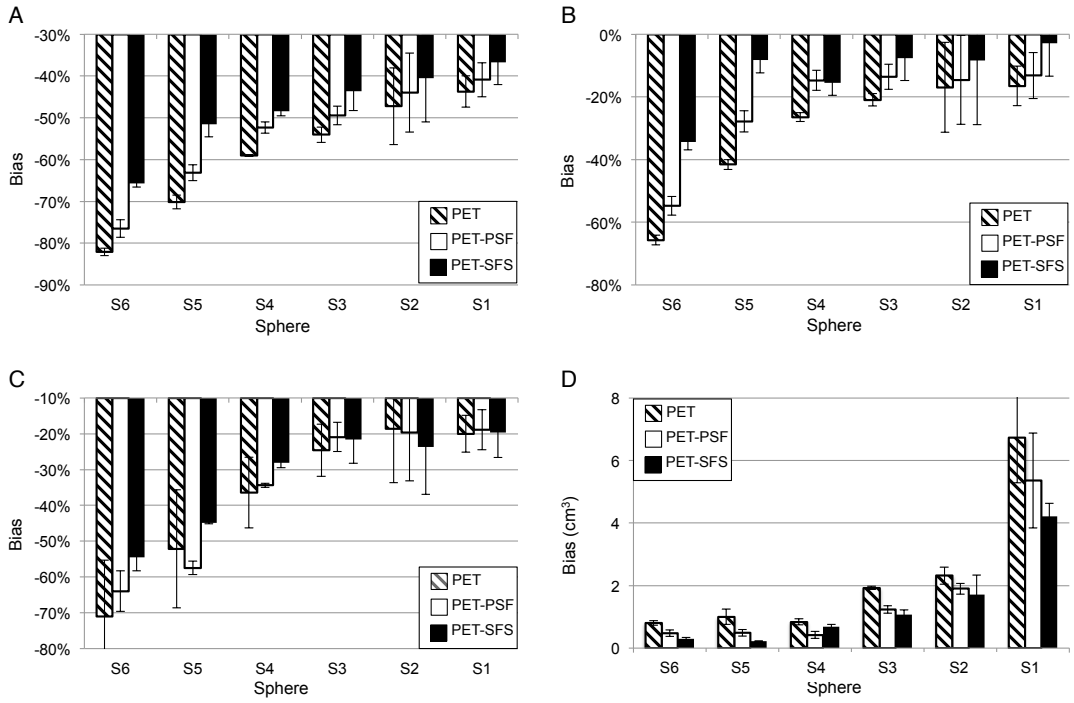

Figure 4.5: Activity quantification and MATV estimates bias obtained as an average among the three phantom experiments. A-C) comparison of percentage differences from ground truth in A) SUVmean, B) SUVmax and C) SUVpeak; D) comparison of absolute differences from ground truth in sphere MATV estimates (x-axis sphere are in reverse order compared to a-c). Bias comparison of images obtained with different modalities: standard PET (dark gray bar), PET with PSF reconstruction (light grey bar) and PET corrected with SFS-RR algorithm (black bar).

The better performances of the SFS-RR algorithm are upheld by the root mean square error (RMSE) and contrast to noise ratio (CNR) comparison in Figure 4.6. Images resulting from the application of the SFS algorithm show lower RMSE on average (up to

15% compared to standard PET for the smallest sphere) while being consistent with the trend of the RMSE increasing for smaller spheres. It is of note that the improved image resolution does not come with a detriment of image quality as noise levels are contained with CNR either higher or comparable with the standard PET image.

4.3.2 Clinical Dataset

The analysis of clinical data have been performed comparing Standard PET and PET corrected with SFS-RR algorithm; the PSF reconstruction has been excluded since it is not performed in clinical practice. However, in order to have a complete overview, in Figure 4.7 is reported an example of follow-up patient images reconstructed with the inclusion of the PSF. From a qualitative perspective one can note that, despite the improved image sharpness, the noise level increases.

The influence of using the SFS-RR algorithm on real patient data can be appreciated qualitatively in Figure 4.8-4.11 where the Maximum Intensity Projection (MIP) and two different transaxial views are displayed for a representative subject.

There is a clear increase in lesion sharpness following the application of a resolution recovery technique. The quantitative characterization of all lesions of this specific subject is reported in Figure 4.12 and Table 4.3.2.

The transaxial views of Figure 4.8 is a good example of the effect in lesion definition and characterization using the SFS-RR algorithm. Sharper contours and the activity recovery in the PET-SFS images for the rib lesion (Figure 4.8, transaxial view, red marker) and also in the spine (Figure 4.8, transaxial view, blue marker) are evident, and in the spine lesion it is easier to appreciate that the activity is in the periphery of the lesion where there is greatest osteoblastic activity compared to the relatively photopenic center. In terms of quantitative characterization there is an increase in the SUV_{mean} estimates of 60% (rib lesion, SUV_{PET} =30.7 SUV_{SFS} =49.1) and 43% (spine lesion, SUV_{PET} =23.2 SUV_{SFS} =33.1) from the standard-PET to the PET-SFS. In contrast, the automatic segmented MATV has a relative reduction of 25% (rib lesion, $MATV_{PET}$=2.7cm^3 $MATV_{SFS}$ =2.1cm^3) and 31% (spine lesion, MAT_{PET}=7.5cm^3 $MATV_{SFS}$=5.2cm^3).

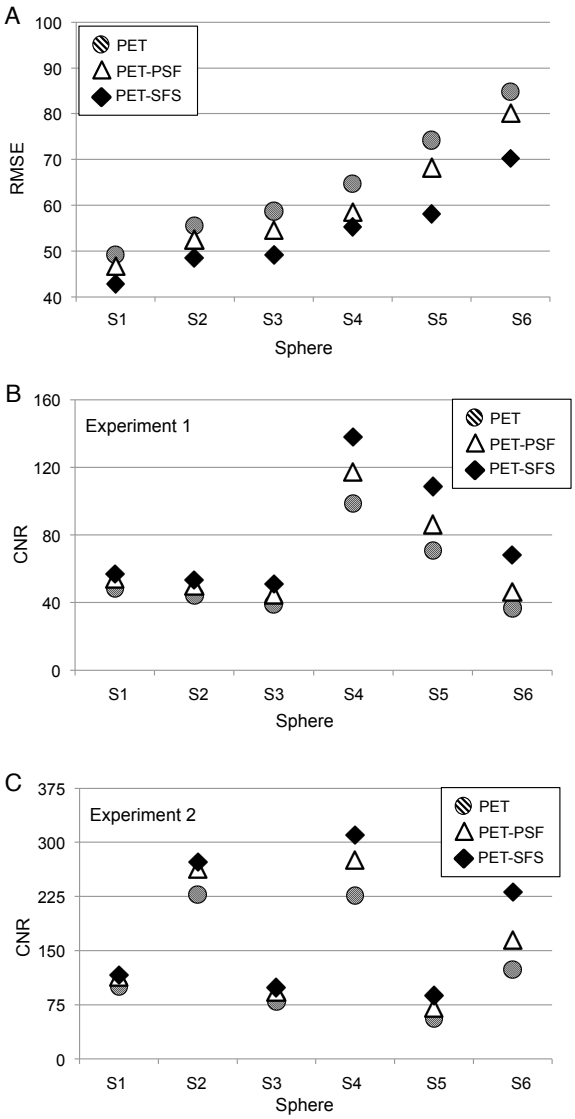

Figure 4.6: Root mean square error and noise analysis. For each sphere (S1-S6) three values corresponding to images obtained with different modalities are reported: standard PET (dashed circle), PET with PSF reconstruction (white triangle) and PET corrected with SFS-RR algorithm (black diamond) A) Root mean square error for the six spheres obtained as an average among the three phantom experiments. B-C) Contrast to noise ratio computed for each sphere against a uniform region in the phantom background. Only experiments 1 and 2 are reported for consistency reasons (in experiment 3 three spheres have zero activity).

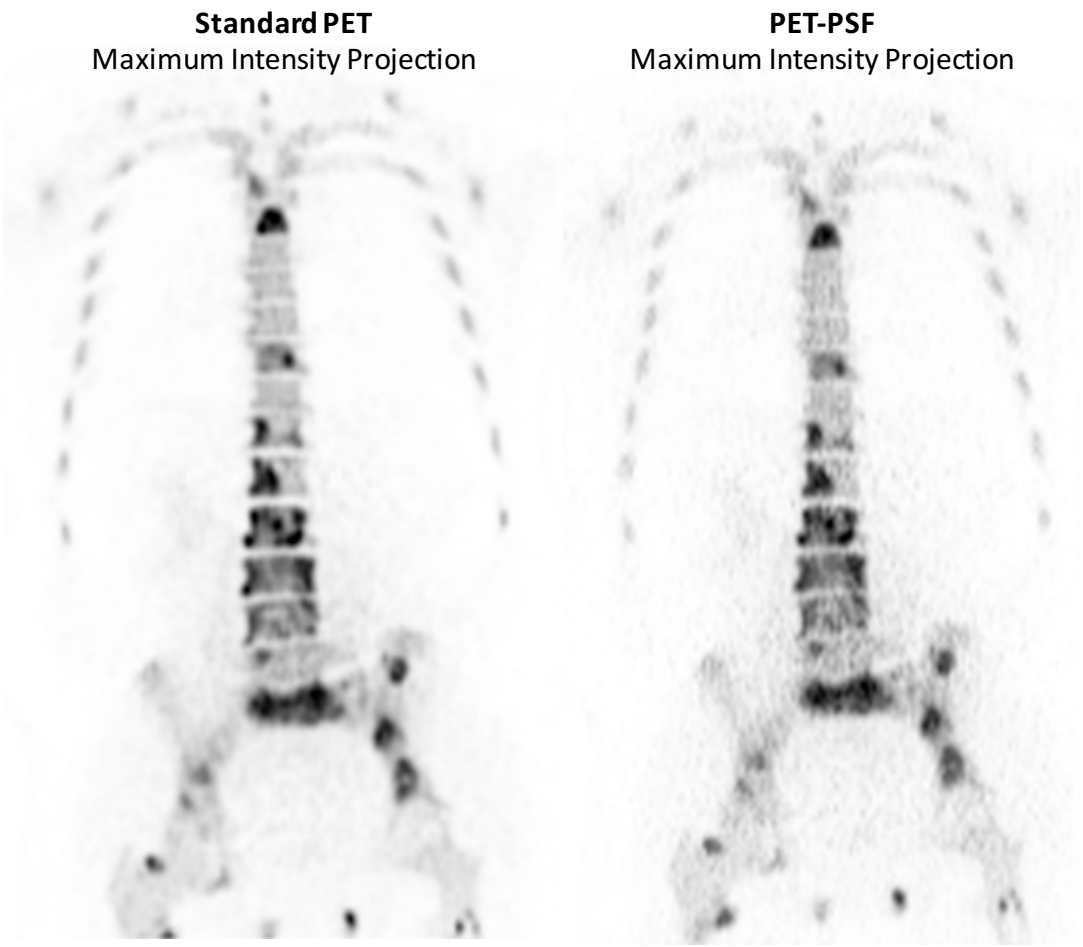

Figure 4.7: Maximum Intensity Projection (MIP) and transaxial views of a representative subject (Patient 08 - Follow-up). Left Panel - Standard PET; Right Panel - PET reconstructed with PSF model

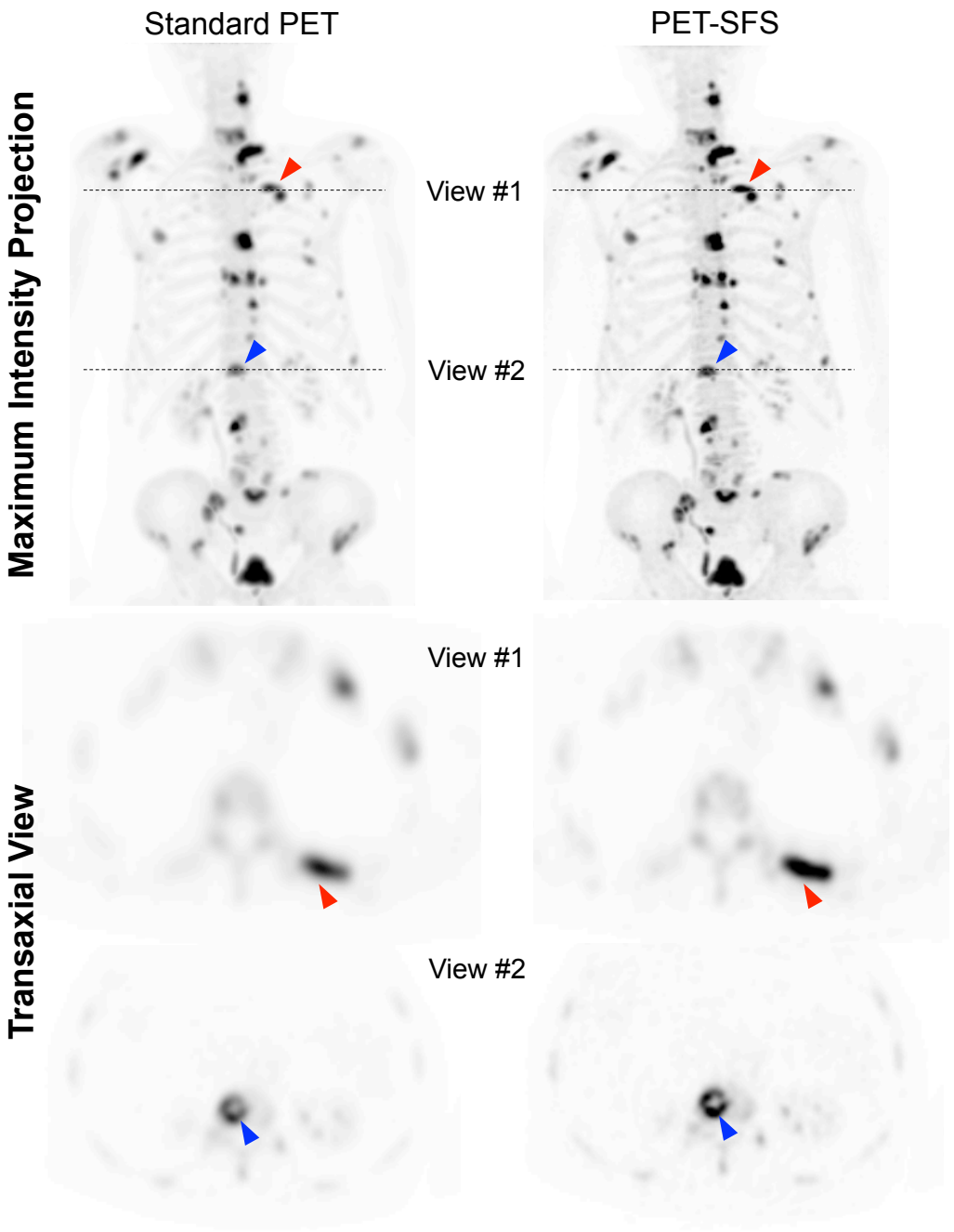

Figure 4.8: Maximum Intensity Projection (MIP) and transaxial views of a representative subject (Patient 01). Left Panel - Standard PET; Right Panel - PET corrected with SFS-RR algorithm. The red and blue markers highlight two representative lesions (spine and rib respectively) that appear sharper in the PET-SFS image compared to the standard PET one. Dashed lines indicate the slice position of the transaxial views reported below the MIP.

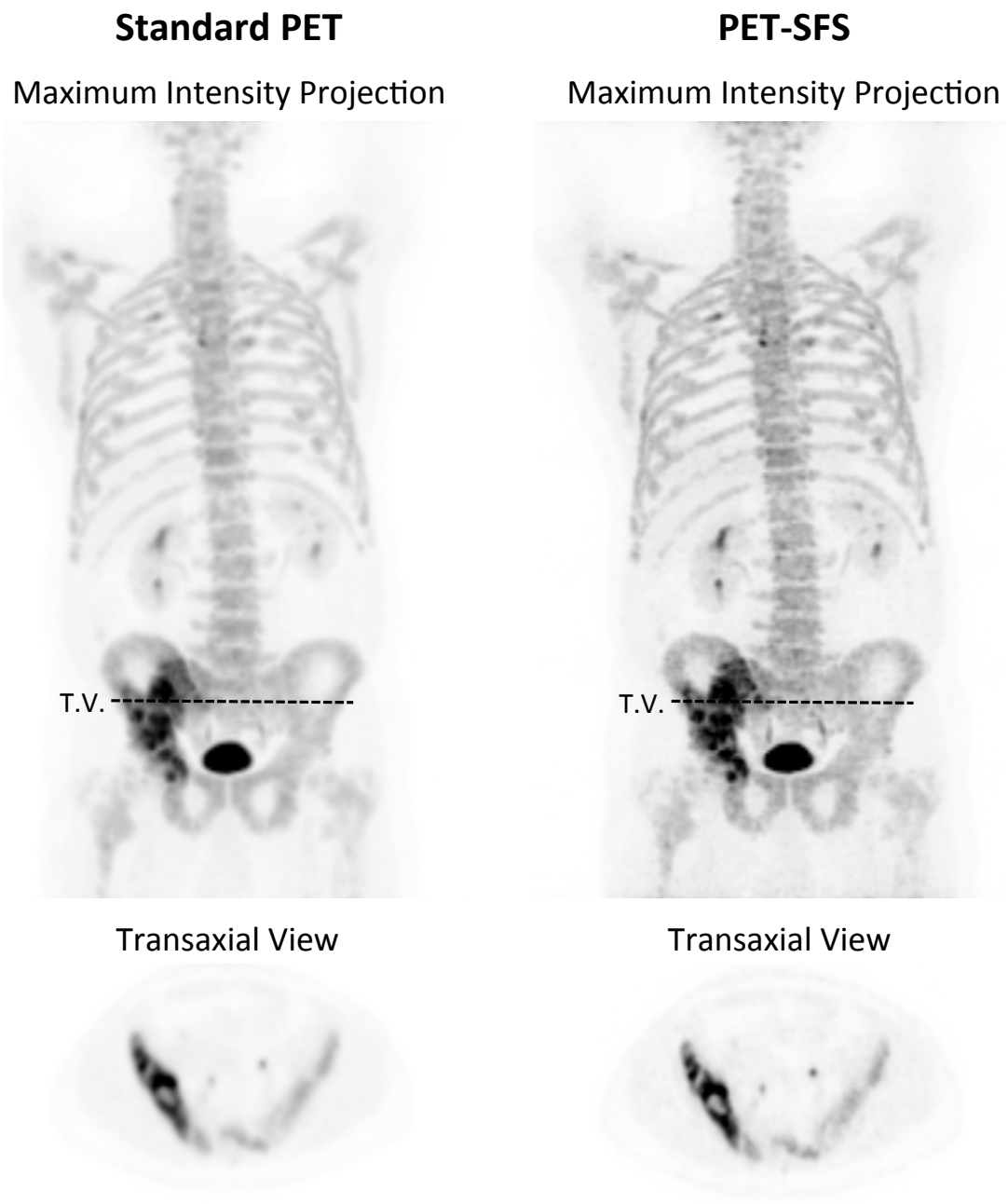

Figure 4.9: Upper Panels Maximum Intensity Projection (MIP) view of Patient02. Lower Panels Transaxial view corresponding to the dashed line reported on the MIP. Left Panels Standard PET; Right Panels PET corrected with SFS-RR algorithm.

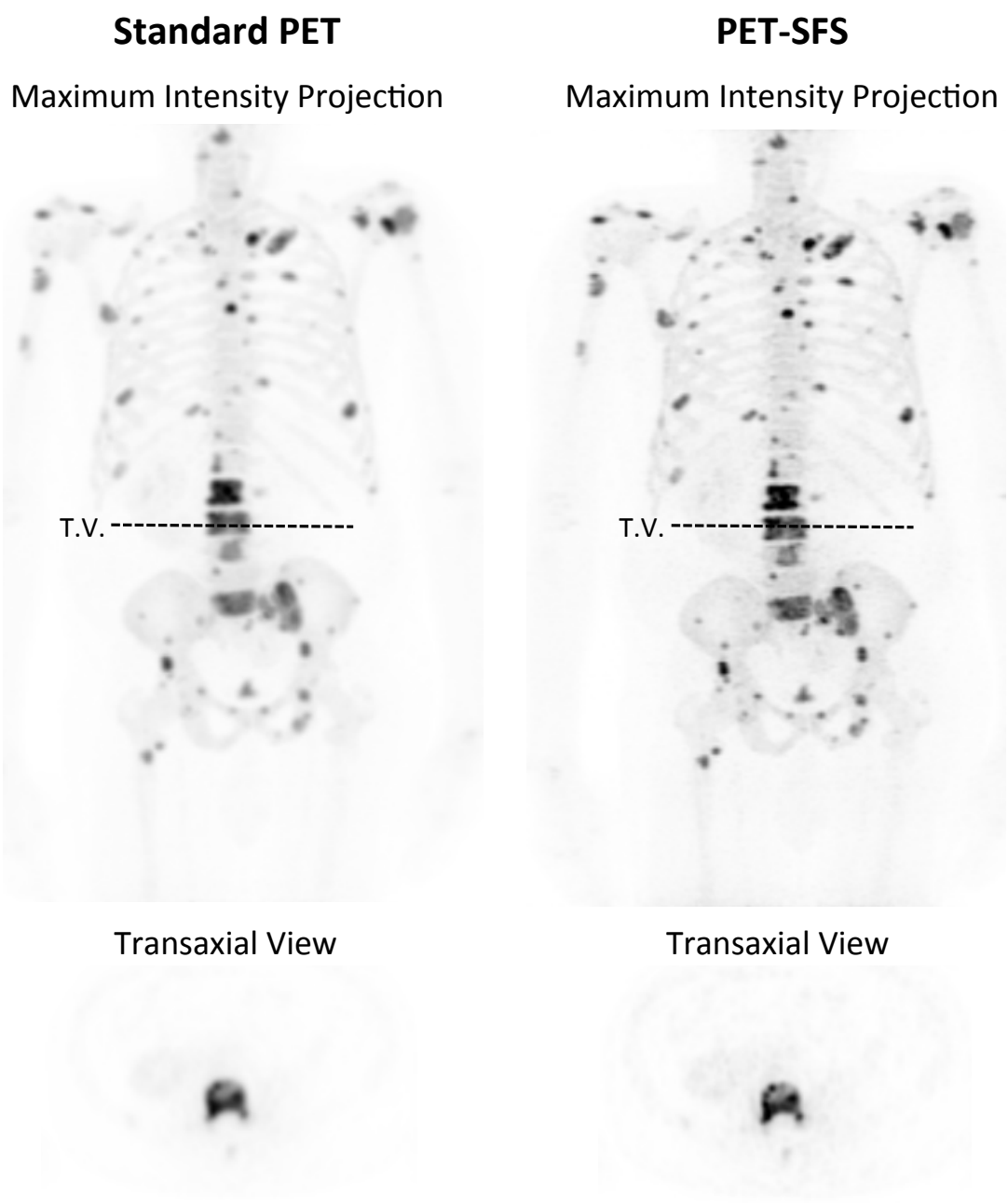

Figure 4.10: Upper Panels Maximum Intensity Projection (MIP) view of Patient03. Lower Panels Transaxial view corresponding to the dashed line reported on the MIP. Left Panels Standard PET; Right Panels PET corrected with SFS-RR algorithm.

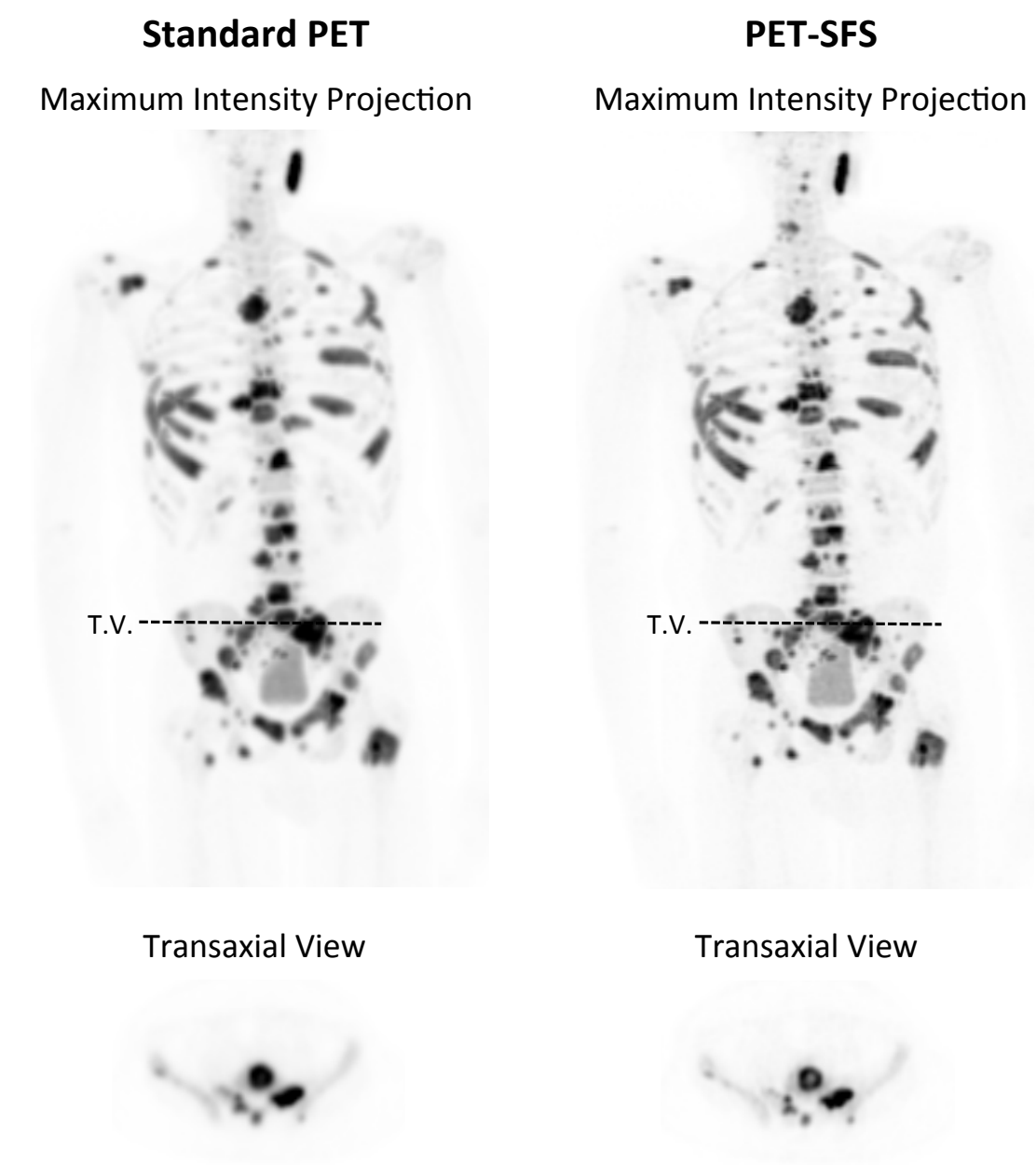

Figure 4.11: Upper Panels Maximum Intensity Projection (MIP) view of Patient04. Lower Panels Transaxial view corresponding to the dashed line reported on the MIP. Left Panels Standard PET; Right Panels PET corrected with SFS-RR algorithm.

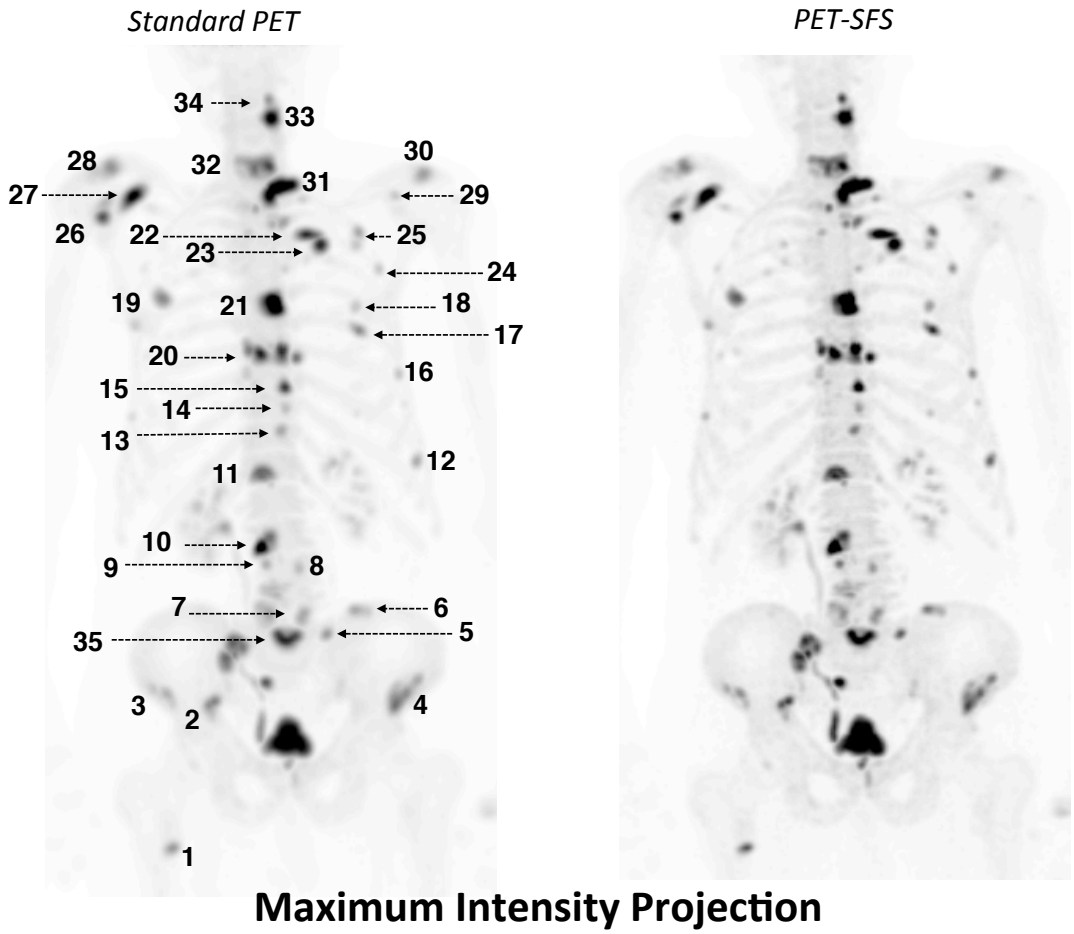

Figure 4.12: Maximum Intensity Projection view of Patient01. Left Panel Standard PET; Right Panel PET corrected with SFS-RR algorithm. Lesions indexes are also reported (right panel). Corresponding SUVs and volumes estimates are reported in Supplementary Table 4.3.2.

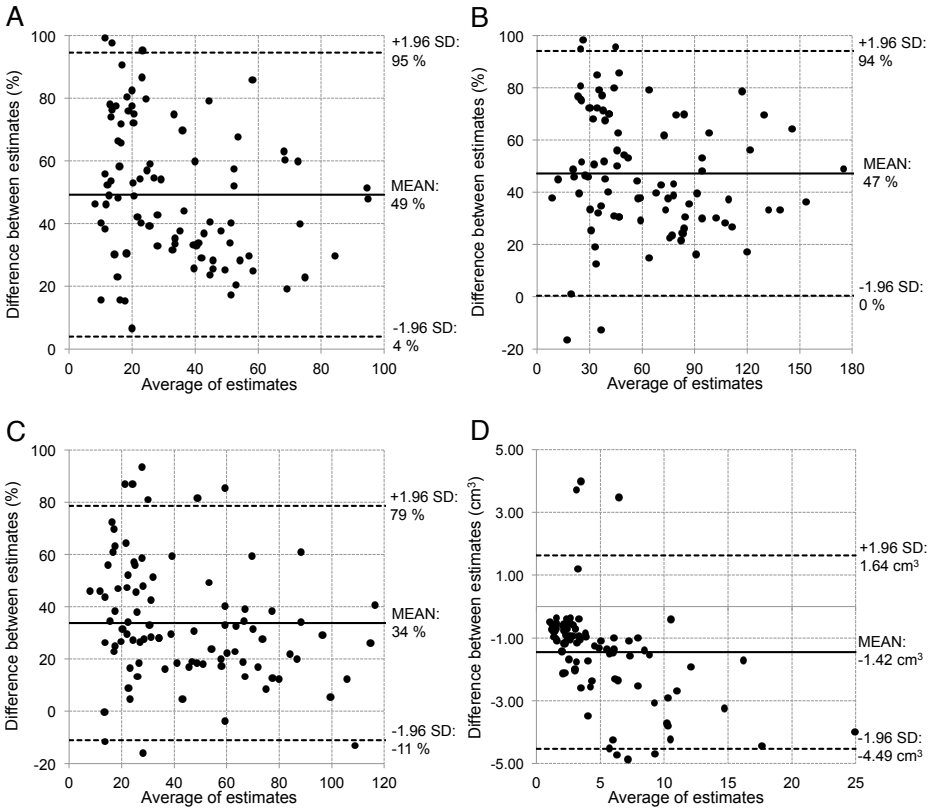

Figure 4.13: Bland-Altman plots showing the differences in MATV and activity quantification when estimates are computed in images obtained with standard PET and PET corrected with the SFS-RR algorithm. Each grey circle represents a specific lesion; all lesions of all patients are reported. The differences between estimates for SUVmean (A), SUVmax (B) and SUVpeak (C) are reported as the relative percentage difference. The MATV (D) is reported as absolute difference in cm^3

A comprehensive comparison of the quantitative differences due to application of the SFS-RR algorithm is reported in Figure 4.13. As previously performed for Patient 01 (Figure 4.12 -Table 4.3.2 Supplementary Materials B) we segmented all lesions of the remaining patients and collected the corresponding values of SUV$_{mean}$, SUV$_{max}$, SUV$_{peak}$ and MATV. Figure 4.13 reports the relative differences (SUVs and MATV) between lesions segmented in standard PET and PET-SFS images for the entire datasets.

There is a general increment in activity estimates for PET-SFS compared to standard PET. The average increments for different indexes are as follow: SUV$_{mean}$ = 49$\%$, SUV$_{max}$ = 47$\%$ and SUV$_{peak}$ = 34$\%$. For low activity lesions the range of differences in the estimates is larger than for more active lesions indicating that the algorithm efficiency is dependent on signal to noise ratio. For the MATV there is an average reduction of 1.4cm^3 when segmentation is performed on PET-SFS images. When lesion size increases the difference reached values of 4-5cm^3, which might be relevant if patient classification were based on characterization of the larger detectable lesions.

4.4 Discussion

In this work we evaluated the influence of a multimodal partial volume correction technique on the quantification and assessment of metastatic bone lesions from primary prostate and breast cancers. It is worth remarking that this work targets specifically to 18F-Fluoride PET/CT bone scans as SFS-RR obviously produces better results the stronger is the correspondence between functional and structural signals. Our results showed an average 50$\%$ increase in SUV$_{max}$ and SUV$_{mean}$ and a 30$\%$ increase in the SUV$_{peak}$ for partial-volume corrected images when compared with the standard PET, depending on lesion size (lesion volume range 0.525cm^3). Our results are in agreement with findings in similar experimental settings from previous studies [48, 52]. Although SUV$_{max}$ estimates depend on image noise, the 50$\%$ increase is not a consequence of noise bursts given the comparable RMSE between the SFS-RR corrected images and standard PET images.

The higher activity recovery and the good noise control from the phantom analysis indi-

cate a better image quality when the SFS-RR algorithm is applied. Indeed patient images show lesions with sharper and better-defined contours, which result in improved lesion conspicuity and segmentation even for smaller volumes. To note that the CNR depends on the absolute activity value and that explains why on Figure 4.6 one set of spheres show higher CNR than the other.

The results from the phantom experiments showed that the SFS-RR images outperform both standard PET and PSF images in terms of image quality and quantification accuracy. PSF-based image reconstruction is known to contribute to the appearance of artefacts [114] and is computationally cumbersome hence is not performed in routine clinical studies in our Unit. Furthermore, when a representative whole body patient image was reconstructed with the inclusion of the PSF model, an increase in image noise was detected. For these reasons standard PET was used as a reference for SFS-RR images when it came to patients image analysis. In this regard, it is worth noting that no artefacts have been generally observed in this and previous applications of SFS-RR which is now a mature enough technology worth further testing in the clinical setting.

It is worth highlighting the robustness of the methodology regarding possible mismatch between PET and CT images. Phantom acquisitions showed that even if some structures are only visible on the functional images, they are preserved after the application of the algorithm. This is of importance because lesions that might be lost in the CT segmentation, for example because their size is too small or the metastasis does not show sufficient bone mineralization to appear sclerotic, they will still be visible in the final enhanced PET images.

Although the SFS-RR algorithm showed qualitatively and quantitatively better images than standard PET, further analyses are necessary to quantify the influence of the improved image quality on the assessment of patient skeletal staging and therapy response. This may allow better definition and quantification of lesions following therapy or allow greater detectability and segmentation of metastatic spread at staging. Of interest would be also to evaluate whether lesion heterogeneity is affected by higher resolution and evaluate the consequent impact on textural analysis, given its increasing oncological ap-

plications [30, 49].

4.5 Conclusions

We have proposed and tested on a set of phantom studies and demonstrated on clinical data a multimodal methodology for quantitative resolution recovery for whole body PET-CT, here specifically designed for [^{18}F]Fluoride PET imaging of bone metastases. The technique allows rapid and straightforward application and produces images of significant improved visual quality and quantitative properties.

However, this approach might not be an ideal choice for different clinical applications. Despite in the current formulation the segmentation of the subject structural image does not require the use of atlases or user input, this might not always be the case. It might be difficult to define neat segmentation rules for other types of structural acquisitions. These considerations provide the motivation for the next chapter in this thesis, where a PVC technique is formulated for brain [11C]PIB PET/MRI myelin imaging. Specifically, myelin lesions are not as straightforward as bone lesion to automatically segment on MRI images given their lower contrast and high heterogeneity (the lesion tissue comprises of peri-lesion, lesion, black hole and Gadolinium enhanced lesion). Manual segmentation is also not feasible, given the high number and size variability of lesions. From this premise stems the proposal of the novel PVC approach presented in the next Chapter, which does not require any structural image pre-processing.

	SUVmean		SUVmax		SUVpeak		MATV [cm^3]	
Lesion	PET	PET-SFS	PET	PET-SFS	PET	PET-SFS	PET	PET-SFS
1	14.41	25.59	29.10	48.73	19.62	30.62	2.69	1.27
2	10.10	15.06	22.27	32.60	15.42	1.28	9.56	4.69
3	17.78	27.43	35.33	57.45	25.05	31.96	5.50	2.93
4	19.25	20.52	38.88	33.91	30.54	25.63	12.08	8.36
5	15.00	26.24	30.57	52.00	20.78	30.27	2.08	1.03
6	12.36	19.56	23.68	39.81	17.62	23.18	4.01	2.25
7	15.01	25.81	30.57	52.00	19.20	25.79	2.18	1.08
8	8.32	11.68	19.30	19.53	13.48	13.43	5.77	2.27
9	11.45	21.84	23.92	44.20	16.80	31.39	2.74	1.30
10	37.16	52.24	76.45	106.60	54.62	72.46	5.18	3.91
11	23.26	33.08	41.12	62.92	33.91	39.38	7.53	5.18
12	13.15	23.71	25.31	45.33	14.73	27.55	1.78	1.25
13	9.63	14.67	16.42	24.43	13.19	17.76	4.77	2.18
14	9.31	10.75	18.70	15.60	14.62	12.93	4.89	3.15
15	26.64	45.22	55.17	89.25	34.76	63.11	2.79	1.59
16	9.14	18.05	17.44	34.60	11.86	20.46	1.49	1.00
17	17.37	31.21	32.78	60.82	21.43	34.00	1.88	1.17
18	9.25	16.47	17.78	32.12	11.61	18.11	1.71	1.12
19	17.96	25.50	33.77	47.35	23.99	30.34	3.77	2.81
20	28.46	38.51	59.49	68.29	42.15	44.05	11.61	6.92
21	47.53	60.96	88.69	115.52	75.39	84.73	6.77	5.40
22	30.68	49.04	59.11	100.23	42.74	63.77	2.76	2.05
23	29.80	42.89	58.43	83.39	41.35	57.07	3.11	2.18
24	8.64	17.37	16.90	32.91	12.69	21.53	1.56	1.23
25	12.02	20.67	25.04	43.14	16.31	26.78	3.99	2.00
26	22.88	35.25	46.60	67.20	33.73	43.63	3.99	1.96
27	35.20	44.25	67.93	83.17	52.46	62.85	5.65	4.55
28	14.90	17.25	30.28	36.10	24.44	27.69	9.63	8.09
29	7.65	15.24	17.89	29.83	11.26	16.18	3.13	1.00
30	13.79	16.95	27.25	34.19	21.34	24.89	6.23	4.87
31	43.74	58.49	81.85	106.39	66.42	77.65	9.19	6.65
32	24.07	31.98	48.69	67.02	37.60	44.50	12.59	8.36
33	36.75	47.41	69.06	85.36	54.23	66.19	4.25	3.40
34	16.09	30.02	31.23	56.12	21.37	38.67	1.76	1.05
35	29.73	40.90	56.80	79.30	44.63	52.91	7.31	5.01

Table 4.3: Standardized Uptake Values (SUVmean, SUVmax, SUVpeak) and Metabolic Active Tumor Volume (MATV) estimates computed for all the lesions indexed in Figure 4.12 after automated segmentation. Values are reported for estimates obtained from the standard PET and PET corrected with the SFS-RR algorithm images.

Chapter 5

Multimodal Partial Volume Correction - Application to [^{11}C]PIB PET/MRI myelin imaging in multiple sclerosis

5.1 Introduction

Multiple sclerosis MS is a complex neurological disease that represents the first non-traumatic cause of neurological disability among young adults [91]. MS pathophysiology is characterized by an auto-immune aggression of myelin sheaths resulting in demyelinated lesions and axonal degeneration. Myelin is however a dynamic tissue and there is strong evidence in animal models that myelin repair is an efficient process which may follow myelin insult [40]; however little is known about the dynamics of re-myelination in patients with MS. Sensitive imaging tools are now required to measure myelin dynamics in vivo and understand spontaneous re-myelination in MS patients as well as to act as biomarkers for new pro-myelinating therapies.

Positron emission tomography (PET) with [^{11}C]PIB was originally developed to image amyloid deposition in neurodegenerative disorders and dementia [63] and has been recently repurposed as an accurate imaging probe for myelin *in vivo* [108, 125, 9]. Demyelination (or re-myelination) evaluation criteria consist of lesion detection, quantification of myelin content and comparison between baseline and follow-up scans. In this

perspective, the influence of partial volume effect (PVE) is of importance when detecting and quantifying myelin content changes in lesions, considering the typical poor image resolution of PET and quantification bias resulting from activity spill-in.

The literature provides a wide range of partial volume correction (PVC) techniques to address the PVE in PET imaging [96]. One group is represented by region-of-interest (ROI) based methods, which are however limited by the assumption of radiotracer homogeneous distribution and is inapplicable here [96, 5]. Alternatively, voxel-based techniques are available like partition-based [77] and multiresolution [16, 104] methods. A distinct final approach consists of incorporating a model of the system point spread function (PSF) into the reconstruction algorithm [89, 92].

The aim of this study was to achieve better myelin delineation and quantification in [^{11}C]PIB PET/MR brain images through successful image resolution recovery leading to PVC. The Multiresolution-Multimodal Resolution-Recovery MM-RR method presented stems from previous works on brain PET/MR [104, 74, 59, 105] and whole-body PET/CT [44]. Similarly to this work, the relation between functional (PET) and anatomical (MR) information is exploited in a synergistic fashion for a realistic noise-controlled recovering of PET image resolution. However, the new algorithm takes a step further by means of creating a more robust statistical model of the relationship between functional and structural information that results in an accurate quantification of cold lesions, more relevant in MS imaging, as well as hot areas.

The choice of [^{11}C]PIB PET/MR myelin imaging in MS is not fortuitous, as this clinical application offers a perfect example of exquisite correlation between functional (PET) and structural (MR) signals. As outlined in Figure 1, myelin sheath is characterized by a repetition of major dense layers (80$\%$ lipid and 20$\%$ protein lamellar structure) alternated with an extracellular space characterized by a relatively high-water content (WC) up to 40$\%$ of myelin weight [81]. There is consensus in literature that the high WC is one of the primary causes for T1 relaxation in newborns. However for subjects older than 2 years of age conventional T1- and T2- weighted signals have lower specificity and should be considered a qualitative myelination measure (Figure 1B) [37, 68]. The source of

PET signal is instead ascribed to the presence of myelin basic protein (MBP) in the lipid-protein bilayer (Figure 1C). In intact myelin sheath the MBP clasps together adjacent myelin layers; in doing so it gathers a secondary structure characterized by $\beta-$pleated sheets that attract the ligand [94]. A number of studies have demonstrated that PIB and other compounds with similar planar rigidity (Stilbene and Benzothiazole derivatives also used for amyloid imaging) are characterized by high affinity to such $\beta-$sheets structures [130] generating a specific source of signal in [^{11}C]PIB PET myelin imaging (Figure 1D).

5.2 Materials and Methods

5.2.1 Image Resolution Recovery

The Multiresolution-Multimodal Resolution-Recovery (MM-RR) algorithm stems from previous works on partial volume correction [104, 44] and denoising [118] where the structural information (CT or MRI) is exploited to improve the image quality of the functional counterpart (PET). As for existing anatomical-driven resolution recovery techniques, MM-RR is based on a wavelet decomposition of both functional and structural images.
In existing techniques, the high-frequency wavelet coefficients are transferred via weighted sum from the high-resolution anatomical image to the PET after appropriate statistical scaling. However, prior to wavelet decomposition, the anatomical image is segmented by means of tissue classification based on anatomical image intensity levels or using anatomical atlases.
In the formulation presented here, the image resolution recovery depends on the ad-hoc modeling of the relationship between low-frequency information of PET and MR that is then used to insert high-frequency MR data into the PET image after appropriate scaling and denoising.

Wavelet decomposition MM-RR algorithm

The wavelet transform (WT) decomposes a 1D signal $f(x)$ into its high- and low- frequency components though the filter bank as follow

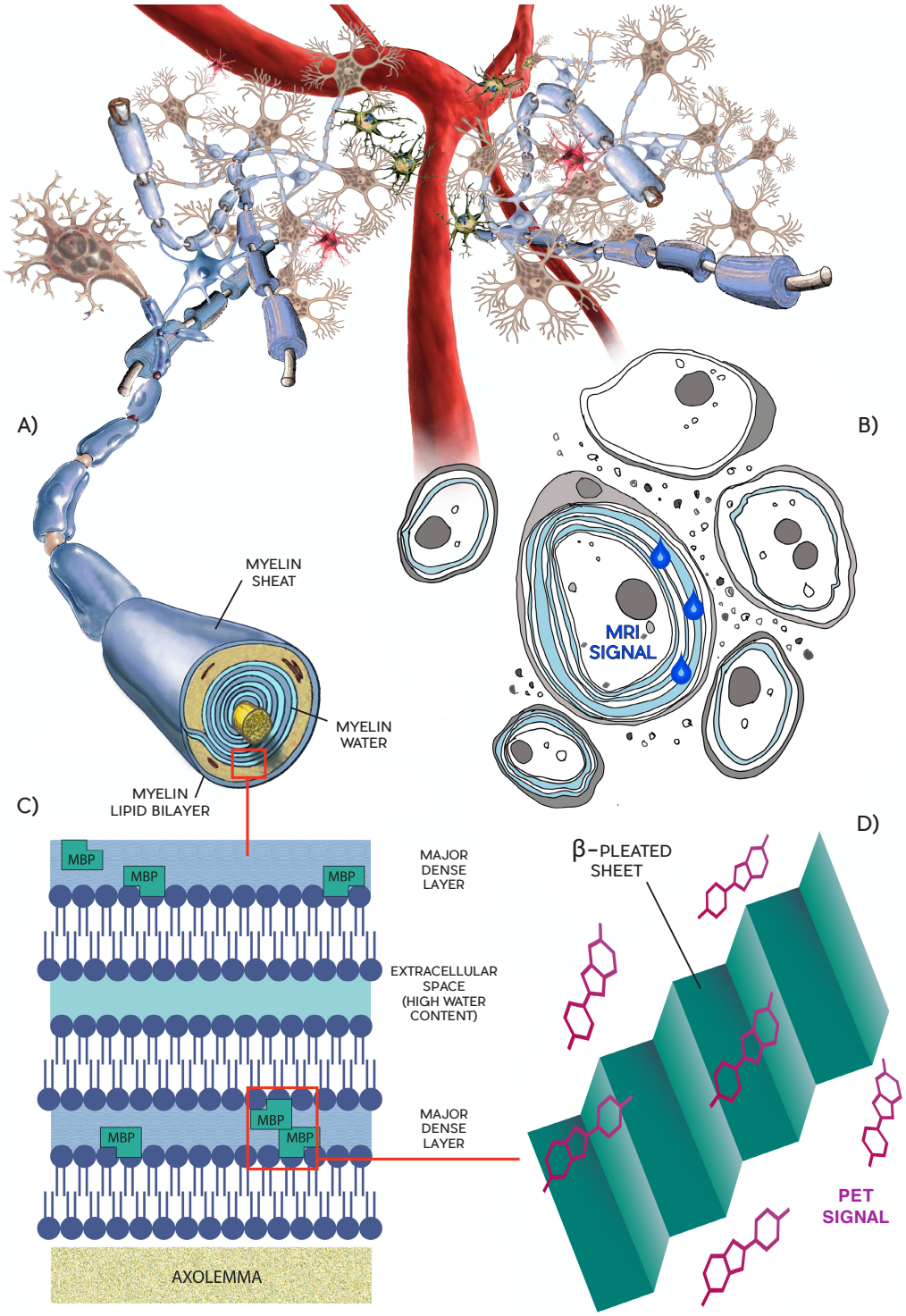

Figure 5.1: Graphical description of PET/MRI myelin source signal starting from the brain axonal network down to molecular level. A) Axon structure with visible alternation of myelin lipid bilayer and myelin water content; B) Representation of T1-w and T2-w MRI source signal due to myelin high water content as from panel A); C) detailed representation of myelin structure where is highlighted the presence of myelin basic proteins (MBP) within the lipid bilayer; D) schematic representation of PET source signal - PIB high affinity with the -pleated sheet structure of MBP.

$$f(x) = \sum_{k} \sum_{j-1}^{J} d_j(k) \cdot \psi_{j,k}(x) + \sum_{k} C_j(k) \cdot \phi_{J,k}(x) \tag{5.1}$$

where j is usually referred to as the decomposition/resolution level, ψ is a high band-pass function and ϕ is a low-pass scaling function while $d_j(k)$ and $C_j(k)$ are their resulting coefficients (respectively wavelet and low resolution coefficients).

In tomographic imaging applications the input signal is no longer mono dimensional, therefore its components have to be represented by 3-dimensional wavelet and scaling functions. In this case the transform generates 8 components from a 3D input signal while applying the one-dimensional decomposition (high- and low- pass filters) successively along the three x, y, z directions. The low resolution coefficients resulting from the application of the low-pass filter to all x, y, z directions represent the input signal for the second level wavelet decomposition $j = 2$. We refer to Figure 5.2 for a graphical representation of the 3D wavelet decomposition.

In this work, as in previously proposed PVC techniques [104, 44], we preferred the dual-tree complex wavelet transform (DT-CWT) [61] to the more used dyadic wavelet transform (DWT) [72] in order to achieve better directional selectivity, shift invariance and more exact reconstruction.

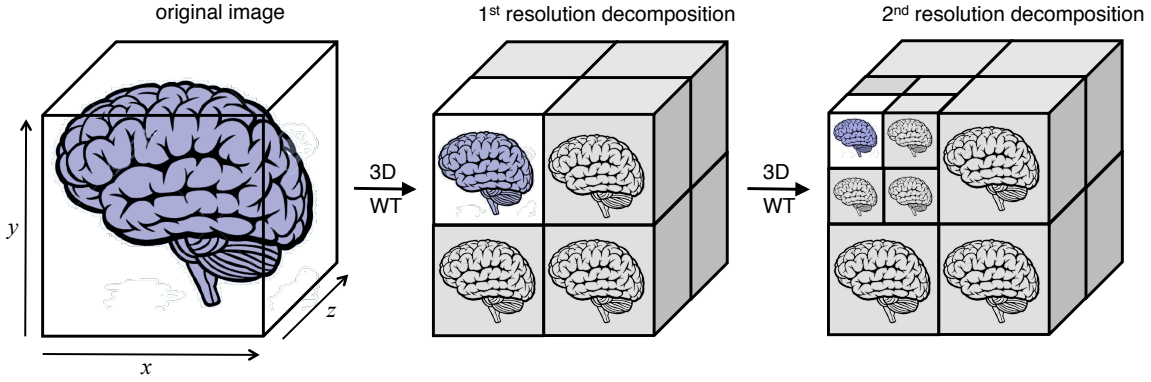

Figure 5.2: Graphical representation of wavelet decomposition when applied to a 3D volume as a tomographic scan

Scaling Factors

Initially, both functional (PET) and anatomical (MRI) images are decomposed by means of the DT-CWT into several resolution elements up to resolution level $j = 2$ and the wavelet ($\mathscr{W}^{PET}$, $\mathscr{W}^{MRI}$) and low resolution ($\mathscr{L}^{PET}$, $\mathscr{L}^{MRI}$) coefficients collected into separate matrixes.

The algorithm requires two scaling factors to account for the resolution difference between the two imaging modalities (*inter-modality resolution* and *global coefficient* scaling factors) and a weighting factor accounting for the difference between subsequent wavelet resolution levels (*intra-modality resolution* scaling factor). The *inter-modality resolution* scaling factor R compensates for the difference in resolution between the two imaging modalities. The magnitude of wavelet coefficients depend on the spatial resolution of the image, therefore the scaling coefficient is obtained as the ratio of the coefficients of the original anatomical image with a smoother version which is degraded to PET scanner resolution through a 3-dimensional Gaussian filtering in image space.

$$R^{\mathscr{L}} = \frac{\sum \mathscr{L}^{MRI}}{\sum \mathscr{L}^{MRIs}} \qquad R^{\mathscr{W}} = \frac{\sum \mathscr{W}^{MRI}}{\sum \mathscr{W}^{MRIs}} \tag{5.2}$$

The *global coefficient* scaling factor G compensates for the difference in intensity between PET and MRI coefficients. Note that in Eq 5.3 the PET coefficients are multiplied with the *inter-modality resolution* scaling factor R for consistency purposes

$$G^{\mathscr{L}} = \frac{R^{\mathscr{L}} \cdot \sum \mathscr{L}^{PET}}{\sum \mathscr{L}^{MRI}} \qquad G^{\mathscr{W}} = \frac{R^{\mathscr{W}} \cdot \sum \mathscr{W}^{PET}}{\sum \mathscr{W}^{MRI}} \tag{5.3}$$

The PET and MRI wavelet and low-resolution coefficients are then respectively multiplied by the inter-modality resolution and the global coefficient scaling factors within the algorithm iterative steps.

MM-RR algorithm

The first step of the algorithm consists of creating a correlation model between the functional and structural information taking into account only the one quadrant containing the

low resolution coefficients as depicted in Figure 5.3A

$$\mathscr{L}^{model} = \alpha \cdot G^{\mathscr{L}} \cdot \mathscr{L}^{MRI} + \beta \tag{5.4}$$

$$residuals_{\mathscr{L}} = G^{\mathscr{L}} \cdot \mathscr{L}^{MRI} - \mathscr{L}^{model} \tag{5.5}$$

where α and β are the slope and intercept of the red regression line ($\mathscr{L}^{model}$) which is stored together with the $residuals_{\mathscr{L}}$ before moving on with the analysis of the wavelet coefficients.

In the following iterative steps, each quadrant of the wavelet coefficients decomposition is analyzed separately. In each quadrant a correlation analysis is performed between the functional and structural high-resolution wavelet coefficients ($\mathscr{W}^{PET}$, $\mathscr{W}^{MRI}$). The coefficients that fall in the second and fourth quadrant are discarded before calculating the correlation model since they result from image noise.

$$\mathscr{W}^{model} = \alpha \cdot G^{\mathscr{W}} \cdot \mathscr{W}^{MRI} + \beta \tag{5.6}$$

Once the linear model is computed, the residuals are calculated (Figure 5.3B) and stored (Figure 5.3C).

$$residuals_{\mathscr{W}} = G^{\mathscr{W}} \cdot \mathscr{W}^{MRI} - \mathscr{W}^{model} \tag{5.7}$$

The residuals are then added to the correlation model $\mathscr{L}^{model}$ obtained from the low-resolution coefficients at the first step to obtain the final coefficients of the improved PET image (Figure 5.3C).

$$\mathscr{W}^{newPET} = \mathscr{L}^{model} + residuals_{\mathscr{W}} \tag{5.8}$$

To note in Eq 5.8 is that the correlation model obtained with low-resolution coefficients Eq 5.4 is used as foundation in the computation of the coefficients for the new high resolution PET. Since the magnitude of the coefficients increases as the decomposition proceeds to finer resolution levels, an *intra-modality resolution* scaling factor Λ accounting for this difference is needed.

We used a robust measure of the noise variance computed for each resolution level ($\sigma_{\mathscr{L}}$

and $\sigma_{\mathscr{W}}$) to account for this scaling factor. Precisely we computed the m*edian absolute deviation MAD* [33, 120].

$$\sigma_{\mathscr{L}} = MAD\{residuals_{\mathscr{L}}\} \tag{5.9}$$

$$\sigma_{\mathscr{W}} = MAD\{residuals_{\mathscr{W}}\} \tag{5.10}$$

Once the measures of the noise variance are known, the *intra-modality resolution* scaling factor Λ is computed as the ratio between different resolution levels as in Eq 5.11 and integrated in the final model of Eq 5.8 to obtain Eq 5.12

$$\Lambda = \sigma_{\mathscr{W}}/\sigma_{\mathscr{L}} \tag{5.11}$$

$$\mathscr{W}^{newPET} = \mathscr{L}^{model} + \Lambda \cdot residuals_{\mathscr{W}} \tag{5.12}$$

Once the new wavelet coefficients ($\mathscr{W}^{newPET}$) are calculated iteratively for all the wavelet quadrants, an inverse wavelet transform is performed to obtain the new high resolution PET image (Figure 5.3D).

5.2.2 Dataset

The impact of the proposed PVC technique was tested with two datasets from the same study comprising [^{11}C]PIB PET and MR images. For the first part of the study 10 healthy control subjects (3 male, 7 female, age: 29.5 $\pm$ 6.2 years) were enrolled. Inclusion criteria consisted in an age between 18 and 55 years and the exclusion of any known neurological or psychiatric condition. Each volunteer undertook two separate scans, at baseline and a retest scan performed within approximately 1 month from the first one. The second set comprised of 20 relapsing-remitting MS patients (7 male, 13 female, age: 32.3 $\pm$ 5.6 years) with at least one gadolinium enhancing (Gd+) lesion over 6mm in diameter on magnetic resonance imaging (MRI) at study entry. Ethical approval was granted by the ethics committee of the Pite-Salpetriere Hospital (Approval No. P080503) and informed consent was obtained from all participants. This study was conducted according to the

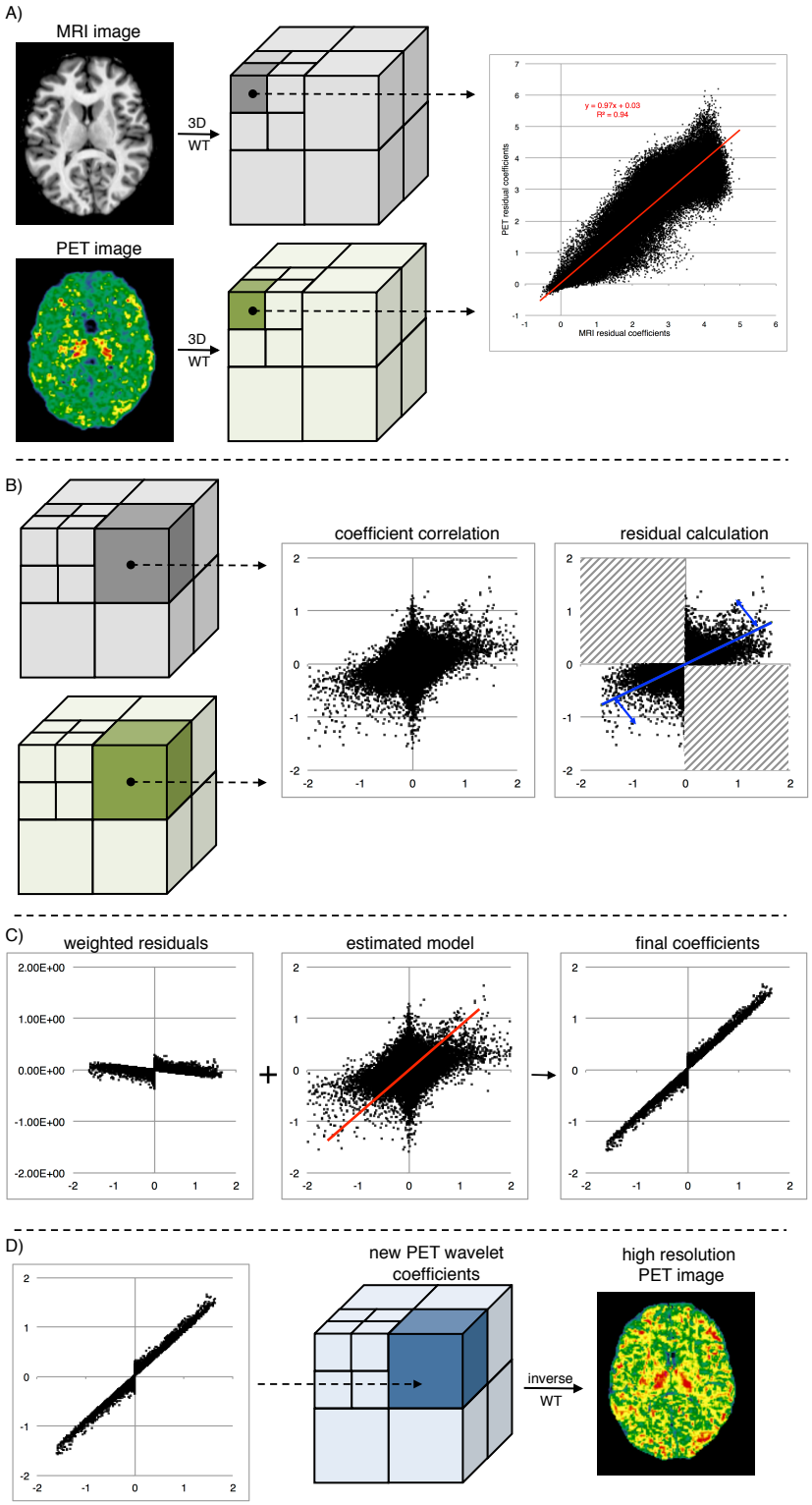

Figure 5.3: Graphical representation of the MM-RR algorithm. A) wavelet decomposition and model definition of the relationship between MR and PET signals at low resolution scales; B) model definition of the relationship between MR and PET high-resolution coefficients; C) definition of new wavelet coefficients from the models defined in A) and B) after appropriate scaling and de-noising; D) inverse wavelet transform of the final wavelet coefficients of the improved PET image

Declaration of Helsinki.

5.2.3 Positron Emission Tomography and Magnetic Resonance Imaging

All PET scans were performed on the brain dedicated PET research tomograph ECAT-HRRT (CPS Innovations, Knoxville, TN, USA). This high resolution scanner achieves an intra-slice spatial resolution of ~ 2.5 mm full width at half maximum, with 25 cm and 31.2 cm of axial and transaxial field of view [128]. The 90-minute emission scan was initiated coincident with a 1-minute intravenous bolus injection of [^{11}C]PIB (mean 358 $\pm$ 34 MBq). Images were reconstructed using the 3D ordinary Poisson ordered subset expectation maximization algorithm (POSEM) [21] implementing point spread function (PSF) modeling up to 10 iterations. An additional smoothing filter implementing the PSF was applied to the reconstructed images [111].

The resulting dynamic PET images consisted of 25 frames of data ($6 \times 1, 6 \times 2, 4 \times 3, 6 \times 5, 3 \times 10$ minutes) with a voxel size of $1.22mm \times 1.22mm \times 1.22mm$. Inter-frame subject motion correction was applied by realigning each PET frame to a common reference space through a procedure similar to those reported by Montgomery et al [79]. Data were corrected for carbon-11 decay. A reference region was determined using previously published methodology developed specifically for [^{11}C]PIB that uses a supervised clustering approach to determine a set of gray matter voxels with kinetics that are the closest to a predefined set of normative dynamics [57]. The average time-activity curve of these voxels was used as input for the Logan plot do derive parametric maps of volume of distribution (DVR)[87]. We refer to Veronese et al [125] for a detailed description of the PET [^{11}C]PIB dynamic quantification.

In addition to the PET scans, MR images of all subjects were collected using a 3T Siemens system (Siemens, Erlangen, Germany; TRIO 32-channel TIM system). Specifically, 3D T1-weighted MPRAGE, T2-weighted (T2-w) and 3d FLAIR sequences were performed for all subjects while patients had additional pre- and post- gadolinium T1 spin-echo sequences. Only the T1 weighted images were used for PVC using MM-RR. Lesions were segmented on T2-w images with reference to co-registered FLAIR

scans. For each subject, T2- and T1- weighted images were co-registered to the PET space using a rigid transformation using Flirt (http://fsl.fmrib.ox.ac.uk/fsl/) maintaining PET data in its original space and avoiding further loss of resolution due to interpolation. Using VBM8 toolbox (hhttp://dbm.neuro.uni-jena.de/vbm/download/) and FIRST (http://fsl.fmrib.ox.ac.uk/fsl/), image voxels were automatically classified as gray matter (GM), white matter (WM) and cerebrospinal fluid (CSF) using a tissue probability threshold of 90%.

Additional regions of interest (ROIs) were manually defined on patient images by a single experienced observer (BB) using the co-registered information from the T2- weighted and T1-weighted images. The ROIs were classified as follow: 1) GM; 2) normal-appearing WM; 3) perilesional WM; 4) lesion WM; 5) black holes and 6) Gadolinium enhancing (Gd+) lesions. Only lesions above 2.5 mm (corresponding to the resolution of the PET-camera) were retained as effective ROIs.

5.2.4 Image analysis and evaluation

Qualitative and quantitative evaluations were carried out comparing the original data, here labelled as Standard PET images with the output of the resolution recovery procedure, here named High Resolution PET, in order to evaluate the performance of the MM-RR algorithm. In first instance we analyzed the healthy subject images to evaluate the resolution recovery achievable with the MM-RR algorithm and any bias that may have been introduced. For each subject we calculated the average [^{11}C]PIB DVR in three ROIs (GM, WM and whole brain respectively) and the mean and standard deviation of all subjects were compared between Standard and High Resolution PET. As an additional check, we calculated the [^{11}C]PIB DVR as a function of the distance from the cerebral spinal fluid for both WM and GM ROIs as this relationship was evident in the original data as a result of PVE [125].

Finally, for a quantitative evaluation of resolution recovery, a contrast analysis was performed taking into consideration the GM/WM contrast in small spherical regions of 2.5, 5, 7.5 and 10 mm diameter. For each subject a pair of random regions was drawn on

the GM and WM segmented on the T1-weighted images. Both ROIs were then moved to the PET images (Standard and High Resolution) and the mean of voxel estimates within each region was computed (WM_{ROI},GM_{ROI}) and the mean local contrast calculated as

$$mlc_{\%} = \frac{WM_{ROI} - GM_{ROI}}{GM_{ROI}} \cdot 100 \tag{5.13}$$

The procedure was repeated up to 500 times for each sphere size and mean and variability of $mlc_{\%}$ were compared between different ROI sizes as well as between Standard and High Resolution PET.

For the patient group we compared the average [^{11}C]PIB DVR with the same statistical methodology used for the healthy subjects group focusing however on clinically relevant ROIs, specifically the normal-appearing WM, perilesional area, lesions, black holes and Gadolinium enhancing (Gd+) lesions. Additionally, we performed a correlation analysis between the average PIB DVR and the lesion volumes to check whether the effect of the PVC depended on the size of the lesion, as one would have expected. To perform this type of analysis we grouped all the lesions of all the patients according to their volumes. Then, for each lesions size, we calculated the average PIB DVR of all patients' lesions of that specific volume.

The robustness to anatomical and functional mismatch of PVC wavelet-based approaches has been already demonstrated in previous study [44]. However, an additional test was performed to ensure that no bias or artifacts are introduced when the structural and functional signals are not related. We applied the MM-RR algorithm to a sample [^{18}F]FDOPA PET/MR scan of a healthy subject where the anatomical information had no relation with the PET signal located in the basal ganglia.

5.3 Results

Figure 5.4 provides an example of the improved image resolution achieved with the MM-RR algorithm compared to Standard PET. The images refer to a representative healthy control. The High Resolution PET images show sharper contours compared to the Stan-

dard PET and better WM definition.

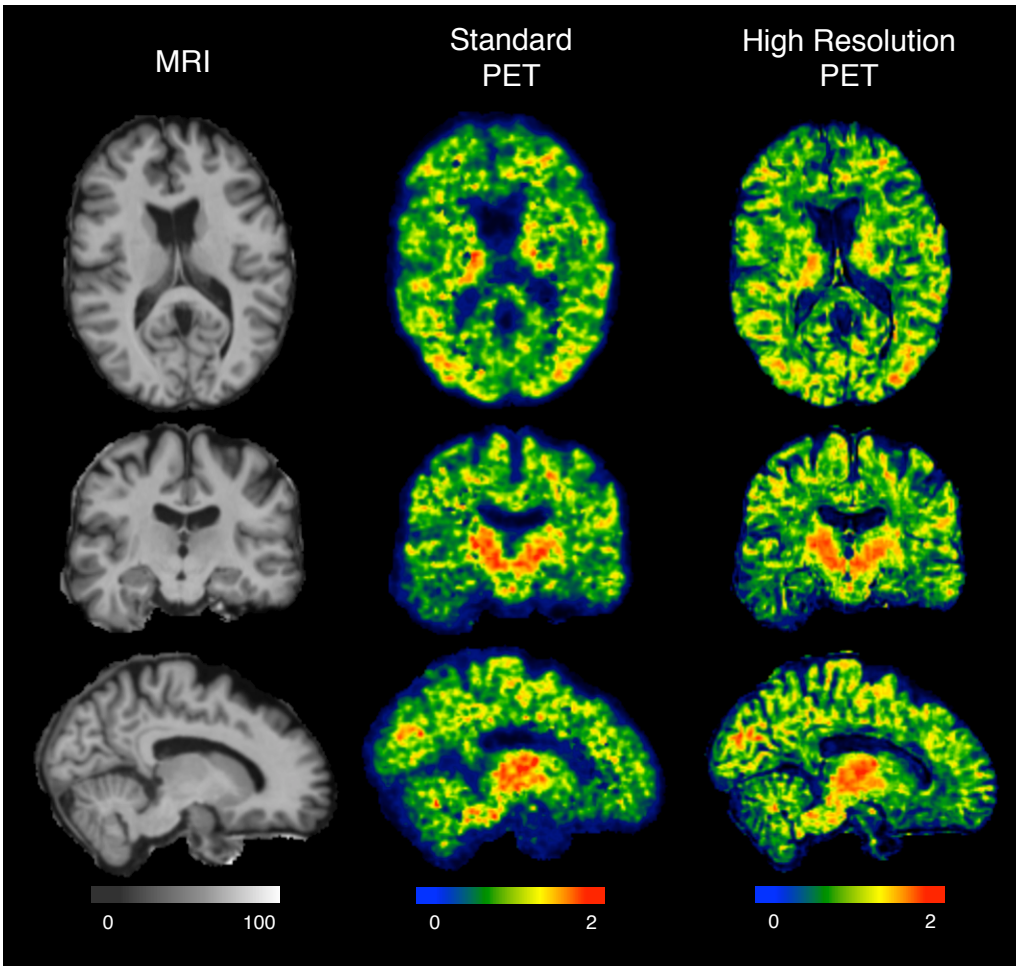

Figure 5.4: [11C]PIB PET axial, coronal and sagittal views from a representative control. Left column MRI images; central column Standard PET; right column High Resolution PET. Color codes for PET images represent DVR units dimensionless

Figure 5.5 reports the quantitative comparison of the three tissue ROIs (whole brain, gray matter and white matter) in the healthy control dataset. Each box collects the mean value for the specific ROI of all the healthy subjects. The average DVR in the WM is 5.7% higher for the High Resolution PET compared to the Standard PET. This indicates a successful partial volume correction given the specificity of PIB binding to the WM. The average DVR in the GM is comparable between Standard PET and High Resolution PET, meaning that the new algorithm does not introduce any bias. Moreover the resolution recovery does not come at the cost of increased noise as the standard deviations of the

two imaging modalities are comparable for all the three ROIs. A quantitative evaluation of the improved image quality achieved with the MM-RR algorithm is reported in the contrast analysis in Figure 5.6. High Resolution PET images show an average increase of 30% in WM/GM contrast compared to Standard PET; noteworthy is the signal improvement for the smallest ROI (2.5 mm) with a 46% increase in contrast.

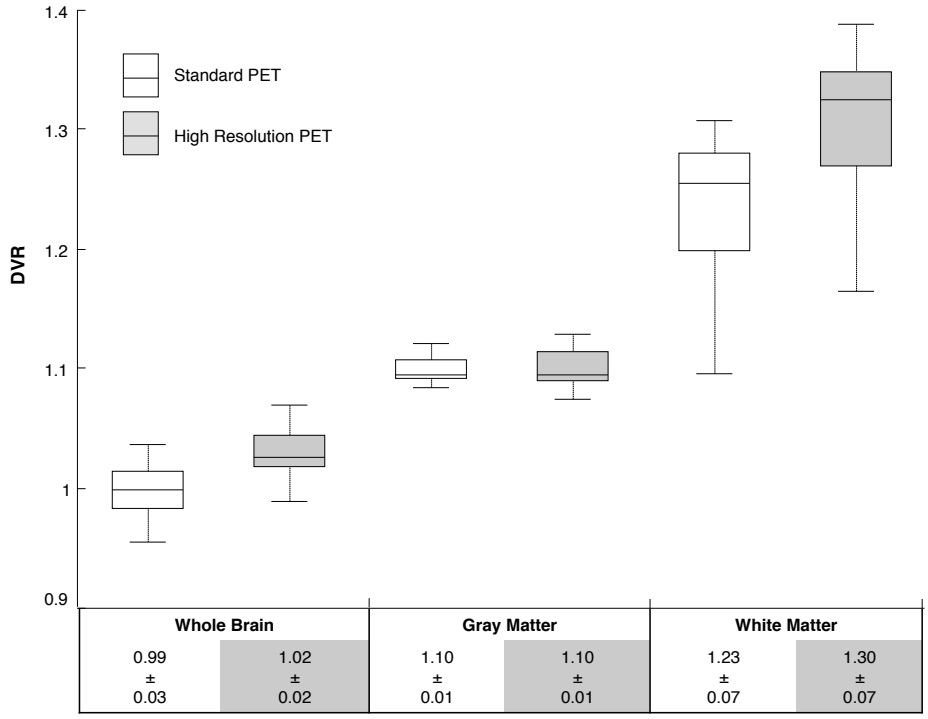

Figure 5.5: Comparison of [^{11}C]PIB DVR values between Standard PET (white boxes) and High Resolution PET (grey boxes). The box-plot diagrams show the median (middle line) and range of DVR values for the healthy control group in three different ROIs (from left to right: whole brain, grey matter, white matter). The table reports the numerical value of mean and standard deviation for each box.

A quantitative measure of the PVC that can be achieved when the resolution recovery is applied is reported in Figure 5.7 where the DVR for WM and GM is displayed as a function of the distance from the CSF. As expected the trend of the GM DVR remains comparable between Standard PET and High Resolution PET. However, for the WM, the DVR close to the CSF is considerably higher (up to 31%) for the High Resolution images while it settles on values comparable with the Standard PET as the distance increases. This suggests

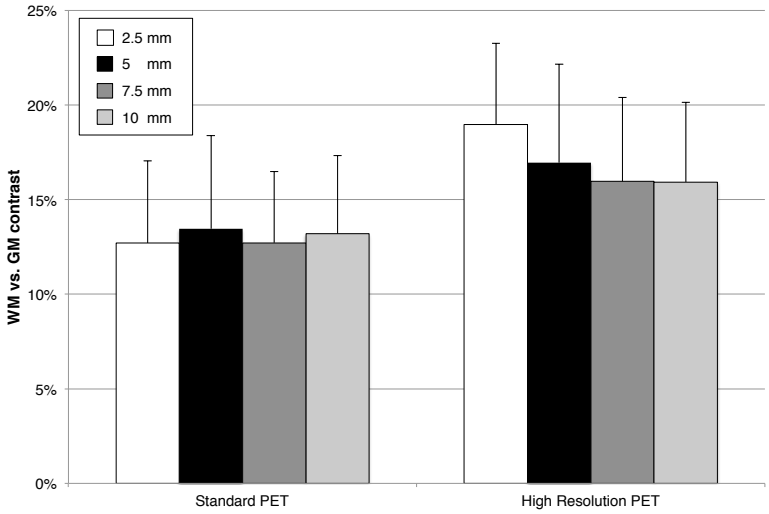

Figure 5.6: Contrast local analyses. The mean and standard deviation of white matter (WM)/grey matter (GM) contrast values are reported for Standard PET images and High Resolution PET images for different ROI sizes.

that the increase in resolution comes with an actual correction for the spill-out effect in the WM border area that is of great clinical interest given that neurodegeneration around the ventricles is an early process of the pathophysiology of MS.

Figures 5.8-5.9 report the impact of the MM-RR application to the MS patient dataset. Figure 5.8 provides an example of the improved lesion detectability achieved with the MM-RR algorithm compared to the Standard PET. The images refer to a representative MS patient. As for the healthy control in Figure 5.4, the High Resolution PET images show sharper contours compared to the Standard PET. Additionally, a noticeable improvement in lesion detectability can be appreciated in the two representative lesions (zoom in the red circle). The quantitative impact of the MM-RR application on patient images is reported in Figure 5.9. As previously done for healthy controls (Figure 5.5), each box collects the mean value for specific clinically relevant ROI for all the patients. The average PIB DVR in the lesional tissue (T2-w lesions, black holes and Gadolinium enhancing lesions) is lower for the High Resolution PET (4-12$\%$ difference); this means that the higher resolution allows PVC correction for spill-in effects. On the other hand, there is a consistent increase of the DVR in the perilesional area and normal-appearing

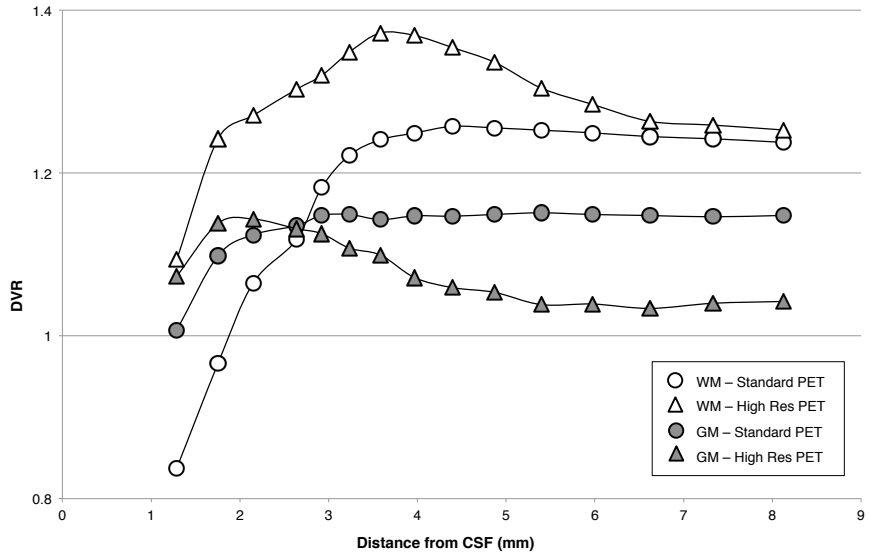

Figure 5.7: The graph reports the [^{11}C]PIB DVR values measured for white matter (white markers) and grey matter (grey markers) as function of the distance from the cerebral spinal fluid (CSF). Lines with circle markers refer to the Standard PET and the lines with triangle markers refer to the High Resolution PET.

WM up to 5% meaning that lesions had better contrast and this led to better segmentation and quantification. As for the analysis of the healthy control dataset, the standard deviation of the two imaging modalities is comparable for all the ROIs.

Finally, Figure 5.10 shows the comparison between Standard PET and High Resolution PET when analyzing the variation of PIB DVR against the lesion size. As expected, recovery is greater for small lesions while for big lesion the two modalities produce very similar DVRs

It is worth to highlight the robustness of the methodology regarding possible mismatch between PET and MRI images. In Figure 5.11 we report the result of the application of the algorithm application to a [^{18}F]FDOPA PET and T1-weigthed MR templates of healthy subjects (www.nitrc.org/projects/spmtemplates/) were one can note that no artifacts are introduced after application of MM-RR.

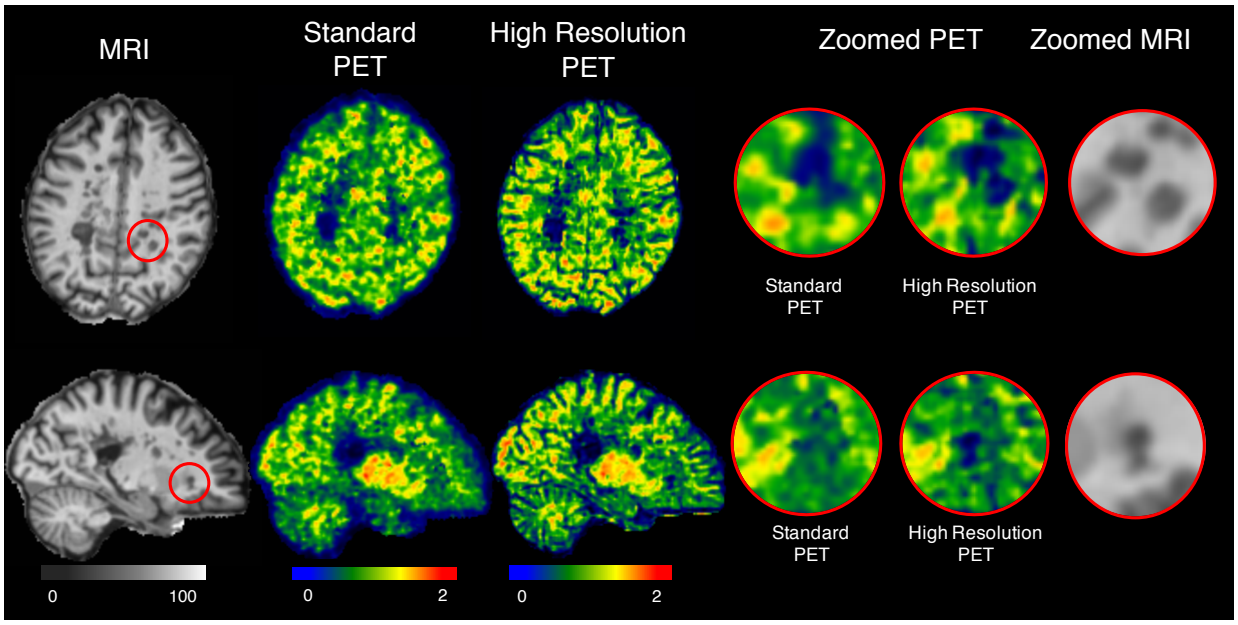

Figure 5.8: Axial and sagittal views from a representative MS patient. From left to right: MRI images; Standard PET; High Resolution PET; zooms of the area delimited in the MRI image with a red circle.

5.4 Discussion

In this work, we evaluated the influence of a novel multimodal PVC technique on the quantification of myelin content in healthy control and MS patients. Similar PVC techniques based on wavelet decomposition, have already been extensively validated for brain [104, 74, 59, 105] and whole body PET/CT [44] using either simulated or phantom data.

In this work the methodology has been developed to give a mathematical account of the better specificity to myelin and quantitative robustness of PET at low resolution as well as the good precision of MRI at finer resolution scales. Given the nature of PET/MR myelin images and considering that [^{11}C]PIB PET is a new modality for patient *in-vivo* imaging, realistic data simulations for additional algorithm validation were not feasible to perform. However, the robustness of the algorithm towards possible artefacts due to functional-structural mismatch between anatomical and functional images has been tested using [^{18}F]FDOPA PET/MR images from healthy subjects. This type of data does not show cor-

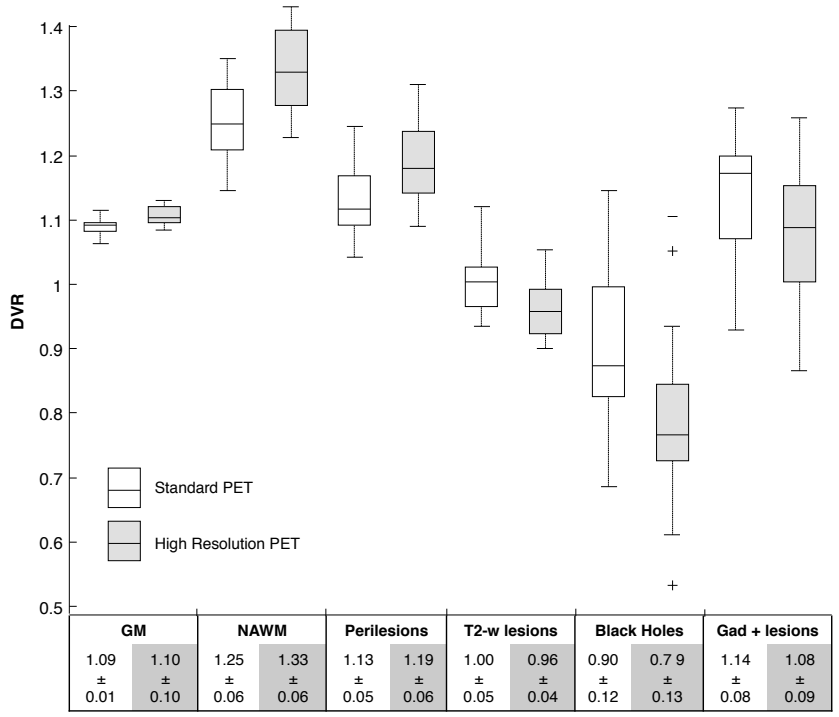

GM		NAWM		Perilesions		T2-w lesions		Black Holes		Gad + lesions	
1.09 ± 0.01	1.10 ± 0.10	1.25 ± 0.06	1.33 ± 0.06	1.13 ± 0.05	1.19 ± 0.06	1.00 ± 0.05	0.96 ± 0.04	0.90 ± 0.12	0.7 9 ± 0.13	1.14 ± 0.08	1.08 ± 0.09

Figure 5.9: Comparison of [^{11}C]PIB DVR values between Standard PET (white boxes) and High Resolution PET (grey boxes). The box-plot diagrams show the median (middle line) and range of DVR for the healthy control group in three different ROIs (from left to right: grey matter GM, normal-appearing white matter NAWM, Perilesions, T2-w lesions, Black Holes, Gad enhancing lesions). The table reports the numerical value of mean and standard deviation for each box.

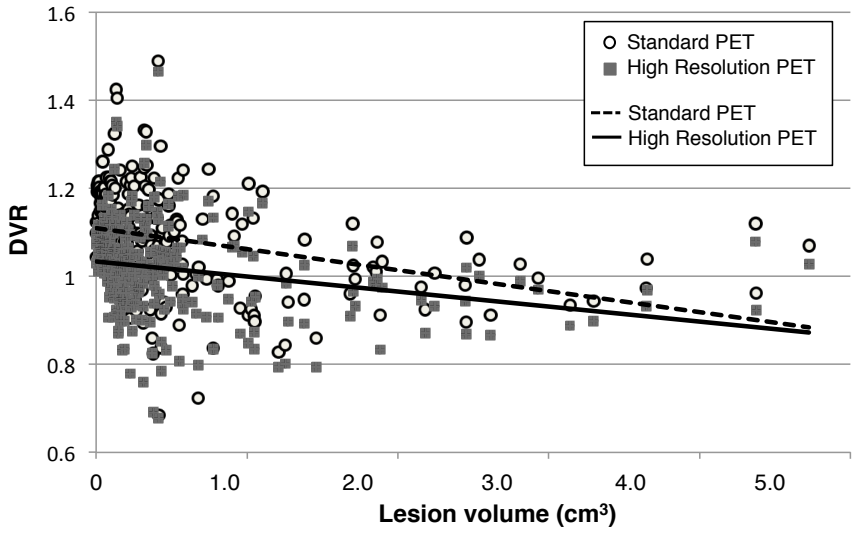

Figure 5.10: Comparison of [^{11}C]PIB DVR lesion quantification between Standard PET and High Resolution PET as function of lesion size. Each mark (white circle for Standard PET and grey square for High Resolution PET) represents the average DVR for lesion with a specific volume. The two lines represent the regression model of the data (dashed line for Standard PET and solid line for High Resolution PET)

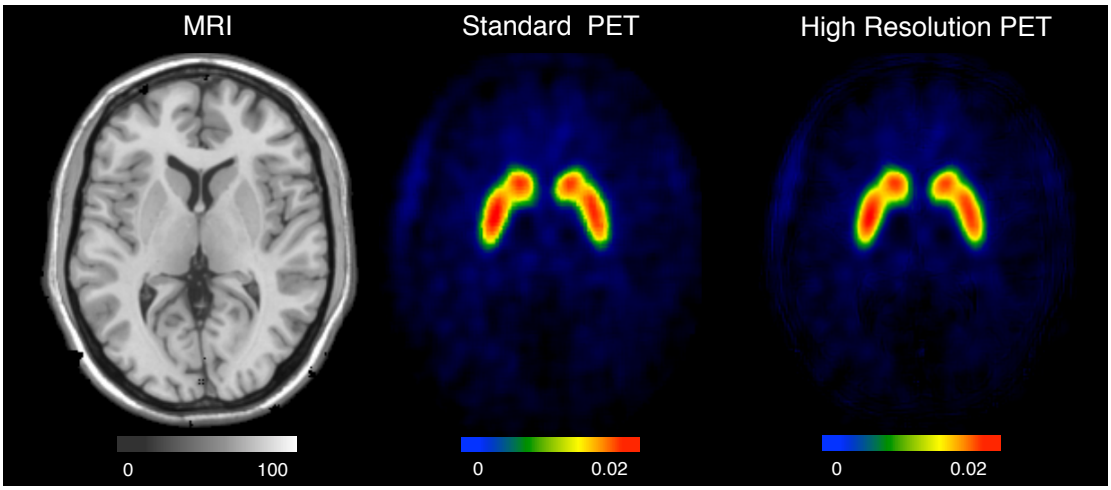

Figure 5.11: Axial view from a representative control subject of a [^{18}F]FDOPA PET/MR dataset. Left column MRI image; central column Standard PET; right column High Resolution PET

relation in the basal ganglia between functional and structural images, hence one would not expect significant changes in the final PET images as our analysis demonstrates. It is worth highlighting that our algorithm aims to tackle a specific clinical application where the PVE affects the quantification of cold lesions that can not be defined *a priori* on population atlases. The wavelet-based techniques that we had previously described use a loose statistical model to test the existence of quantitative relationship between the structural (MRI) and the functional data (PET) and then apply the scaling if the relationship exists. Moreover, in brain imaging, these methods rely on population atlases to stabilize the model. In the work presented here the assumption is that both PET and MRI are myelin sensitive but that the sensitivity varies at different scales. The resulting linear model is then quite stable and provides good recovery for the cold lesions that, importantly, are the characteristic hallmark of MS pathology.

Our results on the healthy control dataset showed a qualitative improvement especially in the delineation of WM structures and an average 30% increase in contrast between white and grey matter with no quantification bias or noise increase. The signal recovery and good noise control assessed in the healthy controls were then reflected into patient images that demonstrated lesions with sharper and better-defined contours and the resulting accurate quantification of PIB DVR in different lesion types and perilesional areas. The work presented here we believe is highly relevant for the newly introduced PET-MRI scanners as it presents one of the first synergistic approaches combining PET and MRI data for the same target, myelin in this case. In this work the MRI data are provided as a T1-weighted scan that is not the most specific to myelin content. In the future we plan to test this methodology using more myelin-sensitive imaging sequences such as Magnetization Transfer Imaging (MTR) [34, 124] and multi-component driven equilibrium single pulse observation of T1 (mcDESPOT) [62, 64]. Both MRI sequences offer better contrast of tissue water content, especially the latter given its capability to provide a measure of myelin thickness strongly related to the functional signal provided by the [11C]PIB PET.

5.5 Conclusion

We have developed a robust multimodal methodology for quantitative resolution recovery of brain [^{11}C]PIB PET/MR scans, here specifically designed for myelin imaging, and tested it on a set of clinical healthy controls and MS patients data. The technique produces images with significantly improved quantitative properties and visual quality and it is of straightforward and rapid application without need of atlas incorporation or anatomical segmentation.

Chapter 6

Conclusions

Multimodality imaging systems like PET/CT and PET/MRI have great potential as diagnostic tools since they combine the high resolution anatomical details of CT and MRI with the functional information provided by PET imaging. However, the combination of the two modalities has been mostly limited to overlapping images for visualization purposes while ad-hoc tools to fully exploit the synergy between anatomical and functional images are still inadequate. A clever idea already investigated in the literature is to take advantage of multimodality imaging systems and to use the detailed high resolution anatomical content to improve the low resolution of PET images in order to perform partial volume correction (PVC) and achieve better functional quantification. It is in this context of PET PVC that the work presented in this thesis found a purpose. This work aimed to tackle two distinctive clinical applications, one in PET/CT and the second in PET/MR imaging, in order to improve their diagnostic power by means of performing PVC on PET images. In the first part an existing PVC technique has been optimised for accurate and straightforward application in oncology whole body PET/CT imaging of bone metastases. In the second part a step forward has been made by developing a new and more robust PVC algorithm for brain PET/MR myelin imaging in multiple sclerosis.

The two algorithms performed PVC through a resolution recovery of PET images by taking advantage of the mutliresolution property of the wavelet transform applied to both functional and structural images. The choice of the specific wavelet decomposition has

been supported by previous application in PET imaging and a detailed description of this mathematical tool is presented in the thesis appendix. Realistic PET/CT phantom acquisitions were also performed to achieve a more robust method validation, aiming to fill the existing gap between sometimes simplistic whole body data simulation and real patient data which lacks ground truth. These acquisitions, first of their kind, have been thoroughly described to be easily reproduced for other applications.

The main result of this work is that application of both the PVC algorithms resulted in a very significant gain in PET image resolution without any detectable increase of image noise. Lesion sharpness and detectability improved as well with a resulting increase in quantification accuracy, which has been tested using phantom or control data as well as compared against an additional resolution recovery technique (i.e. point spread function PSF reconstruction). Together with the remarkable results in terms of image quality and functional quantification, the algorithms presented proved to be robust toward possible mismatch between anatomical and functional images and, furthermore, they do not require prior image elaboration or atlas creation.

For the reasons stated above, the algorithms developed and presented in this thesis proved to be straightforward tools to employ multimodality imaging to improve PET quantification in routine clinical practice.

6.1 Future Directions

The work presented in this thesis can be easily extended towards different directions. For what concern the whole-body bone metastases PET/CT application, of interest would be to evaluate the effect of the PVC on a longitudinal study. Images at different time points are required to evaluate whether high resolution images might be of help in identifying early change in lesion activity thus patient response to therapy. Furthermore, texture analysis is gaining popularity in characterizing lesional bone. Another interesting development would then be to evaluate the effect of PVC in lesion classification through texture analysis.

The evaluation of the second PVC technique has been based on clinical data only. For

this reason an immediate future step would be to fully validate this approach with simulated data as well. However, given the interesting results obtained in the Phantom Experiment presented in this thesis, the set-up and acquisition of structural-functional PET/MRI phantom images would be an interesting piece of work, especially when considering the increasing popularity of simultaneous PET/MRI system.

From a clinical perspective it would be of interest to test the MM-RR technique with MRI sequences more myelin-specific than the T1w. As mentioned earlier in the conclusion, a recent study on myelin imaging demonstrated the specificity of MTR and mcDEPOST sequences to myelin content. In this way the structural image will carry functional information as well as creating a more interesting scenario.

Considering the flexibility toward the input structural image required (no segmentation and no atlas needed) the use of MM-RR could be extended in other fields where a lower resolution image could take advantage from a higher resolution counterpart. One example that might be worth mentioning is applying the algorithm to raw DTI data using the T1 as structural information to obtain final high resolution DTI images.

References

[1] P. Aguiar, M. Rafecas, J. E. Ortuño, G. Kontaxakis, A. Santos, J. Pavía, and D. Ros. Geometrical and monte carlo projectors in 3d pet reconstruction. *Medical physics*, 37(11):5691–5702, 2010.

[2] A. Aldroubi and M. Unser. *Wavelets in medicine and biology*. CRC press, 1996.

[3] A. M. Alessio, C. W. Stearns, S. Tong, S. G. Ross, S. Kohlmyer, A. Ganin, and P. E. Kinahan. Application and evaluation of a measured spatially variant system model for pet image reconstruction. *Medical Imaging, IEEE Transactions on*, 29(3):938–949, 2010.

[4] B. A. Ardekani, M. Braun, B. F. Hutton, I. Kanno, and H. Iida. Minimum cross-entropy reconstruction of pet images using prior anatomical information. *Physics in Medicine and Biology*, 41(11):2497, 1996.

[5] J. A. Aston, V. J. Cunningham, M.-C. Asselin, A. Hammers, A. C. Evans, and R. N. Gunn. Positron emission tomography partial volume correction: Estimation and algorithms. *Journal of Cerebral Blood Flow & Metabolism*, 22(8):1019–1034, 2002.

[6] K. Baete, J. Nuyts, K. Van Laere, W. Van Paesschen, S. Ceyssens, L. De Ceuninck, O. Gheysens, A. Kelles, J. Van den Eynden, P. Suetens, et al. Evaluation of anatomy based reconstruction for partial volume correction in brain fdg-pet. *Neuroimage*, 23(1):305–317, 2004.

[7] D. L. Barbee, R. T. Flynn, J. E. Holden, R. J. Nickles, and R. Jeraj. A method for partial volume correction of pet-imaged tumor heterogeneity using expectation

maximization with a spatially varying point spread function. *Physics in medicine and biology*, 55(1):221, 2009.

[8] G. Battle. A block spin construction of ondelettes. part i: Lemarié functions. *Communications in Mathematical Physics*, 110(4):601–615, 1987.

[9] M. Beheshti, R. Vali, P. Waldenberger, F. Fitz, M. Nader, J. Hammer, W. Loidl, C. Pirich, I. Fogelman, and W. Langsteger. The use of f-18 choline pet in the assessment of bone metastases in prostate cancer: correlation with morphological changes on ct. *Molecular imaging and biology*, 11(6):446–454, 2009.

[10] B. Benedetta, M. Veronese, D. Garca-Lorenzo, M. Battaglini, E. Poirion, A. Chardain, L. Freeman, C. Louapre, M. Tchikviladze, C. Papeix, F. Doll, B. Zalc, C. Lubetzki, M. Bottlaender, F. Turkheimer, and B. Stankoff. Dynamic imaging of individual remyelination profiles in multiple sclerosis. *Annals of neurology*, In press.

[11] V. Bettinardi, I. Castiglioni, E. De Bernardi, and M. Gilardi. Pet quantification: strategies for partial volume correction. *Clinical and Translational Imaging*, 2(3):199–218, 2014.

[12] J. Bini, M. Eldib, P. M. Robson, and Z. A. Fayad. Wavelet-based partial volume effect correction for simultaneous mr/pet of the carotid arteries. *EJNMMI Physics*, 1(1):1–2, 2014.

[13] R. Boellaard, W. J. Oyen, C. J. Hoekstra, O. S. Hoekstra, E. P. Visser, A. T. Willemsen, B. Arends, F. J. Verzijlbergen, J. Zijlstra, A. M. Paans, et al. The netherlands protocol for standardisation and quantification of fdg whole body pet studies in multi-centre trials. *European journal of nuclear medicine and molecular imaging*, 35(12):2320–2333, 2008.

[14] A. Bousse, S. Pedemonte, B. A. Thomas, K. Erlandsson, S. Ourselin, S. Arridge, and B. F. Hutton. Markov random field and gaussian mixture for segmented mri-based partial volume correction in pet. *Physics in medicine and biology*, 57(20):6681, 2012.

[15] N. Boussion, M. Hatt, F. Lamare, Y. Bizais, A. Turzo, C. Cheze-Le Rest, and D. Visvikis. A multiresolution image based approach for correction of partial volume effects in emission tomography. *Physics in medicine and biology*, 51(7):1857, 2006.

[16] N. Boussion, M. Hatt, F. Lamare, C. C. Le Rest, and D. Visvikis. Contrast enhancement in emission tomography by way of synergistic pet/ct image combination. *Computer methods and programs in biomedicine*, 90(3):191–201, 2008.

[17] N. Boussion, C. C. Le Rest, M. Hatt, and D. Visvikis. Incorporation of wavelet-based denoising in iterative deconvolution for partial volume correction in whole-body pet imaging. *European journal of nuclear medicine and molecular imaging*, 36(7):1064–1075, 2009.

[18] J. E. Bowsher, V. E. Johnson, T. G. Turkington, R. J. Jaszczak, C. E. Floyd, and R. E. Coleman. Bayesian reconstruction and use of anatomical a priori information for emission tomography. *Medical Imaging, IEEE Transactions on*, 15(5):673–686, 1996.

[19] C. S. Burrus, R. A. Gopinath, and H. Guo. *Introduction to wavelets and wavelet transforms*, volume 998. Prentice hall New Jersey, 1998.

[20] R. E. Carson. A maximum likelihood method for region-of-interest evaluation in emission tomography. *Journal of computer assisted tomography*, 10(4):654–663, 1986.

[21] R. E. Carson, W. C. Barker, J.-S. Liow, C. Johnson, et al. Design of a motion-compensation osem list-mode algorithm for resolution-recovery reconstruction for the hrrt. In *Nuclear Science Symposium Conference Record, 2003 IEEE*, volume 5, pages 3281–3285. IEEE, 2003.

[22] C. Chan, R. Fulton, R. Barnett, D. D. Feng, and S. Meikle. Postreconstruction non-local means filtering of whole-body pet with an anatomical prior. *Medical Imaging, IEEE Transactions on*, 33(3):636–650, 2014.

[23] S. G. Chang, B. Yu, and M. Vetterli. Adaptive wavelet thresholding for image denoising and compression. *IEEE transactions on image processing*, 9(9):1532–1546, 2000.

[24] C. K. Chui and C. S. Liu. *Wavelet toolware*. Gulf Professional Publishing, 1998.

[25] A. Clamp, S. Danson, H. Nguyen, D. Cole, and M. Clemons. Assessment of therapeutic response in patients with metastatic bone disease. *The lancet oncology*, 5(10):607–616, 2004.

[26] R. Coleman, G. Mashiter, K. Whitaker, D. Moss, R. Rubens, and I. Fogelman. Bone scan flare predicts successful systemic therapy for bone metastases. *J Nucl Med*, 29(8):1354–1359, 1988.

[27] R. Coleman and R. Rubens. The clinical course of bone metastases from breast cancer. *British journal of cancer*, 55(1):61, 1987.

[28] C. Comtat, P. E. Kinahan, J. A. Fessler, T. Beyer, D. W. Townsend, M. Defrise, and C. Michel. Clinically feasible reconstruction of 3d whole-body pet/ct data using blurred anatomical labels. *Physics in Medicine and Biology*, 47(1):1, 2002.

[29] C. Comtat, F. Sureau, M. Sibomana, I. Hong, N. Sjoholm, and R. Trebossen. Image based resolution modeling for the hrrt osem reconstructions software. In *2008 IEEE Nuclear Science Symposium Conference Record*, pages 4120–4123. IEEE, 2008.

[30] G. J. Cook, C. Yip, M. Siddique, V. Goh, S. Chicklore, A. Roy, P. Marsden, S. Ahmad, and D. Landau. Are pretreatment 18f-fdg pet tumor textural features in non–small cell lung cancer associated with response and survival after chemoradiotherapy? *Journal of Nuclear Medicine*, 54(1):19–26, 2013.

[31] I. Daubechies et al. *Ten lectures on wavelets*, volume 61. SIAM, 1992.

[32] A. P. Dempster, N. M. Laird, and D. B. Rubin. Maximum likelihood from incomplete data via the em algorithm. *Journal of the royal statistical society. Series B (methodological)*, pages 1–38, 1977.

[33] D. L. Donoho, I. M. Johnstone, G. Kerkyacharian, and D. Picard. Wavelet shrinkage: asymptopia? *Journal of the Royal Statistical Society. Series B (Methodological)*, pages 301–369, 1995.

[34] V. Dousset, R. Grossman, K. Ramer, M. Schnall, L. Young, F. Gonzalez-Scarano, E. Lavi, and J. Cohen. Experimental allergic encephalomyelitis and multiple sclerosis: lesion characterization with magnetization transfer imaging. *Radiology*, 182(2):483–491, 1992.

[35] E. Even-Sapir, U. Metser, G. Flusser, L. Zuriel, Y. Kollender, H. Lerman, G. Lievshitz, I. Ron, and E. Mishani. Assessment of malignant skeletal disease: initial experience with 18f-fluoride pet/ct and comparison between 18f-fluoride pet and 18f-fluoride pet/ct. *Journal of Nuclear Medicine*, 45(2):272–278, 2004.

[36] E. Even-Sapir, U. Metser, E. Mishani, G. Lievshitz, H. Lerman, and I. Leibovitch. The detection of bone metastases in patients with high-risk prostate cancer: 99mtc-mdp planar bone scintigraphy, single-and multi-field-of-view spect, 18f-fluoride pet, and 18f-fluoride pet/ct. *Journal of Nuclear Medicine*, 47(2):287–297, 2006.

[37] P. P. Fatouros and A. Marmarou. Use of magnetic resonance imaging for in vivo measurements of water content in human brain: method and normal values. *Journal of neurosurgery*, 90(1):109–115, 1999.

[38] J. A. Fessler. Penalized weighted least-squares image reconstruction for positron emission tomography. *IEEE Transactions on Medical Imaging*, 13(2):290–300, 1994.

[39] A. R. Formiconi. Least squares algorithm for region-of-interest evaluation in emission tomography. *IEEE transactions on medical imaging*, 12(1):90–100, 1993.

[40] R. J. Franklin and V. Gallo. The translational biology of remyelination: Past, present, and future. *Glia*, 62(11):1905–1915, 2014.

[41] T. Funck, C. Paquette, A. Evans, and A. Thiel. Surface-based partial-volume correction for high-resolution pet. *NeuroImage*, 102:674–687, 2014.

[42] C. Galasko. The pathological basis for skeletal scintigraphy. *Journal of Bone & Joint Surgery, British Volume*, 57(3):353–359, 1975.

[43] E. González, J.-y. Cui, G. Pratx, M. Bieniosek, P. D. Olcott, and C. S. Levin. Point spread function for pet detectors based on the probability density function of the line segment. In *Nuclear Science Symposium and Medical Imaging Conference (NSS/MIC), 2011 IEEE*, pages 4386–4389. IEEE, 2011.

[44] E. Grecchi, J. ODoherty, M. Veronese, C. Tsoumpas, G. J. Cook, and F. E. Turkheimer. Multimodal partial-volume correction: Application to 18f-fluoride pet/ct bone metastases studies. *Journal of Nuclear Medicine*, 56(9):1408–1414, 2015.

[45] P. J. Green. Bayesian reconstructions from emission tomography data using a modified em algorithm. *Medical Imaging, IEEE Transactions on*, 9(1):84–93, 1990.

[46] A. Hammers, R. Allom, M. J. Koepp, S. L. Free, R. Myers, L. Lemieux, T. N. Mitchell, D. J. Brooks, and J. S. Duncan. Three-dimensional maximum probability atlas of the human brain, with particular reference to the temporal lobe. *Human brain mapping*, 19(4):224–247, 2003.

[47] M. Hatt, D. Groheux, A. Martineau, M. Espié, E. Hindié, S. Giacchetti, A. De Roquancourt, D. Visvikis, and C. Cheze-Le Rest. Comparison between 18f-fdg pet image–derived indices for early prediction of response to neoadjuvant chemotherapy in breast cancer. *Journal of Nuclear Medicine*, 54(3):341–349, 2013.

[48] M. Hatt, A. Le Pogam, D. Visvikis, O. Pradier, and C. C. Le Rest. Impact of partial-volume effect correction on the predictive and prognostic value of baseline 18f-fdg pet images in esophageal cancer. *Journal of Nuclear Medicine*, 53(1):12–20, 2012.

[49] M. Hatt, M. Majdoub, M. Vallieres, F. Tixier, C. C. Le Rest, D. Groheux, E. Hindié, A. Martineau, O. Pradier, R. Hustinx, et al. 18f-fdg pet uptake characterization through texture analysis: Investigating the complementary nature of heterogeneity and functional tumor volume in a multi–cancer site patient cohort. *Journal of Nuclear Medicine*, 56(1):38–44, 2015.

[50] T. Hebert and R. Leahy. A generalized em algorithm for 3-d bayesian reconstruction from poisson data using gibbs priors. *IEEE transactions on medical imaging*, 8(2):194–202, 1989.

[51] G. T. Herman. *Fundamentals of computerized tomography: image reconstruction from projections*. Springer Science & Business Media, 2009.

[52] N. J. Hoetjes, F. H. van Velden, O. S. Hoekstra, C. J. Hoekstra, N. C. Krak, A. A. Lammertsma, and R. Boellaard. Partial volume correction strategies for quantitative fdg pet in oncology. *European journal of nuclear medicine and molecular imaging*, 37(9):1679–1687, 2010.

[53] H. M. Hudson and R. S. Larkin. Accelerated image reconstruction using ordered subsets of projection data. *Medical Imaging, IEEE Transactions on*, 13(4):601–609, 1994.

[54] R. H. Huesman. A new fast algorithm for the evaluation of regions of interest and statistical uncertainty in computed tomography. *Physics in Medicine and Biology*, 29(5):543, 1984.

[55] B. F. Hutton. Recent advances in iterative reconstruction for clinical spect/pet and ct. *Acta Oncologica*, 50(6):851–858, 2011.

[56] B. F. Hutton, B. A. Thomas, K. Erlandsson, A. Bousse, A. Reilhac-Laborde, D. Kazantsev, S. Pedemonte, K. Vunckx, S. Arridge, and S. Ourselin. What approach to brain partial volume correction is best for pet/mri? *Nuclear Instruments and Methods in Physics Research Section A: Accelerators, Spectrometers, Detectors and Associated Equipment*, 702:29–33, 2013.

[57] Y. Ikoma, P. Edison, A. Ramlackhansingh, D. J. Brooks, and F. E. Turkheimer. Reference region automatic extraction in dynamic [11c] pib. *Journal of Cerebral Blood Flow & Metabolism*, 33(11):1725–1731, 2013.

[58] D. Kazantsev, S. Ourselin, B. F. Hutton, K. J. Dobson, A. P. Kaestner, W. R. Lionheart, P. J. Withers, P. D. Lee, and S. R. Arridge. A novel technique to incorporate

structural prior information into multi-modal tomographic reconstruction. *Inverse Problems*, 30(6):065004, 2014.

[59] E. Kim, M. Shidahara, C. Tsoumpas, C. J. McGinnity, J. S. Kwon, O. D. Howes, and F. E. Turkheimer. Partial volume correction using structural–functional synergistic resolution recovery: comparison with geometric transfer matrix method. *Journal of Cerebral Blood Flow & Metabolism*, 33(6):914–920, 2013.

[60] N. Kingsbury. Complex wavelets for shift invariant analysis and filtering of signals. *Applied and computational harmonic analysis*, 10(3):234–253, 2001.

[61] N. G. Kingsbury. The dual-tree complex wavelet transform: a new technique for shift invariance and directional filters. In *IEEE Digital Signal Processing Workshop*, volume 86, pages 120–131. Citeseer, 1998.

[62] A. Kirov, J. Piao, and C. Schmidtlein. Partial volume effect correction in pet using regularized iterative deconvolution with variance control based on local topology. *Physics in medicine and biology*, 53(10):2577, 2008.

[63] H. H. Kitzler, J. Su, M. Zeineh, C. Harper-Little, A. Leung, M. Kremenchutzky, S. C. Deoni, and B. K. Rutt. Deficient mwf mapping in multiple sclerosis using 3d whole-brain multi-component relaxation mri. *Neuroimage*, 59(3):2670–2677, 2012.

[64] W. E. Klunk, H. Engler, A. Nordberg, Y. Wang, G. Blomqvist, D. P. Holt, M. Bergström, I. Savitcheva, G.-F. Huang, S. Estrada, et al. Imaging brain amyloid in alzheimer's disease with pittsburgh compound-b. *Annals of neurology*, 55(3):306–319, 2004.

[65] S. H. Kolind and S. C. Deoni. Rapid three-dimensional multicomponent relaxation imaging of the cervical spinal cord. *Magnetic Resonance in Medicine*, 65(2):551–556, 2011.

[66] F. A. Kotasidis, G. I. Angelis, J. C. Matthews, W. R. Lionheart, and A. J. Reader. Space variant psf parameterization in image space using printed point source ar-

rays on the hirez pet/ct. In *2010 IEEE International Conference on Imaging Systems and Techniques*, pages 129–134. IEEE, 2010.

[67] H. Kudo, M. Nomura, T. Asada, and T. Takeda. Image processing method for analyzing cerebral blood-flow using spect and mri. In *Nuclear Science Symposium Conference Record, 2007. NSS'07. IEEE*, volume 5, pages 4015–4021. IEEE, 2007.

[68] K. Lange, R. Carson, et al. Em reconstruction algorithms for emission and transmission tomography. *J Comput Assist Tomogr*, 8(2):306–16, 1984.

[69] C. Laule, I. Vavasour, S. Kolind, D. Li, T. Traboulsee, G. Moore, et al. Magnetic resonance imaging of myelin. neurotherapeutics: the journal of the american society for experimental neurotherapeutics 4 (3), 460–84, 2007.

[70] A. Le Pogam, M. Hatt, P. Descourt, N. Boussion, C. Tsoumpas, F. E. Turkheimer, C. Prunier-Aesch, J.-L. Baulieu, D. Guilloteau, and D. Visvikis. Evaluation of a 3d local multiresolution algorithm for the correction of partial volume effects in positron emission tomography. *Medical physics*, 38(9):4920–4933, 2011.

[71] C. S. Levin and E. J. Hoffman. Calculation of positron range and its effect on the fundamental limit of positron emission tomography system spatial resolution. *Physics in medicine and biology*, 44(3):781, 1999.

[72] B. Lipinski, H. Herzog, E. R. Kops, W. Oberschelp, and H.-W. Müller-Gärtner. Expectation maximization reconstruction of positron emission tomography images using anatomical magnetic resonance information. *Medical Imaging, IEEE Transactions on*, 16(2):129–136, 1997.

[73] S. Mallat. *A wavelet tour of signal processing*. Academic press, 1999.

[74] S. G. Mallat. A theory for multiresolution signal decomposition: the wavelet representation. *Pattern Analysis and Machine Intelligence, IEEE Transactions on*, 11(7):674–693, 1989.

[75] O. Mawlawi, D. A. Podoloff, S. Kohlmyer, J. J. Williams, C. W. Stearns, R. F. Culp, and H. Macapinlac. Performance characteristics of a newly developed pet/ct scanner using nema standards in 2d and 3d modes. *Journal of Nuclear Medicine*, 45(10):1734–1742, 2004.

[76] C. J. McGinnity, M. Shidahara, M. Feldmann, S. Keihaninejad, D. A. R. Barros, I. S. Gousias, J. S. Duncan, D. J. Brooks, R. A. Heckemann, F. E. Turkheimer, et al. Quantification of opioid receptor availability following spontaneous epileptic seizures: Correction of [11 c] diprenorphine pet data for the partial-volume effect. *NeuroImage*, 79:72–80, 2013.

[77] S. R. Meikle, B. F. Hutton, D. L. Bailey, P. K. Hooper, and M. J. Fulham. Accelerated em reconstruction in total-body pet: potential for improving tumour detectability. *Physics in medicine and biology*, 39(10):1689, 1994.

[78] C. C. Meltzer, J. P. Leal, H. S. Mayberg, H. N. Wagner Jr, and J. J. Frost. Correction of pet data for partial volume effects in human cerebral cortex by mr imaging. *Journal of computer assisted tomography*, 14(4):561–570, 1990.

[79] C. C. Meltzer, J. K. Zubieta, J. M. Links, P. Brakeman, M. J. Stumpf, and J. J. Frost. Mr-based correction of brain pet measurements for heterogeneous gray matter radioactivity distribution. *Journal of Cerebral Blood Flow & Metabolism*, 16(4):650–658, 1996.

[80] R. Molteni. Prospects and challenges of rendering tissue density in hounsfield units for cone beam computed tomography. *Oral surgery, oral medicine, oral pathology and oral radiology*, 116(1):105–119, 2013.

[81] A. J. Montgomery, K. Thielemans, M. A. Mehta, F. Turkheimer, S. Mustafovic, and P. M. Grasby. Correction of head movement on pet studies: comparison of methods. *Journal of Nuclear Medicine*, 47(12):1936–1944, 2006.

[82] S. C. Moore, S. Southekal, M.-A. Park, S. J. McQuaid, M. F. Kijewski, and S. P. Muller. Improved regional activity quantitation in nuclear medicine using a new ap-

proach to correct for tissue partial volume and spillover effects. *IEEE transactions on medical imaging*, 31(2):405–416, 2012.

[83] P. Morell, R. Quarles, and W. Norton. Formation, structure, and biochemistry of myelin. In *Basic neurochemistry*, pages 109–136. Raven Press New York, 1989.

[84] H. W. Müller-Gärtner, J. M. Links, J. L. Prince, R. N. Bryan, E. McVeigh, J. P. Leal, C. Davatzikos, and J. J. Frost. Measurement of radiotracer concentration in brain gray matter using positron emission tomography: Mri-based correction for partial volume effects. *Journal of Cerebral Blood Flow & Metabolism*, 12(4):571–583, 1992.

[85] Y. Nakamoto, B. B. Chin, D. L. Kraitchman, L. P. Lawler, L. T. Marshall, and R. L. Wahl. Effects of nonionic intravenous contrast agents at pet/ct imaging: Phantom and canine studies 1. *Radiology*, 227(3):817–824, 2003.

[86] J. Nuyts. The use of mutual information and joint entropy for anatomical priors in emission tomography. In *Nuclear Science Symposium Conference Record, 2007. NSS'07. IEEE*, volume 6, pages 4149–4154. IEEE, 2007.

[87] V. Y. Panin, F. Kehren, C. Michel, and M. Casey. Fully 3-d pet reconstruction with system matrix derived from point source measurements. *Medical Imaging, IEEE Transactions on*, 25(7):907–921, 2006.

[88] S. Pedemonte, M. Cardoso, A. Bousse, C. Panagiotou, D. Kazantsev, S. Arridge, B. Hutton, and S. Ourselin. Class conditional entropic prior for mri enhanced spect reconstruction. In *Nuclear Science Symposium Conference Record (NSS/MIC), 2010 IEEE*, pages 3292–3300. IEEE, 2010.

[89] J. C. Price, W. E. Klunk, B. J. Lopresti, X. Lu, J. A. Hoge, S. K. Ziolko, D. P. Holt, C. C. Meltzer, S. T. DeKosky, and C. A. Mathis. Kinetic modeling of amyloid binding in humans using pet imaging and pittsburgh compound-b. *Journal of Cerebral Blood Flow & Metabolism*, 25(11):1528–1547, 2005.

[90] J. Ptáček, L. Henzlová, and P. Koranda. Bone spect image reconstruction using deconvolution and wavelet transformation: Development, performance assessment and comparison in phantom and patient study with standard osem and resolution recovery algorithm. *Physica Medica*, 30(7):858–864, 2014.

[91] J. Qi, R. M. Leahy, S. R. Cherry, A. Chatziioannou, and T. H. Farquhar. High-resolution 3d bayesian image reconstruction using the micropet small-animal scanner. *Physics in medicine and biology*, 43(4):1001, 1998.

[92] M. Quarantelli, K. Berkouk, A. Prinster, B. Landeau, C. Svarer, L. Balkay, B. Alfano, A. Brunetti, J.-C. Baron, and M. Salvatore. Integrated software for the analysis of brain pet/spect studies with partial-volume-effect correction. *Journal of Nuclear Medicine*, 45(2):192–201, 2004.

[93] S. V. Ramagopalan, R. Dobson, U. C. Meier, and G. Giovannoni. Multiple sclerosis: risk factors, prodromes, and potential causal pathways. *The Lancet Neurology*, 9(7):727–739, 2010.

[94] E. Rapisarda, V. Bettinardi, K. Thielemans, and M. Gilardi. Image-based point spread function implementation in a fully 3d osem reconstruction algorithm for pet. *Physics in medicine and biology*, 55(14):4131, 2010.

[95] H. R. A. Razak, S. M. S. S. Rahmat, and W. M. M. Saad. Effects of different tube potentials and iodine concentrations on image enhancement, contrast-to-noise ratio and noise in micro-ct images: a phantom study. *Quantitative imaging in medicine and surgery*, 3(5):256, 2013.

[96] R. A. Ridsdale, D. R. Beniac, T. A. Tompkins, M. A. Moscarello, and G. Harauz. Three-dimensional structure of myelin basic protein ii. molecular modeling and considerations of predicted structures in multiple sclerosis. *Journal of Biological Chemistry*, 272(7):4269–4275, 1997.

[97] A. J. Rockmore and A. Macovski. A maximum likelihood approach to emission image reconstruction from projections. *Nuclear Science, IEEE Transactions on*, 23(4):1428–1432, 1976.

[98] O. Rousset, A. Rahmim, A. Alavi, and H. Zaidi. Partial volume correction strategies in pet. *PET clinics*, 2(2):235–249, 2007.

[99] O. G. Rousset, Y. Ma, and A. C. Evans. Correction for partial volume effects in pet: principle and validation. *The Journal of Nuclear Medicine*, 39(5):904, 1998.

[100] R. D. Rubens. Bone metastases: incidence and complications. *Cancer and the Skeleton. London: Martin Dunitz*, pages 33–42, 2000.

[101] U. E. Ruttimann, M. Unser, and D. Rio. Statistical analysis of image differences by wavelet decomposition. In *Engineering in Medicine and Biology Society, 1994. Engineering Advances: New Opportunities for Biomedical Engineers. Proceedings of the 16th Annual International Conference of the IEEE*, pages A28–A29. IEEE, 1994.

[102] S. Sastry and R. E. Carson. Multimodality bayesian algorithm for image reconstruction in positron emission tomography: a tissue composition model. *Medical Imaging, IEEE Transactions on*, 16(6):750–761, 1997.

[103] H. I. Scher, S. Halabi, I. Tannock, M. Morris, C. N. Sternberg, M. A. Carducci, M. A. Eisenberger, C. Higano, G. J. Bubley, R. Dreicer, et al. Design and end points of clinical trials for patients with progressive prostate cancer and castrate levels of testosterone: recommendations of the prostate cancer clinical trials working group. *Journal of Clinical Oncology*, 26(7):1148–1159, 2008.

[104] Y. Sheng. *Wavelet transform*, volume 747. Boca Raton, Fl: CRC, 1996.

[105] L. A. Shepp and Y. Vardi. Maximum likelihood reconstruction for emission tomography. *Medical Imaging, IEEE Transactions on*, 1(2):113–122, 1982.

[106] M. Shidahara, C. Tsoumpas, A. Hammers, N. Boussion, D. Visvikis, T. Suhara, I. Kanno, and F. E. Turkheimer. Functional and structural synergy for resolution recovery and partial volume correction in brain pet. *Neuroimage*, 44(2):340–348, 2009.

[107] M. Shidahara, C. Tsoumpas, C. McGinnity, T. Kato, H. Tamura, A. Hammers, H. Watabe, and F. E. Turkheimer. Wavelet-based resolution recovery using an anatomical prior provides quantitative recovery for human population phantom pet [11c] raclopride data. *Physics in medicine and biology*, 57(10):3107, 2012.

[108] S. Somayajula, C. Panagiotou, A. Rangarajan, Q. Li, S. R. Arridge, and R. M. Leahy. Pet image reconstruction using information theoretic anatomical priors. *Medical Imaging, IEEE Transactions on*, 30(3):537–549, 2011.

[109] M. Soret, S. L. Bacharach, and I. Buvat. Partial-volume effect in pet tumor imaging. *Journal of Nuclear Medicine*, 48(6):932–945, 2007.

[110] B. Stankoff, L. Freeman, M.-S. Aigrot, A. Chardain, F. Dollé, A. Williams, D. Galanaud, L. Armand, S. Lehericy, C. Lubetzki, et al. Imaging central nervous system myelin by positron emission tomography in multiple sclerosis using [methyl-11c]-2-(4-methylaminophenyl)-6-hydroxybenzothiazole. *Annals of neurology*, 69(4):673–680, 2011.

[111] A. Stefano, F. Gallivanone, C. Messa, M. Gilardi, and I. Gastiglioni. Metabolic impact of partial volume correction of [18f] fdg pet-ct oncological studies on the assessment of tumor response to treatment. *The quarterly journal of nuclear medicine and molecular imaging*, 58(4):413–423, 2014.

[112] S. Strother, M. Casey, and E. Hoffman. Measuring pet scanner sensitivity: relating countrates to image signal-to-noise ratios using noise equivalents counts. *Ieee transactions on nuclear science*, 37(2):783–788, 1990.

[113] S. Stute and C. Comtat. Practical considerations for image-based psf and blobs reconstruction in pet. *Physics in medicine and biology*, 58(11):3849, 2013.

[114] F. C. Sureau, A. J. Reader, C. Comtat, C. Leroy, M.-J. Ribeiro, I. Buvat, and R. Trébossen. Impact of image-space resolution modeling for studies with the high-resolution research tomograph. *Journal of Nuclear Medicine*, 49(6):1000–1008, 2008.

[115] B.-K. Teo, Y. Seo, S. L. Bacharach, J. A. Carrasquillo, S. K. Libutti, H. Shukla, B. H. Hasegawa, R. A. Hawkins, and B. L. Franc. Partial-volume correction in pet: validation of an iterative postreconstruction method with phantom and patient data. *Journal of Nuclear Medicine*, 48(5):802–810, 2007.

[116] P. Therasse, S. G. Arbuck, E. A. Eisenhauer, J. Wanders, R. S. Kaplan, L. Rubinstein, J. Verweij, M. Van Glabbeke, A. T. van Oosterom, M. C. Christian, et al. New guidelines to evaluate the response to treatment in solid tumors. *Journal of the National Cancer Institute*, 92(3):205–216, 2000.

[117] K. Thielemans, E. Asma, S. Ahn, R. Manjeshwar, T. Deller, S. Ross, C. Stearns, and A. Ganin. Impact of psf modelling on the convergence rate and edge behaviour of em images in pet. In *Nuclear Science Symposium Conference Record (NSS/MIC), 2010 IEEE*, pages 3267–3272. IEEE, 2010.

[118] K. Thielemans, C. Tsoumpas, S. Mustafovic, T. Beisel, P. Aguiar, N. Dikaios, and M. W. Jacobson. Stir: software for tomographic image reconstruction release 2. *Physics in medicine and biology*, 57(4):867, 2012.

[119] B. A. Thomas, K. Erlandsson, M. Modat, L. Thurfjell, R. Vandenberghe, S. Ourselin, and B. F. Hutton. The importance of appropriate partial volume correction for pet quantification in alzheimers disease. *European journal of nuclear medicine and molecular imaging*, 38(6):1104–1119, 2011.

[120] J. Tohka and A. Reilhac. Deconvolution-based partial volume correction in raclopride-pet and monte carlo comparison to mr-based method. *Neuroimage*, 39(4):1570–1584, 2008.

[121] S. Tong, A. M. Alessio, K. Thielemans, C. Stearns, S. Ross, and P. E. Kinahan. Properties and mitigation of edge artifacts in psf-based pet reconstruction. *Nuclear Science, IEEE Transactions on*, 58(5):2264–2275, 2011.

[122] F. E. Turkheimer, J. A. Aston, R. B. Banati, C. Riddell, and V. J. Cunningham. A linear wavelet filter for parametric imaging with dynamic pet. *Medical Imaging, IEEE Transactions on*, 22(3):289–301, 2003.

[123] F. E. Turkheimer, N. Boussion, A. N. Anderson, N. Pavese, P. Piccini, and D. Visvikis. Pet image denoising using a synergistic multiresolution analysis of structural (mri/ct) and functional datasets. *Journal of Nuclear Medicine*, 49(4):657–666, 2008.

[124] F. E. Turkheimer, M. Brett, D. Visvikis, and V. J. Cunningham. Multiresolution analysis of emission tomography images in the wavelet domain. *Journal of Cerebral Blood Flow & Metabolism*, 19(11):1189–1208, 1999.

[125] M. Unser and A. Aldroubi. A review of wavelets in biomedical applications. *Proceedings of the IEEE*, 84(4):626–638, 1996.

[126] M. Unser, P. Thevenaz, C. Lee, and U. E. Ruttimann. Registration and statistical analysis of pet images using the wavelet transform. *IEEE Engineering in Medicine and Biology Magazine*, 14(5):603–611, 1995.

[127] K. Van Laere, M. Koole, I. Lemahieu, and R. Dierckx. Image filtering in single-photon emission computed tomography: principles and applications. *Computerized Medical Imaging and Graphics*, 25(2):127–133, 2001.

[128] J. Van Waesberghe, W. Kamphorst, C. J. De Groot, M. A. Van Walderveen, J. A. Castelijns, R. Ravid, G. Lycklama a Nijeholt, P. Van Der Valk, C. H. Polman, A. J. Thompson, et al. Axonal loss in multiple sclerosis lesions: magnetic resonance imaging insights into substrates of disability. *Annals of neurology*, 46(5):747–754, 1999.

[129] M. Veronese, B. Bodini, D. García-Lorenzo, M. Battaglini, S. Bongarzone, C. Comtat, M. Bottlaender, B. Stankoff, and F. E. Turkheimer. Quantification of [11c] pib pet for imaging myelin in the human brain: a test–retest reproducibility study in high-resolution research tomography. *Journal of Cerebral Blood Flow & Metabolism*, 2015.

[130] T. O. Videen, J. S. Perlmutter, M. A. Mintun, and M. E. Raichle. Regional correction of positron emission tomography data for the effects of cerebral atrophy. *Journal of Cerebral Blood Flow & Metabolism*, 8(5):662–670, 1988.

[131] K. Vunckx, A. Atre, K. Baete, A. Reilhac, C. M. Deroose, K. Van Laere, and J. Nuyts. Evaluation of three mri-based anatomical priors for quantitative pet brain imaging. *Medical Imaging, IEEE Transactions on*, 31(3):599–612, 2012.

[132] K. Wienhard, M. Schmand, M. Casey, K. Baker, J. Bao, L. Eriksson, W. Jones, C. Knoess, M. Lenox, M. Lercher, et al. The ecat hrrt: performance and first clinical application of the new high resolution research tomograph. *Nuclear Science, IEEE Transactions on*, 49(1):104–110, 2002.

[133] D. H. Woodbury and W. H. Beierwaltes. Fluorine-18 uptake and localization in soft tissue deposits of osteogenic sarcoma in rat and man. *Journal of Nuclear Medicine*, 8(9):646, 1967.

[134] C. Wu, V. W. Pike, and Y. Wang. Amyloid imaging: from benchtop to bedside. *Current topics in developmental biology*, 70:171–213, 2005.

[135] J. Yang, S. Huang, M. Mega, K. Lin, A. Toga, G. Small, and M. Phelps. Investigation of partial volume correction methods for brain fdg pet studies. *IEEE Transactions on Nuclear Science*, 43(6):3322–3327, 1996.

[136] H. Young, R. Baum, U. Cremerius, K. Herholz, O. Hoekstra, A. Lammertsma, J. Pruim, P. Price, et al. Measurement of clinical and subclinical tumour response using [18 f]-fluorodeoxyglucose and positron emission tomography: review and

1999 eortc recommendations. *European journal of cancer*, 35(13):1773–1782, 1999.